The Pennsylvania State University

The Graduate School

SPATIOTEMPORAL AND COMBINATORIAL DELIVERY OF MIRNAS FOR MODULATION OF OSTEOGENESIS IN HUMAN ADIPOSE STEM CELLS

A Dissertation in

Bioengineering

by

Mohammad Abu-Laban

Submitted in Partial Fulfillment
of the Requirements
for the Degree of

Doctor of Philosophy

August 2019

The dissertation of Mohammad Abu-Laban was reviewed and approved* by the following:

Daniel J. Hayes
Associate Professor of Bioengineering
Dissertation Adviser
Chair of Committee

Jian Yang
Professor of Bioengineering

Scott Medina
Assistant Professor of Bioengineering

Sulin Zhang
Professor of Engineering Science and Mechanics

William Hancock
Professor, Chair of The Intercollege Graduate Program in Bioengineering

*Signatures are on file in the Graduate School.

ABSTRACT

Short non-coding nucleic acid molecules play an important role in regulating gene expression in numerous processes from embryonic to immune system development, and have been sought after as potential therapeutic agents relevant to human physiology and pathology. However, clinical translation has been limited due to risks involving unspecified off-target effects and inefficient delivery. With the capability to respond to internal or external stimuli, nanoparticle delivery systems hold great promise for efficient spatiotemporal gene control for therapeutic applications. Additionally, techniques that allow for delivery of heteroplexed nucleic acid sequences with precise sequential and spatial targeting could result in improved control of processes such as wound repair. For attachment of the therapeutic, computation modeling suggested the possibility of three alternate chemistries to tether amine-terminal biomolecules onto nanoparticles using thermally-labile linkers. Using the versatile tool of the retro-Diels-Alder (DA/rDA) chemistry, we synthesized three cycloadducts that thermally cleaved at different temperature ranges. Furthermore, we utilized the unique properties of noble metal nanoparticles and their distinct plasmonic abilities to induce surface release. With these tools, we demonstrated the sequential delivery of two miRNA structures for an enhanced osteogenic effect of human adipose stem cells (hASCs). Furthermore, using a 3D collagen culture as a model, we have shown the ability to deliver miR-148b for bone differentiation of hASCs within the outer-band region of the hydrogel, and miR-21 in the centered cells for increased adipogenic differentiation. Utilizing the capability of the retro-Diels-Alder chemistry and the differential optical photothermal responses of gold and silver nanoparticles, spatially discrete differentiation into two different tissue types was achieved. In summary, the presented document demonstrated three alternate DA linkers with varying thermal responses and rDA kinetics, sequential miR-148b and miR-21 release via co-delivery on photo-responsive gold and silver nanoparticles, and spatially targeted mineralization and adipogenic regeneration across different sections of our collagen model.

TABLE OF CONTENTS

List of Tables v
List of Figures vi
Acknowledgements xii

Chapter 1. Literature Review 1
References 13

Chapter 2. Comparison of Thermally Actuated *Retro*-Diels-Alder Release Groups for Nanoparticle Based Nucleic Acid Delivery 19
Introduction 21
Materials & Methods 23
Results & Discussion 28
Conclusion 41
References 42

Chapter 3. Combinatorial Delivery of miRNA Mimics Using Plasmonic Nanoparticles for Amplified Osteogenic Differentiation of Human Adipose Stem Cells 48
Introduction 51
Results & Discussion 52
Materials & Methods 72
Conclusion 80
References 82

Chapter 4. Spatial Modulation of Osteoblast Differentiation in 3D-cultured Human Adipose Stem Cells 87
Introduction 87
Materials & Methods 89
Results & Discussion 94
Conclusion 100
References 100

Chapter 5. Summary & Conclusion 103

Appendix A. Supplementary Information for Chapter 2 105

Appendix B. Supplementary Information for Chapter 3 108

LIST OF TABLES

Chapter 2, Table 1. Optimized structures used for B3LYP/ 6-311G* computation. Yellow=S, Red=O, Black=C, Blue=N, White=H. Images rendered using PyMOL……....29

Chapter 2, Table 2. Gibbs free energy & enthalpy reaction barriers generated from B3LYP/6-311G* theory…….29

Chapter 2, Table 3. List of fit parameters obtained by fitting SHG data using first order exponential equation, +/-SEM……...38

Chapter 3, Table 1. hASC groups treated with GNP-miR-148b and/or SNP-miR-21, illuminated at different wavelengths…….77

Appendix A, Table S1. Input example used for furan computation at 298.15 K using B3LYP, 6-311G*……...105

Appendix B, Table S1. Fit parameters obtained for the SNP-miR-21nanoparticle system at different 400 nm laser powers……..110

Appendix B, Table S2. Fit parameters obtained for the GNP-miR-148b nanoparticle system at different 530 nm laser powers……..111

Appendix B, Table S3. ARS images for all NP groups tested……..114

LIST OF FIGURES

Chapter 1, Figure 1. Schematic illustrating oscillations between conduction electrons and lattice along resonant light waveform……....5

Chapter 1, Figure 2. Schematic illustrating attachment and external stimulation of payload release……..7

Chapter 1, Figure 3. Proposed retro-Diels-Alder reaction scheme……...8

Chapter1, Figure 4. Schematic illustrating Runx2 expression via wnt signaling pathway (left), and induction of Smad pathway to promote osteogenic gene expression (right)……..12

Chapter 2, Figure 1. Overall schematic illustrating pericyclic reaction between dienes with 6-maleimidohexanoic acid and conjugation onto nanoparticle via generic thiol linkage (1). EDC coupling chemistry was utilized to link amine-terminated siRNA to nanostructure (2)……...23

Chapter 2, Figure 2. Normalized fluorescence of FAM-siRNA release from covalently-linked SNPs via retro-Diels-Alder reaction at different water bath temperatures, +/-SEM…….32

Chapter 2, Figure 3. a) SHG spectra for SNP+pyrrole+maleimide+siRNA sample at 0, 30, and 300 s, b) normalized SHG spectra for control sample, SNP+cysteamine+maleimide, c) and real time decay of SHG maxima at 400 nm for SNP+pyrrole+maleimide+siRNA and SNP+cysteamine+maleimide linker, +/-SEM……....36

Chapter 2, Figure 4. Time-dependent SHG profile of thermal release of siRNA from (a) SNP+pyrrole+maleimide+siRNA, (b) SNP+ furan+maleimide+siRNA and (c) SNP+thiophene+maleimide+siRNA complexes, +/-SEM…….37

Chapter 2, Figure 5. Photothermal release of SNPs conjugated with the 3 different DA linkers, after 405 nm resonant irradiation, measured with fluorescence intensity, +/-SEM……...40

Chapter 3, Graphical Abstract...……....50

Chapter 3, Figure 1. A. TEM image and UV-Vis spectra for silver nanoparticles, and B. gold nanoparticles. C. Zeta potential measurements of miRNA-NP conjugates for silver and gold surfaces with increasing doses of incident light. D. Normalized fluorescence measurements of nanoparticle supernatant solutions, irradiated at 405 and 530 nm light wavelengths. Gold nanoparticle surfaces in this experiment were modified with Diels-Alder linked miRNA mimic-FAM dye molecules, while silver nanoparticles were surface-modified similarly with Cy3-tagged dye molecules.....54

Chapter 3, Figure 2. A. Representative SHG spectra of miRNA-functionalized silver nanoparticles at different wavelengths and irradiation times. SHG intensity of the miRNA-functionalized gold and silver nanoparticles as a function of time under varying laser irradiation powers using 530 nm (B) and 400 nm (C). D. The obtained photothermal cleaving rate constants as a function of laser power for miRNA-functionalized gold and silver nanoparticles, using 530 nm and 400 nm irradiation, respectively.....58

Chapter 3, Figure 3. Colocalization of SNPs (blue) & conjugated FAM molecules (green) in hASCs. Irradiation at 400 nm (50 J) and 530 nm (565 nm). 60X magnification used with scale bars annotated at 33 μm.....61

Chapter 3, Figure 4. Colocalization of GNPs (red) & conjugated FAM molecules (green) in hASCs. Irradiation at 400 nm (50 J) and 530 nm (565 nm). 60X magnification used with scale bars annotated at 33 μm.....62

Chapter 3, Figure 5. Xylenol Orange stained samples, imaged 24h after applied staining solution (Top). All images were collected at constant exposure conditions and magnification as indicated by the scale bar set at 200 μm. (Bottom) Quantification of mineralization using Alizarin Red S staining solution and P-value summary between 3 negative controls and

experimental groups. Values less than 0.05 are denoted as (*), and (**) for those less than 0.1, and X for no statistical significance. The labels indicate the different samples as follows: A = Stromal media control; B = miR-21-SNPs & miR-148b-GNPs without activation; C = Osteogenic differentiation media control; D = miR-21-SNPs & miR-148b-GNPs, light activated at 405 nm and 530 nm wavelengths of light, simultaneously, 16 h after transfection; E = miR-21-SNPs & miR-148b-GNPs, light activated at 405 nm 16 h post-transfection, followed by 530 nm at 40 h; F = miR-21-SNPs & miR-148b-GNPs, light activated at 530 nm 16 h post-transfection, followed by 405 nm at 40 h; G = miR-21-SNPs & miR-148b-GNPs, light activated at 405 nm 16 h post-transfection, followed by 530 nm at 64 h; H = miR-21-SNPs & miR-148b-GNPs, light activated at 530 nm 16 h post-transfection, followed by 405 nm at 64 h.....64

Chapter 3, Figure 6. Day 7 & 21 PCR Results. ALP expression was measured at day 7, while Runx2, OPN and BMP-2 were measured at day 21. The legends indicate the different samples as follows: B = miR-21-SNPs & miR-148b-GNPs without activation; C = Osteogenic differentiation media control; D = miR148-GNPs light activated at 530 nm 16 h post-transfection; E = miR-21-SNPs & miR-148b-GNPs, light activated at 405 nm and 530 nm wavelengths of light, simultaneously, 16 h after transfection; F = miR-21-SNPs & miR-148b-GNPs, light activated at 405 nm 16 h post-transfection, followed by 530 nm at 40 h; G = miR-21-SNPs & miR-148b-GNPs, light activated at 530 nm 16 h post-transfection, followed by 405 nm at 40 h; H = miR-21-SNPs & miR-148b-GNPs, light activated at 405 nm 16 h post-transfection, followed by 530 nm at 64h; I = miR-21-SNPs & miR-148b-GNPs, light activated at 530 nm 16 h post-transfection, followed by 405 nm at 64 h.....66

Chapter 3, Figure 7. Cell count number, measured by DAPI staining of cells, and Sox2 gene expression at day 21. The legends indicate the different samples as follows: B = miR-21-SNPs &

miR-148b-GNPs without activation; C = Osteogenic differentiation media control; D = miR148-GNPs light activated at 530 nm 16 h post-transfection; E = miR-21-SNPs & miR-148b-GNPs, light activated at 405 nm and 530 nm wavelengths of light, simultaneously, 16 h after transfection; F = miR-21-SNPs & miR-148b-GNPs, light activated at 405 nm 16 h post-transfection, followed by 530 nm at 40 h; G = miR-21-SNPs & miR-148b-GNPs, light activated at 530 nm 16 h post-transfection, followed by 405 nm at 40 h; H = miR-21-SNPs & miR-148b-GNPs, light activated at 405 nm 16 h post-transfection, followed by 530 nm at 64 h; I = miR-21-SNPs & miR-148b-GNPs, light activated at 530 nm 16 h post-transfection, followed by 405 nm at 64 h.....68

Chapter 3, Figure 8. RAMAN Spectroscopy results for Groups A (SM), C (OM) and I (SNP-miR-21 & GNP-148b) with hydroxyapatite powder as a reference.....71

Chapter 4, Figure 1. Schematic illustrating experimental setup of spatially-controlled illumination experiments, with one region of hASCs/collagen scaffold exposed to 405nm, and another at 530nm.....91

Chapter 4, Figure 2. Immunostaining results for Runx2 (above) and OCN expression (below) in hASCs, treated with miR-21 and miR-148b after nanoparticle photoactivation.....95

Chapter 4, Figure 3. OsteoImage^{TM} staining. **A**. Center region: 405nm-illuminated, miR-21 released. **B**. Outer-band: 530nm-illuminated, miR-148b released.....96

Chapter 4, Figure 4. A-F. Panels showing serial imaging of ARS mineralization of hASCs in collagen sample, moving outward from the center region. Quantification of ARS (below) by measuring absorbance and normalizing to the number of cells between regions.....98

Chapter 4, Figure 5. Oil Red O Staining. (Above) A. hASCs-only group, B. Center-region activated with 405nm to release miR-21, and C. Outer-band, osteogenically induced with miR-

148b photorelease. (Below) Normalized absorbance quantification of Oil Red O staining, after de-staining.....99

Appendix A, Figure S1. UV-Vis spectra of SNP, with maxima at 415 nm.....105

Appendix A, Figure S2. Bulk temperature of SNP solution during irradiation with 405 nm mounted LED, +/-SEM.....107

Appendix B, Figure S1. Absorbance spectra of Diels-Alder linker.....108

Appendix B, Figure S2. Representative SHG spectra of miRNA-functionalized gold nanoparticles at different wavelengths and irradiation times.....109

Appendix B, Figure S3. Extinction spectra of the GNPS, the miRNA-functionalized GNPs, and the miRNA-functionalized GNPs after laser irradiation with 530 nm wavelength.....109

Appendix B, Figure S4. Extinction spectra of the SNPs, the miRNA-functionalized SNPs, and the miRNA-functionalized SNPs after laser irradiation with 400 nm wavelength.....110

Appendix B, Figure S5. Colocalization, z-stack images of SNP/GNP with FAM-miRNA molecules.....112

Appendix B, Figure S6. Xylene Orange images for all NP groups tested.....114

Appendix B, Figure S7. ARS quantification for all NP groups normalized to cell count.....116

Appendix B, Figure S8. Chemical transfection groups ARS (images presented in same order, left to right, as listed on x-axis of graph) 117

Appendix B, Figure S9. Chemical transfection groups PCR day 21.....118

Appendix B, Figure S10. All NP groups PCR day 7.....119

Appendix B, Figure S11. All NP groups PCR day 21.....119

Appendix B, Figure S12. DAPI/Cell count at Day 21 for chemical transfection (top) and NP groups (bottom).....120

Appendix B, Figure S13. Transfection efficiencies of SNPs and GNPs in hASCs, measured using Flow Cytometry of Cy3 conjugated miRNA mimics, and uptake efficiency of SNPs using ICP-AES.....121

ACKNOWLEDGEMENTS

I would like to thank my academic advisor and mentor, Dr. Daniel Hayes, for giving me the opportunity to join his lab. In every phase of this project, his wise guidance and direction helped make this work stronger, and myself a better researcher. The experiences learned under his mentorship will continue to help shape my future endeavors and career.

I am also grateful to my committee members, Dr. Scott Medina, Dr. Sulin Zhang, and Dr. Jian Yang, whose constructive critiques and recommendations helped develop and enhance this project to a higher standard. I would also like to express gratitude to our close collaborators, Dr. Louis Haber and Dr. Raju Kumal from Louisiana State University, for their extensive knowledge of SHG and strengthening our contributions in nanomedicine design.

To my fellow colleagues and lab mates, both former and current, namely, Cong Chen, Anoosha Forghani, Jonathan Casey, Lisa Bernsten, Yiming Liu, and Mukunth Parthasarathy, I value the friendships and collaborations forged, which made working in the lab a pleasant experience with never a dull moment.

And last but not least, I am most thankful to my family; to my mother, who helped mold and encourage my ambitions every step of the way no matter the sacrifice, and to my two brothers and sister for their endless moral support and love.

CHAPTER 1.
Literature Review

Nucleic acid caging can delay the onset of degradative pathways in the cell from lysosomes and RNAse while providing spatiotemporal release of a therapeutic, allowing for tissue specific control of delivery. Noble metallic nanoparticles (Pt, Au, Ag etc.) have shown high transfection efficiencies but also unique optical properties that allow these particles to respond to electromagnetic fields within the visible and near infrared spectrum. These optical responses are unique to the metal composition of the particle, which upon excitation with photons at resonant frequencies, results in the generation of excited plasmonic states in the particles, giving rise to a cascade of energy transfer and scattering, resulting in photonic and phononic responses, often referred to as the particles' photothermal effect. The ability to temporally deliver gene therapies and small molecules has already been demonstrated. However, the delivery of different drugs, peptides and nucleic acid therapeutics at distinct gradients of space and time has yet to be reported, despite the clear need for enhanced spatiotemporal control of therapeutic delivery in clinical treatments. In addition, other design issues pertaining to the delivery vehicle need to be addressed including their cyto- and biocompatibility, as well as the linking chemistry between substrate and biomolecule. By altering the enthalpies and entropies of activation barriers of the linkers, either by reducing or increasing, we can provide a larger window for molecular discharge. To demonstrate the ability to sequentially and spatially administer more than one antisense nucleic acid, we turned to the known osteoinductive sequence of miR-148b, and miR-21, a known regulator of pluripotency, to enhance the osteogenesis of human adipose stem cells and provide discrete spatial differentiation of hASCs in 3D collagen cultures.

Nanocarriers in gene therapy

Controlled drug delivery systems have gained traction due to their ability to be localized *en masse* at sites of interest, requiring a lower dosage, and circumventing off-target effects with vital organs. Nanoparticles, broadly defined as particles less than 100nm, have shown great potential in drug delivery applications. Their large reactive area provides an effective substrate for conjugation and their properties can be tuned to enhance ease of passage across membrane barriers, as well as evading degradation by the mononuclear phagocyte system (MPS). Tested nanocarrier systems include polymer, dendrimer, pepti/liposome, carbon, silica, and inorganic materials [1, 2, 3, 4, 5, 6, 7].

Drug delivery systems (DDS) can be classified as organic, such as liposomes, peptides and polymers, or inorganic, such as iron oxide, platinum, gold etc. Polymeric DDS have made advances in clinical trials, while liposomal-based technologies already exist in the market with FDA approval [8, 9]. The latter, however, has been met with translational obstacles. These amphiphilic structures, consisting of a lipid bilayer encapsulating an aqueous core, offer an attractive delivery system due to their flexible physicochemical and biophysical properties [10].

Liposomal structures have been fashioned with various modifications, including targeting monoclonal antibodies [11] and PEG-ylated functional groups for increased circulation longevity [12]. Liposomal cell interaction and drug delivery can occur via different pathways. One mechanism is the adsorption of the lipid bilayer to the membrane of the cell and its enzymatic degradation, followed by passive diffusion of the encapsulated contents into the cell [13]. This mechanism is arguably the least efficient and desirable as it would require large doses of the drug to achieve a threshold concentration to overcome losses from diffusion away from the cell. A second mechanism involves fusion of the liposome with the membrane and the direct release of

the contents into the cytoplasm [14], and a third mechanism involving receptor mediated endocytosis [15]. The former method exposes the therapeutic contents to DNAase/RNAse and other enzymatic degradation by the cell, prior to achieving their biological purpose, while the latter requires additional modification of the liposomal surfaces to withstand the acidic environment of lysosomes and endosomes [16]. The amphiphilic nature of liposomal design ensures sealed encapsulation of loaded molecules. However, in blood circulation, exposure to plasma and specific plasma proteins, particularly lipoproteins, increases the permeability of solutes into the liposome structure [17]. As a result, modifications to liposomal structures continue to be investigated that may prolong their stability *in vivo* [18].

There are also an array of published works involving polymeric NPs, including biocompatible and biodegradable poly (D, L-lactic-co-glycolic acid)-poly (ethylene glycol) (PLGA-b-PEG) polymers [19] [20]. In [21], specific targeting of prostate cancer cells was accomplished *in vitro* and *in vivo* by surface functionalization of the polymeric NPs with A10 2'-fluoropyrimidine ribonucleic acid aptamers that identify prostate-specific membrane antigens.

A major challenge faced by most developed DDS is the ability to deliver the requisite dosage for therapeutic effect *in vivo*. This can be complicated during sequestration by the mononuclear phagocyte and reticuloendothelial systems (MPS/RES) and frequent interactions with plasma proteins that may disrupt the integrity of the nanoparticle and lead to less than optimal delivery of the payload [22]. With all nanoparticle systems, the retention of the delivery system within circulation is crucial, with modifications to prolong its duration constantly being explored [23]. Attenuating the surface with alternative functional groups to regulate surface charge, and hence opsonization, or by including a more hydrophobic loading, or altering particle size are some parameters used to extend a therapeutics' lifetime *in vivo*.

With the advent of nanotechnology, metal nanoparticles have been extensively researched with potential roles in vaccinations and drug delivery [24]. Their high surface area to volume ratios, well defined toxicity and biocompatibility, as well as diverse selection of well described chemical conjugation make them good candidates for drug delivery [25]. These particles have been used in cancer therapies, platinum in chemotherapy [26], and gold in photothermal therapy for hyperthermic ablation of tumor tissue [27]. They can also act as diagnostic contrast agents as well as drug vehicles, with iron oxide nanoparticles already utilized in MRI scans [28].

Gold nanoparticles have been heavily investigated as a therapeutic vehicle for nucleic acid delivery [29], [30]. Their general non-toxicity, stability and high transfection efficiency make them an ideal candidate for cellular targeting [31]. Their optical properties, attributed to their oscillating band of conduction electrons referred to as the surface plasmon resonance, have attracted groups to utilize the nanoparticles as biomolecular contrast imaging agents [32]. Additionally, their photothermal effect, i.e. their ability to transfer light energy absorbed into heat, has garnered interest to use the nanoparticles as a heat source for photothermal treatment (PTT) in cancer therapies [33]. Similar to Au nanoparticles, Ag nanoparticles possess antimicrobial properties, and have also been demonstrated to be effective delivery therapeutics [34]. The plasmonic properties of nanoparticles such as gold and silver, provide a convenient method to catalyze surface reactions which can provide an effective trigger to induce cargo decaging upon excitation. While similar in phenomena, the two materials are distinct in their EM excitation ranges. While Au nanoparticles can be tuned to absorb light at 530-570nm, Ag can absorb in 405-450nm ranges [35, 36]. The distinct plasmonic resonance wavelengths can provide two discrete triggers to induce drug release. In a parallel dosage, one therapeutic can be

discharged at one wavelength followed by the second at an alternate light wavelength, and each possibly irradiated at overlapping tissue sections. Sequential & spatial gene delivery can be achieved with illumination of tissue samples at distinct timepoints and discrete sections, accomplished with advanced spatiotemporal control.

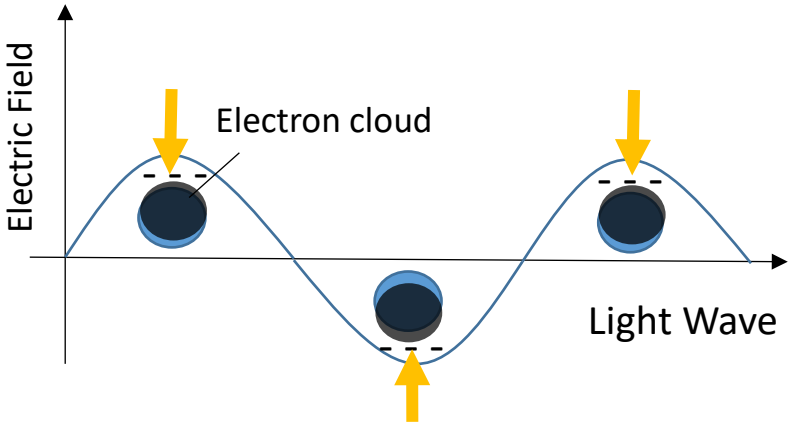

Figure 1. Schematic illustrating oscillations between conduction electrons and lattice along resonant light waveform

Plasmonic activity of metal nanoparticles arises from the oscillation between a charged electron cloud, and its positive ion lattice (**Figure 1**). At wavelengths of light resonant with the oscillation frequency, strong light scattering occurs with enhancement of local electromagnetic fields [37]. At maximum polarizability, the particle exhibits its surface plasmon resonance peak. The electric field enhancement is strongly dictated by the pairing of the incident wavelength and the resonance wavelength. When compared to gold, silver nanospheres exhibited higher extinction efficiencies than gold, upon resonant light illumination [38]. The electric field energy enhancement for silver nanospheres at short-excitation wavelength lasers (400nm), was much higher than that for gold at longer-excitation wavelength lasers (530nm). The photothermal property of the nanoparticles are largely dependent on the absorption cross sections, which decreases as size increases and scattering becomes more relevant [39]. Between gold and silver, gold has been argued to exhibit higher photothermal responses as a result of its high absorption cross section spectra, and thermal stability [40]. However, discrepancies between different

nanoparticle syntheses methods resulting in varying sizes with an array of stabilizing agents to use that control aggregation make it difficult to decisively conclude whether gold or silver nanoparticles are more efficient than the other at surface catalytic reactions, as it is also often difficult to attribute surface chemistry reactions to purely thermal, photonic, or hot electron phenomenon. Criteria for LSPR include particle sizes smaller than the wavelength of applied light, and materials possessing negative real and small positive imaginary dielectric constants [41].

Upon photoexcitation, "hot" electrons inside the metal surface will either remain trapped, causing local heating of the metal and its surroundings, or in cases where electron excitation outpaces the rapid carrier relaxation processes and electron energy is greater than the metal work function, electrons can escape from the metal surface [42]. Energy loss can also result in the re-emission of photons as high energy electrons return to vacant lower energy bands, referred to as the Auger effect [43]. When trapped inside the metal, photoexcited electron-electron scattering can thermalize and lead to electron-phonon and phonon-phonon collisions, dissipating energy into the surrounding media. The phenomenon is often referred to as the photothermal effect [44], [45], [46].

Surface conjugation and de-caging of therapeutics

Molecules can be attached to surfaces via different means including adsorption, covalent linkage or electrostatically. Covalent bonding provides precise control over surface load, and provides increased stability to prevent premature release, improving spatial and temporal control of delivery. The mechanism of drug release is often neglected in many studies, with some elucidating only the final result of discharge. However, it is important to understand the method and chemistry of attachment to predict its behavior *in vivo*, and behavior response at on-target as

well as off-target sites. Designing a vehicle system with a specific exogenous stimulus to trigger de-caging is a desired aspect in many potential therapeutics.

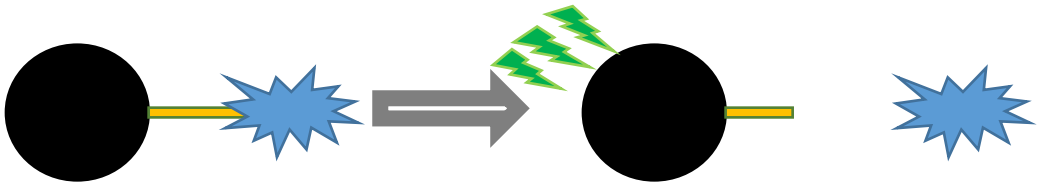

Figure 2. Schematic illustrating attachment and external stimulation of payload release

Most studied nanodelivery vehicles for therapeutics utilize hydrophobicity/ hydrophilicity characteristics of drug molecules and incorporate them into their vehicles accordingly, using either monolayers or bilayers for drug entrapment [47, 48]. Electrostatic forces between oppositely charged surfaces and ligands are also used in conjugation chemistries, with environmental cues like cell pH that cause the delivery vehicle's disintegration followed by the discharge of its contents [49]. Added targeted capabilities using antibodies has the advantage of efficiently directing delivery systems to enact at specific tissue locations or cells. Although this strategy improves intracellular drug levels in target areas, the endocytosed material is subjected to the acidic lysosomal compartment and hydrolysis by various enzymes, such as RNAse and DNAse resulting in reduced biological activity [50]. This is a critical issue as most delivery methods release their payload instantly upon cellular entry which may not be desired. This problem is particularly challenging for therapies that are sensitive to such degradation, including nucleic acid and peptidic drugs [51]. In such cases, methods enabling the release of the entrapped payload into the cytosol are advantageous. Ideally, the vehicle system would remain intact even intracellularly for a period of time, if brief, prior to desired de-caging. The strategy has the benefit of shielding biological molecules from degradation from enzymes and lysosomes prior to reaching their target, largely by the sterically hindering effect of the uncompromised vehicle

system. This increased stability improves the chances of small molecules achieving protein or gene regulation upon stimulated release in the cytosol.

For efficient temporal manipulation of small molecules, click chemistry, most commonly reported between an azide and alkyne [52], can provide bioconjugation abilities of biomolecules. These reactions are wide in scope, but pertain to reactions proceeding under mild conditions to give high yields and innocuous by-products [53], [54]. Diels Alder reactions are a class of reactions that meet the criteria, and involve formation of a cycloadduct product derived from a dienophile and diene in which more stable σ-bonds are formed from [4+2] π-bonds, based on overlapping electron levels between higher and lower occupied and unoccupied molecular orbitals [55]. At higher temperatures the cyloaddition reactions undergo reverse reaction pathways, referred to as the retro-Diels-Alder (rDA) reaction, to reproduce their diene and dienophile counterparts [56].

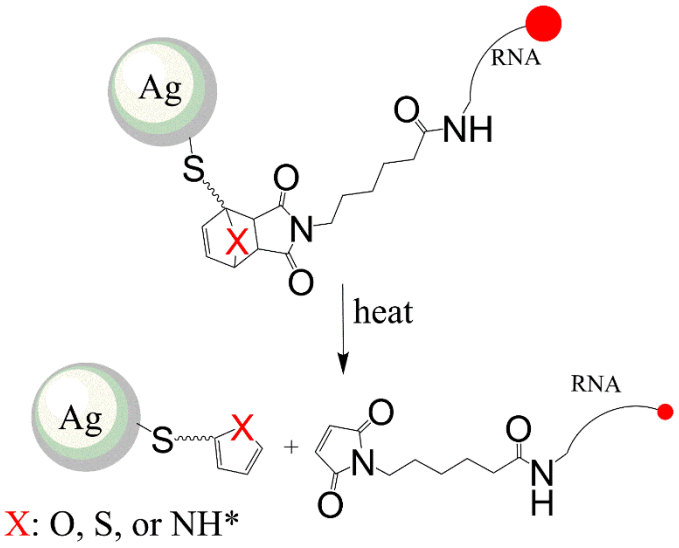

Figure 3. Proposed retro-Diels-Alder reaction scheme

In Bakhtiari et al. [57], it was demonstrated that the cycloadduct between a furan and maleimide could be synthesized at room temperature over 7 days, with the rDA reaction observed to occur at temperatures 60°C and above. Using gold nanoparticles modified with

fluorescein-tagged furan-maleimide linkers and irradiated at their plasmonic wavelength of 532nm, an increase in solution fluorescence was observed due to localized plasmon-phonon heat generation triggering the rDA reaction and releasing the markers. The rDA chemistry is a versatile tool for the delivery of short biological molecules utilizing simple chemical modifications, and providing a stimuli-responsive switch to trigger cargo release based on local heat induction and avoiding tissue damage.

The Diels-Alder forward reaction can be facilitated via an electron-enriched diene with an electron-poor dienophile, where each molecule is typically substituted with electron-donating and electron-withdrawing groups, respectively [58]. In the current study, we aim to build on the chemistry investigated previously [57], in which the bond breaking of 7-oxa-bicyclo-[2.2.1]hept-5-ene-2,3-dicarboxylic imide was studied, and explore the bicyclic reactions of alternate dienes and attain distinct temperature ranges and retro reaction conditions in which to initiate the rDA reaction, for the purpose of multiplex delivery applications.

Bone Regeneration & miRNA

In regenerative tissue engineering, discontinuities in chemical and physical properties at a graded interface can hamper functional efficiency of a dynamic tissue interface. For example, the interface between the innervated and vascularized periodontal ligament and the mineralized hard tissue (bone) can be affected by periodontal disease or non-physiological loads known to decrease the biomechanical and functional efficiency of the bone-tooth fibrous joint [59]. Bone repair is a complex process of regeneration that involves the activity of osteoblasts and osteocytes, as well as chondrocytes, to produce growth factors including BMPs, TGF, PDGF, etc. [60]. Mesenchymal stem cells are a key cell population involved in osteogenesis. The ability to heal bone defects depends on biological as well as mechanical factors, but more importantly

bone fractures require optimal blood circulation for optimal healing process. Nonunion or delayed union of bone fractures occurs regularly in elderly patient populations, individuals with sickle cell disease, cancer patients treated with anti-angiogenic therapies. Most treatments often require surgical implantations to prompt healing. The current inexpensive method of treatment is the use of allografts and xenografts to promote tissue regeneration using mammalian scaffolds [61]. However, the gold standard is the use of autografts, harvesting healthy and similar mature cell types/tissue from the same patient to defect sites [62]. Such procedures are often associated with morbidity for the patient stemming from immunogenic responses at the defect and extracted sites [63].

MicroRNAs (miRNAs) are central post-transcriptional regulators of gene expression. Many studies have demonstrated the significance of miRNAs in the control of osteoblast and osteoclast differentiation and the functions of these short single stranded RNAs [64, 65, 66]. Prospectively, miRNAs may play a critical role in the development of new therapeutics aimed at facilitating fracture repair. Delivery systems providing spatiotemporal control have the potential to improve outcomes in surgical reconstruction and regenerative medicine by precise modulation of tissue repair processes. Modulation of gene expression with miRNA mimics is a promising technique for improving control of tissue repair processes particularly when combined with inherent mesenchymal stromal/stem cells (MSC) progenitors. We will use this capability to explore the co-regulation of miR-21 mimic, a known regulator of cell proliferation and pluripotency [67], and miR-148b mimic, a potent *de novo* regulator of MSC osteogenesis [34].

MicroRNA-148b was investigated in [68] [69]and shown to upregulate alkaline phosphatase to stimulate osteogenic activity *de novo* in hBMSCs and hASCs. Kuei-Chang Li et al. [70] investigated miR-148b in hASCs and reported NOG as a target gene. NOG is known to

negatively regulate bone morphogenetic protein expressions, which play a role in bone formation but also signaling via the SMAD pathway to activate osteogenic promoter genes in MSC nuclei. These studies indicate that miR-148b participates in the downregulation of NOG and promotes osteogenic differentiation via BMP upregulation.

MicroRNA-21 is another widely studied RNA sequence, particularly its regulation of cell proliferation of cancer and stem cells [71] [72]. In [73], miR-21 was demonstrated to be overexpressed in non-small cell lung cancer cells, and played a role in repressing PTEN, a tumor suppressor, leading to lung cancer cell growth and invasion. In contrast, overexpression in mouse embryonic stem cells was found to down-regulate the "stem-ness" and pluripotency of cells by directly targeting Sox2 [74]. Studies with MSCs suggest miR-21 plays a role in arresting stem cells' G1-S-G2-M cell cycle. Reports of miR-21 mimics promoting osteogenic differentiation in hBMSCs by targeting the SMAD-7 gene a suppressant of the TGF-β family [75], and adipogenesis in hASCs via TGF-β signaling modulation [76], have been demonstrated. These results allude to the strong possibility of miR-21 acting as an enabler towards differentiation in the most probable and likely lineage associated with the cell type; in this case adipocytes/fibroblasts for hASCs and osteoblasts for hBMSCs. It is, therefore, likely to drive cells down an alternate pathway with one post-transcriptional regulator, miR-148b, and amplify their differentiation effect with miR-21.

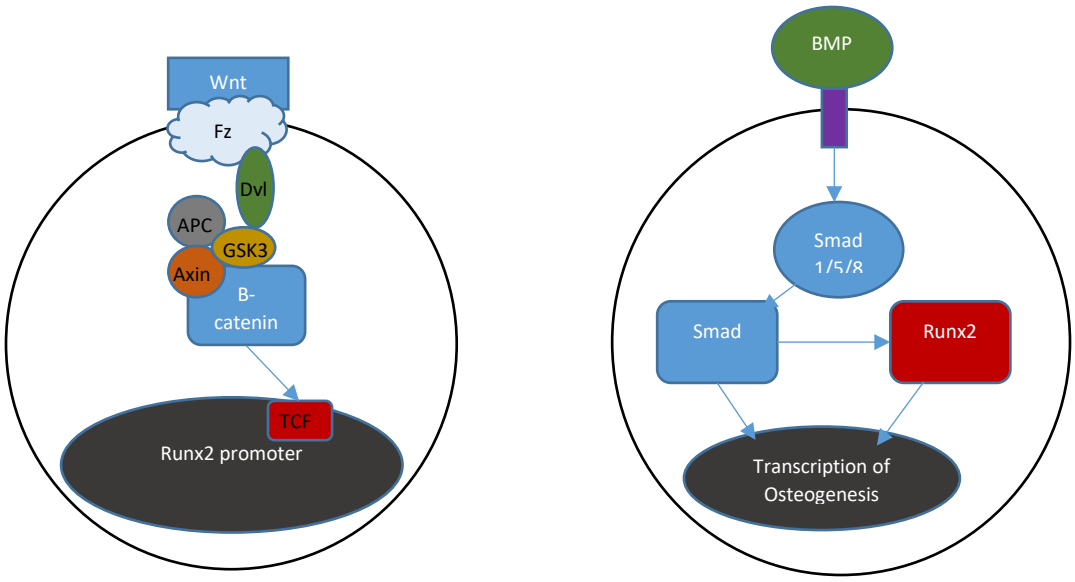

Figure 4. Schematic illustrating Runx2 expression via wnt signaling pathway (left), and induction of Smad pathway to promote osteogenic gene expression (right).

The combination of plasmon-phonon exchange with thermally labile linkers, provides a unique minimally invasive tool to modulate progenitor differentiation in tissue at specific spatial junctions. While the nanoparticle vehicle or cells transfected with them may diffuse *in vivo*, they remain inert until activated, which can be spatially constrained. Also, since miRNA mimics are short lived and only transiently modulate mRNA expression there is little chance of permanent activity once an activated cell has begun differentiation. The miRNA mimics associated with inactivated miRNA-particle systems are expected to degrade slowly intracellularly or in the intercellular space through enzymatic action or hydrolysis. The development of this technology represents a paradigm shift in achieving sequential delivery of multiple therapeutics, and the instigation of differentiation with fine spatial control in situ. The ability to spatially stimulate differentiation of alternate tissue sections can potentially overcome the challenge associated with producing graded interfaces for better tissue/organ functionality. This technology addresses a critical limitation of current non-coding RNA delivery methods that do not control spatiotemporal expression, resulting in severe off-target activity and side effects.

References

[1] A. Z. Wilczewska, K. Niemirowicz, K. H. Markiewicz and H. Car, "Nanoparticles as drug delivery systems," Pharmacological reports, vol. 64, pp. 1020-37, 2012.

[2] F. Alexis, J. Zeng and S. W, "PEI Nanoparticles for Targeted Gene Delivery," CSH Protoc, vol. 1, 2006.

[3] Y. Qu, J. Yang, P. Zhan, S. Liu, K. Zhang, Q. Jiang, C. Li and B. Ding, "Self-Assembled DNA Dendrimer Nanoparticle for Efficient Delivery of Immunostimulatory CpG Motifs," ACS Appl Mater Interfaces, vol. 9, no. 24, pp. 20324-29, 2017.

[4] S. Medina, M. Michie, M. SE, M. Schnermann and J. Schneider, "Fluorous Phase-Directed Peptide Assembly Affords Nano-Peptisomes Capable of Ultrasound-Triggered Cellular Delivery," Angew. Chem., Int. Ed., vol. 56, no. 38, pp. 11404-8, 2017.

[5] M. Wierzbicki, S. Jaworski, M. Kutwin, M. Grodzik, B. Strojny, N. Kurantowicz and E. Sawosz, "Diamond, graphite, and graphene oxide nanoparticles decrease migration and invasiveness in glioblastoma cell lines by impairing extracellular adhesion," Int J Nanomedicine, vol. 12, pp. 7241-54, 2017.

[6] Y. Wang, Q. Zhao, N. Han, L. Bai, J. Li, J. Liu, E. Che, L. Hu, Q. Zhang, T. Jiang and S. Wang, "Mesoporous silica nanoparticles in drug delivery and biomedical applications," Nanomedicine, vol. 11, no. 2, pp. 313-27, 2015.

[7] M. Arruebo, F.-P. R, M. Ibarra and J. Santamaría, "Magnetic nanoparticles for drug delivery," Nano Today, vol. 2, no. 3, pp. 22-32, 2007.

[8] C. Ventola, "Progress in Nanomedicine: Approved and Investigational Nanodrugs," P T, vol. 42, no. 12, pp. 742-55, 2017.

[9] H. Cabrala and K. Kazunori, "Progress of drug-loaded polymeric micelles into clinical studies," J. Controlled Release, vol. 190, no. 28, pp. 465-476, 2014.

[10] D. Lombardo, P. Calandra, D. Barreca, S. Magazù and M. A. Kiselev, "Soft Interaction in Liposome Nanocarriers for Therapeutic Drug Delivery," Nanomaterials, vol. 6, no. 125, 2016.

[11] J. Connor, S. Sullivan and L. Huang, "Monoclonal antibody and liposomes," Pharmacology & Therapeutics, vol. 28, no. 3, pp. 341-65, 1985.

[12] M. L. Immordino, F. Dosio and L. Cattel, "Stealth liposomes: review of the basic science, rationale, and clinical applications, existing and potential," Int J Nanomedicine, vol. 1, no. 3, pp. 297-315, 2006.

[13] T. Allen and P. Cullis, "Liposomal drug delivery systems: from concept to clinical applications.," Adv. Drug Deliv. Rev., vol. 63, pp. 36-48, 2013.

[14] A. Grafmuller, J. Shillcock and R. Lipowsky, "Pathway of membrane fusion with two tension-dependent energy barriers.," Phys. Rev. Lett., vol. 98, no. 21, p. 218101, 2007.

[15] P. Cuatrecasas and T. Roth, "Receptor-Mediated Endocytosis, Receptors and Recognition," Springer, vol. 15, 1983.

[16] T. Ishida, H. Harashima and H. Kiwada, "Interactions of liposomes with cells in vitro and in vivo: Opsonins and receptors.," Curr. Drug Metab. , vol. 2, pp. 397-409, 2001.

[17] C. Hunt, "Liposomes disposition in vivo V. Liposome stability in plasma and implications for drug carrier function," Biochim Biophys Acta, vol. 719, no. 3, pp. 450-63, 1982.

[18] K. Mohr, S. Müller, L. Müller, K. Rusitzka, S. Gietzen, H. Frey and M. Schmidt, "Evaluation of Multifunctional Liposomes in Human Blood Serum by Light Scattering," Langmuir, vol. 30, no. 49, pp. 14954-62, 2014.

[19] a. B. A. T. I. S. J. S. G. L. F. X. G. E. L.-N. J. Jianjun Cheng, B. Teply, I. Sherifi, J. Sung, G. Luther, F. Gu, E. Levy-Nissenbaum, A. Radovic-Moreno, R. Langer and O. Farokhzad, "Formulation of Functionalized PLGA-PEG Nanoparticles for In Vivo Targeted Drug Delivery," Biomaterials, vol. 28, no. 5, pp. 869-876, 2007.

[20] A. Albisa, E. Piacentini, V. Sebastian, M. Arruebo, J. Santamaria and L. Giorno, "Preparation of Drug-Loaded PLGA-PEG Nanoparticles by Membrane-Assisted Nanoprecipitation," Pharm Res, vol. 34, no. 6, pp. 1296-1308, 2017.

[21] J. Chan, P. Valencia, L. Zhang, R. Langer and O. Farokhzad, "Polymeric nanoparticles for drug delivery," Methods Mol Biol, vol. 624, pp. 163-75, 2010.

[22] E. Blanco, H. Shen and M. Ferrari, "Principles of nanoparticle design for overcoming biological barriers to drug delivery," Nat Biotechnol, vol. 33, no. 9, pp. 941-51, 2016.

[23] M. Lundqvist, J. Stigler, G. Elia, I. Lynch, T. Cedervall and K. Dawson, "Nanoparticle size and surface properties determine the protein corona with possible implications for biological impacts," Proc. Natl. Acad. Sci. U. S. A., vol. 105, no. 38, pp. 14265-70, 2008.

[24] M. Rai, D. Nagaonkar and A. P. Ingle, "Metal Nanoparticles as Therapeutic Agents: A Paradigm Shift in Medicine," in Metal Nanoparticles: Synthesis and Applications in Pharmaceutical Sciences, Wiley-VCH Verlag GmbH & Co. KGaA, 2018, pp. 33-44.

[25] V. Mody, R. Siwale, A. Singh and H. Mody, "Introduction to metallic nanoparticles," J Pharm Bioallied Sci, vol. 2, no. 4, pp. 282-89, 2010.

[26] B. Yogesh, B. Vineeta, N. Rammesh and P. Saili, "Biosynthesized Platinum Nanoparticles Inhibit the Proliferation of Human Lung-Cancer Cells in vitro and Delay the Growth of a Human Lung-Tumor Xenograft in vivo," J Pharmacopuncture, vol. 19, no. 2, pp. 114-21, 2016.

[27] H. Norouzi, K. Khoshgard and F. Akbarzadeh, "In vitro outlook of gold nanoparticles in photo-thermal therapy: a literature review.," Lasers Med Sci., vol. 33, no. 4, pp. 917-26, 2018.

[28] O. Gobbo, F. Wetterling, P. Vaes, S. Teughels, F. Markos, D. Edge, C. Shortt, K. Crosbie-Staunton, M. Radomski, Y. Volkov and A. Prina-Mello, "Biodistribution and pharmacokinetic studies of SPION using particle electron paramagnetic resonance, MRI and ICP-MS.," Nanomedicine, vol. 10, no. 11, pp. 1751-60, 2015.

[29] F. Thibaudau, "Ultrafast Photothermal Release of DNA from Gold Nanoparticles," The Journal of Physical Chemistry Letters, vol. 3, pp. 902-907, 2012.

[30] E. Crew, S. Rahman, A. Razzak-Jaffar, D. Mott, M. Kamundi, G. Yu, N. Tchah, J. Lee, M. Bellavia and C.-J. Zhong, "MicroRNA Conjugated Gold Nanoparticles and Cell Transfection," Analytical Chemistry, vol. 84, no. 1, pp. 26-29, 2012.

[31] N. Gunduz, H. Ceylan, M. O. Guler and A. B. Tekinay, "Intracellular Accumulation of Gold Nanoparticles Leads to Inhibition of Macropinocytosis to Reduce the Endoplasmic Reticulum Stress," Scientific Reports, vol. 7, p. 40493, 2017.

[32] L. E. Cole, R. D. Ross, J. M. Tilley, T. Vargo-Gogola and R. K. Roeder, "Gold nanoparticles as contrast agents in x-ray imaging and computed tomography," Nanomedicine, vol. 10, no. 2, 2015.

[33] N. S. Abadeer and C. J. Murphy, "Recent Progress in Cancer Thermal Therapy Using Gold," The Journal of Physical Chemistry C, vol. 120, pp. 4691-4716, 2016.

[34] A. T. Qureshi, A. Doyle, C. Chen, D. Coulon, V. Dasa, F. D. Piero, B. Levi, W. T. Monroe, J. M. Gimble and D. J. Hayes, "Photoactivated miR-148b–nanoparticle conjugates improve closure of critical size mouse calvarial defects," Acta Biomaterialia, vol. 12, pp. 166-173, 2015.

[35] X. Liu, M. Atwater, J. Wang and Q. Huo, "Extinction coefficient of gold nanoparticles with different sizes and different capping ligands," Colloids Surf., B, vol. 58, no. 1, pp. 3-7, 2007.

[36] M. Hlaing, B. Eigzabher, A. Roa, A. Marcano, D. Radu and C. Lai, "Absorption and scattering cross-section extinction values of silver nanoparticles," Opt. Mater., vol. 58, pp. 439-44, 2016.

[37] H. Ammari, Y. Deng and P. Millien, "Surface Plasmon Resonance of Nanoparticles and Applications in Imaging," Arch. Rational Mech. Anal., vol. 220, pp. 109-53, 2016.

[38] Z. Starowicz, R. Wojnarowska-Nowak, P. Ozga and E. Sheregii, "The tuning of the plasmon resonance of the metal nanoparticles in terms of the SERS effect," Colloid Polym. Sci., vol. 296, no. 6, pp. 1029-37, 2018.

[39] O. A. Marcano, "Photothermal Determination of Absorption and Scattering Spectra of Silver Nanoparticles," Appl Spectrosc, vol. 72, no. 2, pp. 234-40, 2018.

[40] H. Norouzi, K. Khoshgard and F. Akbarzadeh, "In vitro outlook of gold nanoparticles in photo-thermal therapy: a literature review," Lasers Med Sci, vol. 33, no. 4, pp. 917-26, 2018.

[41] K. Willets and R. Van Duyne, "Localized Surface Plasmon Resonance Spectroscopy and Sensing," Annu. Rev. Phys. Chem., vol. 58, no. 1, pp. 267-297, 2007.

[42] M. L. Brongersma, N. J. Halas and P. Nordlander, "Plasmon-induced hot carrier science and technology," Nat. Nanotechnol., vol. 10, pp. 25-34, 2015.

[43] M. Geneviève and B. Labrousse, "The Auger Effect," Microsc Microanal Microstruct, vol. 6, pp. 253-262, 1995.

[44] X. Li, D. Xiao and Z. Zhang, "Landau Damping of Quantum Plasmons in Metal Nanostructures," New J. Phys. , vol. 15, no. 2, p. 023011, 2013.

[45] X. Zhang, X. Li, M. Reish, D. Zhang, N. Su, Y. Gutierrez, F. Moreno, W. Yang, H. Everitt and J. Liu, "Plasmon-Enhanced Catalysis: Distinguishing Thermal and Nonthermal Effects," Nano Lett., vol. 18, no. 3, pp. 1714-23, 2018.

[46] A. Manjavacas, J. Liu, V. Kulkarni and P. Nordlander, "Plasmon-Induced Hot Carriers in Metallic Nanoparticles," ACS Nano, vol. 8, no. 8, pp. 7630-38, 2014.

[47] A. Zahr, M. de Villiers and M. Pishko, "Encapsulation of Drug Nanoparticles in Self-Assembled Macromolecular Nanoshells," Langmuir, vol. 21, no. 1, pp. 403-10, 2005.

[48] S. Walker, M. Kennedy and J. Zasadzinski, "Encapsulation of bilayer vesicles by self-assembly," Nature, vol. 387, pp. 61-64, 1997.

[49] D. Zhao, J. Xu, X. Yi, Q. Zhang, S. Cheng, R. Zhuo and F. Li, "pH-Activated Targeting Drug Delivery System Based on the Selective Binding of Phenylboronic Acid," ACS Appl. Mater. Interfaces, vol. 8, no. 23, pp. 14845-54, 2016.

[50] R. Sawant and V. Vladimir P. Torchilin, "Challenges in Development of Targeted Liposomal Therapeutics," AAPS J, vol. 14, no. 2, pp. 303-315, 2012.

[51] C. J and H. L, "pH-sensitive immunoliposomes as an efficient and target-specific carrier for antitumor drugs," Cancer Res, vol. 46, no. 7, pp. 3431-5, 1986.

[52] L. Liang and D. Astruc, "The copper(I)-catalyzed alkyne-azide cycloaddition (CuAAC) “click” reaction and its applications. An overview," Coord Chem Rev, vol. 255, no. 23-24, pp. 2933-45, 2011.

[53] G. M and B. FP, "The Diels-Alder Reaction: A Powerful Tool for the Design of Drug Delivery Systems and Biomaterials," European Journal of Pharmaceutics and Biopharmaceutics, vol. 97, pp. 438-453, 2015.

[54] S. I. Presolski, V. P. Hong and M. Finn, "Copper-Catalyzed Azide–Alkyne ClickChemistry for Bioconjugation," Current Protocol in Chemical Biology, vol. 3, pp. 153-162, 2011.

[55] M. J. S. Dewar and A. B. Pierini, "Mechanism of the Diels-Alder reaction. Studies of the addition of maleic anhydride to furan and methylfurans," Journal of the American Chemical Society, vol. 106, no. 1, pp. 203-208, 1984.

[56] S. Yamashita, H. Fukushima, Y. Niidome, T. Mori, Y. Katayama and T. Niidome, "Controlled-Release System Mediated by a Retro Diels–Alder Reaction Induced by the Photothermal Effect of Gold Nanorods," Langmuir, vol. 27, no. 23, pp. 14621-14626, 2011.

[57] B. AB, H. D, J. G, G. BD and B. NR, "An Efficient Method Based on the Photothermal Effect for the Release of Molecules from Metal Nanoparticle Surfaces," Angewandte Chemie (International ed. in English), vol. 48, pp. 4166-4169, 2009.

[58] W. R.B. and K. T.J., "The Mechanism of the Diels-alder Reaction," Tetrahedron Letters, vol. 1, no. 5, pp. 19-21, 1959.

[59] J. M. Hurng, M. P. Kurylo, G. W. Marshall, S. M. Webb, M. I.Ryder and S. P. Ho, "Discontinuities in the Human Bone-PDL-Cementum Complex," Biomaterials, vol. 32, no. 29, p. 7106–7117, 2011.

[60] Q. Wang, J. Yan, J. Yang and B. Li, "Nanomaterials Promise Better Bone Repair," Materials Today, vol. 19, no. 8, pp. 451-63, 2016.

[61] W. G. D. Long, T. A. Einhorn, K. Koval, M. McKee, W. Smith, R. Sanders and T. Watson, "Bone grafts and bone graft substitutes in orthopaedic trauma surgery. A critical analysis.," The Journal of Bone and Joint Surgery, vol. 89, no. 3, pp. 649-58, 2007.

[62] E. R. CARLISLE and J. S. FISCHGRUND, "CHAPTER 27 - Bone Graft and Fusion Enhancement," in Surgical Management of Spinal Deformities, Elsevier, 2009, pp. 443-48.

[63] R. E. Tomlinson and M. J. Silva, "Skeletal Blood Flow in Bone Repair and Maintenance," Bone Research, vol. 1, pp. 311-322, 2013.

[64] K. Kapinas and A. Delany, "MicroRNA biogenesis and regulation of bone remodeling," Arthritis Research & Therapy, vol. 13, no. 3, pp. 220-230, 2011.

[65] B. Jia, Z. Zhang, X. Qiu, H. Chu, X. Sun, X. Zheng, J. Zhao and Q. Li, "Analysis of the miRNA and mRNA involved in osteogenesis of adipose-derived mesenchymal stem cells," Exp Ther Med, vol. 16, no. 2, pp. 1111-20, 2018.

[66] A. van Wijnen, J. van de Peppel, J. van Leeuwen, J. Lian, G. Stein, J. Westendorf and S. Kakar, "MicroRNA Functions in Osteogenesis and Dysfunctions in Osteoporosis," Curr Osteoporos Rep, vol. 11, no. 2, pp. 72-82, 2013.

[67] Z. Zhong, Z. Dong, L. Yang and Z. Gong, "miR-21 induces cell cycle at S phase and modulates cell proliferation by down-regulating hMSH2 in lung cancer," Journal of Cancer Research and Clinical Oncology, vol. 138, no. 10, pp. 1781-8, 2012.

[68] A. Qureshi, W. Monroe, V. Dasa, J. Gimble and D. Hayes, "miR-148b Nanoparticle Conjugates for Light Mediated Osteogenesis of Human Adipose Stromal/Stem Cells," Biomaterials, vol. 34, no. 31, pp. 7799-810, 2013.

[69] A. Schoolmeesters, T. Eklund, D. Leake, A. Vermeulen, Q. Smith, S. F. Aldred and Y. Fedorov, "Functional Profiling Reveals Critical Role for miRNA in Differentiation of Human Mesenchymal Stem Cells," PLoS One, vol. 4, no. 5, p. e5605, 2009.

[70] K.-C. Li, S.-C. Lo, L.-Y. Sung, Y.-H. Liao, Y.-H. Chang and Y.-C. Hu, "Improved calvarial bone repair by hASCs engineered with Cre/loxP-based baculovirus conferring prolonged BMP-2 and MiR-148b co-expression," Tissue Eng. Regen. Med., vol. 11, pp. 3068-77, 2017.

[71] J. Xu, W. Zhang, Q. Lv and Z. D, "Overexpression of miR-21 promotes the proliferation and migration of cervical cancer cells via the inhibition of PTEN," Oncol Rep., vol. 33, no. 6, pp. 3108-16, 2015.

[72] D. Sekar, S. Saravanan, K. Karikalan, K. Thirugnanasambantham, P. Lalitha and V. Islam, "Role of microRNA 21 in mesenchymal stem cell (MSC) differentiation: a powerful biomarker in MSCs derived cells," Curr Pharm Biotechnol., vol. 16, no. 1, pp. 43-8, 2015.

[73] J. Zhang, J. Wang, F. Zhao, Q. Liu, K. Jiang and G. Yang, "MicroRNA-21 (miR-21) represses tumor suppressor PTEN and promotes growth and invasion in non-small cell lung cancer (NSCLC)," Clin Chim Acta., vol. 411, no. 11-12, pp. 846-52, 2010.

[74] S. SK, A. Marisetty, P. Sathyan, M. Kagalwala, Z. Zhao and S. Majumder, "REST-miR-21-SOX2 axis maintains pluripotency in E14Tg2a.4 embryonic stem cells," Stem Cell Res., vol. 15, no. 2, pp. 305-11, 2015.

[75] X. Li, L. Guo, Y. Liu, Y. Su, Y. Xie, J. Du, J. Zhou, G. Ding, H. Wang, Y. Bai and Y. Liu, "MicroRNA-21 promotes osteogenesis of bone marrow mesenchymal stem cells via the Smad7-Smad1/5/8-Runx2 pathway," Biochem Biophys Res Commun., vol. 493, no. 2, pp. 928-33, 2017.

[76] Y. Kim, S. Hwang, Y. Bae and J. Jung, "MiR-21 regulates adipogenic differentiation through the modulation of TGF-beta signaling in mesenchymal stem cells derived from human adipose tissue," Stem Cells, vol. 27, no. 12, pp. 3093-102, 2009.

CHAPTER 2.

Comparison of Thermally Actuated Retro-Diels-Alder Release Groups for Nanoparticle Based Nucleic Acid Delivery

Mohammad Abu-Laban[a], Raju R. Kumal[b], Jonathan Casey[a], Jeff Becca[c], Daniel LaMaster[b], Carlos N. Pacheco[c,d], Dan G. Sykes[c], Lasse Jensen[c], Louis H. Haber[b] and Daniel J. Hayes[a,e,f].*

[a]The Department of Biomedical Engineering, The Pennsylvania State University, University Park, Pennsylvania 16802. Email: mua323@psu.edu, jsc49@psu.edu.

[b]The Department of Chemistry, Louisiana State University, Baton Rouge, Louisiana 70803. Email: lhaber@lsu.edu, rkumal1@lsu.edu, dlamas1@lsu.edu.

[c]The Department of Chemistry, The Pennsylvania State University, University Park, Pennsylvania, 16802. Email: jensen@chem.psu.edu, jbb5516@psu.edu, djs12@psu.edu.

[d]The NMR Facility, The Pennsylvania State University, University Park, Pennsylvania, 16802. Email: cpacheco223@gmail.com

[e]Materials Research Institute, Materials Characterization Lab, Millennium Science Complex, The Pennsylvania State University, University Park, Pennsylvania 16802

[f]The Huck Institute of the Life Sciences, Millennium Science Complex, The Pennsylvania State University, University Park, Pennsylvania 16802

*Corresponding author: N242 Millennium Science Complex, The Pennsylvania State University, University Park, Pennsylvania 16802. Email: djh195@psu.edu. Phone: 814.865.0780.

Abstract

The present study explores alternate pericyclic chemistries for tethering amine-terminal biomolecules onto silver nanoparticles. Employing the versatile tool of the retro-Diels-Alder (rDA) chemistry, three thermally-labile cycloadducts are constructed that cleave at different temperature ranges. While the reaction between furan and maleimide has been reported, the current study also evaluates the reverse reaction kinetics between thiophene-maleimide, and pyrrole-maleimide cycloadducts. Density Functional Theorem (DFT) calculations used to model and plan the experiments, predict energy barriers for the thiophene-maleimide reverse reaction to be greatest, and the pyrrole-maleimide barriers the lowest. Based on the computational analyses, it is projected that the cycloreversion rate would occur slowest with the thiophene, followed by furan, and finally pyrrole would yield the promptest release. These thermally-responsive linkers, characterized by Electrospray Ionization Mass Spectrometry, ^{1}H and ^{13}C NMR, are thiol-linked to silver nanoparticles and conjugate a single strand siRNA mimic with a 5' fluorescein tag. Second harmonic generation spectroscopy (SHG) and fluorescence spectroscopy are used to measure release and rate of release. The SHG decay constants and fluorescence release profiles obtained for the three rDA reactions confirm the trends obtained from the DFT computations.

Keywords: retro-Diels-Alder, delivery, Second Harmonic Generation (SHG), nanoparticle, maleimide, pyrrole, thiophene, furan

Introduction

Delivery of short non-coding nucleic acid molecules as potential therapeutics has widely been investigated [1] [2] [3] [4] [5] [6] [7]. These molecules play a crucial role in regulating gene expression in numerous processes from embryonic to immune system development, and have been sought after as potential therapeutic agents relevant to human physiology and pathology. Clinical adoption, however, has been slow as a result of unidentified off-target effects as well as non-specific and inefficient delivery, requiring a high dosage for effective treatment. With the capability to respond to internal or external stimuli, nanoparticle delivery systems hold great promise for efficient spatiotemporal gene control of therapeutic delivery. Targeted delivery and release of therapeutics can be initiated via physical, chemical, or mechanical cues. Nanoparticle systems designed for nucleic acid caging and controlled release include polymer-based media [8], surface-linked or encapsulated nanoparticles [7] [9], liposomal and viral vectors [10] [11]. These systems can be tailored to employ various cues for nucleic acid delivery at targeted sites, such as pH change [12], temperature [13] or electromagnetic-mediated stimuli [14]. Most of these methods rely on the linker or substrate chemical nature for stimuli response and drug release, typically through bond breaking and rearrangement.

For efficient temporal manipulation of small molecules and siRNA, click chemistry, most commonly reported between an azide and alkyne, can provide bioconjugation abilities of biomolecules with specific systems providing a switch-like trigger for molecular release. These reactions are wide in scope, but pertain to reactions proceeding under mild conditions to give high yields and innocuous by-products [15] [16]. Diels-Alder reactions meet this criteria, and involve formation of a cycloadduct product derived from a dienophile and diene in which more stable σ-bonds are formed from [4+2] π-bonds, based on overlapping electron levels between

higher and lower occupied and unoccupied molecular orbitals [17] [18] [19]. At higher temperatures the cyloaddition reactions undergo reverse reaction pathways, referred to as the retro-Diels-Alder (rDA) reaction, to reproduce their diene and dienophile counterparts [20] [21] [22]. In Bakhtiari et al. [23], it was demonstrated that the cycloadduct between a furan and maleimide could be synthesized at room temperature over seven days, with the rDA reaction observed to occur at temperatures 60 °C and above. Using gold nanoparticles modified with fluorescein-tagged furan-maleimide linkers and irradiated at their plasmonic wavelength of 532 nm, an increase in solution fluorescence was observed due to localized plasmon-phonon heat generation triggering the rDA reaction and releasing the markers. Other groups have utilized chiral auxiliary synthesis methods for enantiomer-selectivity of pyrrole-pyrimidine ring structures and microwave-inducible rDA reaction [24] [25] [26]. The rDA chemistry is a versatile tool for the delivery of short biological molecules utilizing simple chemical modifications, and providing a stimuli-responsive switch to trigger cargo release based on localized heat induction. By designing multiple linkers with alternate thermal responses, temporal delivery of more than one drug for gene therapy can be achieved.

The Diels-Alder forward reaction can be facilitated via an electron-enriched diene with an electron-poor dienophile, where each molecule is typically substituted with electron-donating and electron-withdrawing groups, respectively [27]. In the current study, we aim to build on the chemistry investigated previously [23], in which the bond breaking of 7-oxa-bicyclo-[2.2.1]hept-5-ene-2,3-dicarboxylic imide was studied, and explore the bicyclic reactions of alternate dienes and attain distinct temperature ranges in which to initiate the rDA reaction, for the purpose of multiplex delivery applications. In addition to the described furan-maleimide composition, substitution of the furan with both a pyrrole and thiophene-based diene was investigated,

utilizing chemical modifications of the cycloadduct with a thiol terminal for nanoparticle conjugation, and a carboxyl terminal group for crosslinking with amine-modified nucleic acids (**Figure 1**). Density functional theory was used to model the reaction barriers at various temperatures for the three different diene reactions with maleimide to aid in the rational design of the system and experimental conditions. To measure the rDA rates for each of the model compounds, second harmonic generation spectroscopy was utilized for nanoparticle surface measurements; the first time the technique is used, to our knowledge, to analyze the reversion of the DA linker.

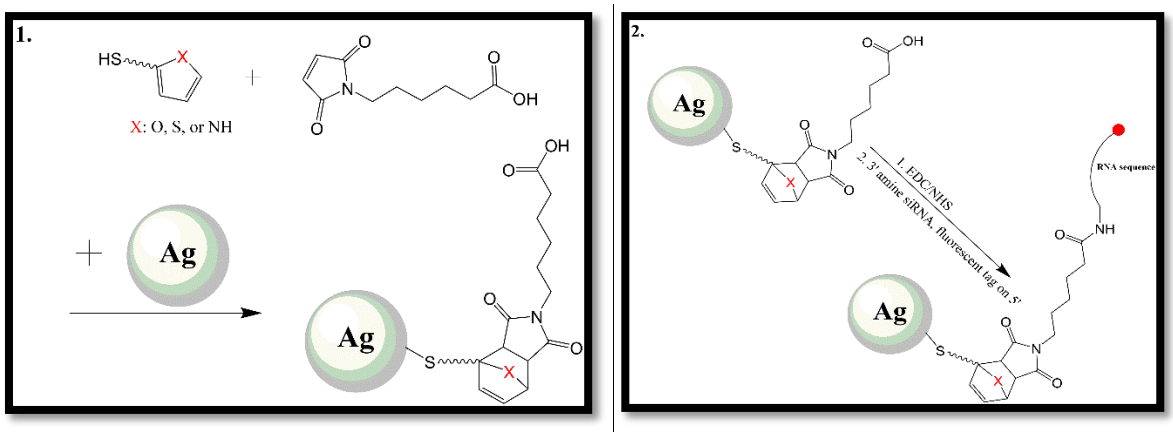

Figure 1. Overall schematic illustrating pericyclic reaction between dienes with 6-maleimidohexanoic acid and conjugation onto nanoparticle via generic thiol linkage (1). EDC coupling chemistry was utilized to link amine-terminated siRNA to nanostructure (2).

Materials & Methods

6-Maleimidohexanoic acid (90%), 2-furanmethanethiol (98%), 2-thienylmethanethiol, pyrrole-2-carboxylic acid (99%), dichloromethane (DCM) (99.8%), methanol (MeOH) (>99.9%), cysteamine (95%), N-hydroxysuccinimide (NHS) (98%), silver nitrate (99%), formaldehyde (36.5-38%), sodium hydroxide (98%, pellets), hydroxypropyl cellulose (HPC) (Mn=80,000, 99%), antifoam A (100%), tris(2-carboxyethyl)phosphine hydrochloride solution (TCEP) (0.5M) and dimethyl sulfoxide-d6 (99.9%) were all received from Sigma Aldrich (St. Louis, MO). EDC

(1-ethyl-3-(3-dimethylaminopropyl) carbodiimide hydrochloride) was purchased from Thermo Fisher Scientific (Waltham, MA), and custom 3'-amine/ 5'-FAM modified anti-sense RFP single stranded siRNA (UUGGAGCCGUACUGGAACUUG) were purchased from Sangon Biotech (Shanghai, China). All reagents were used as received. A mounted 405 nm LED light (1500mW) from ThorLabs, Inc. (Newton, NJ) was utilized for photorelease experiments.

Computational methods:

DFT computations were performed prior to experimentation. The optimized geometry, normal mode analysis, thermodynamic properties, and reaction barriers were calculated using the NWChem (v6.6) software package [28] at a B3LYP and 6-311G* level of theory [29]. Reduced atom models for the maleimide were used to ensure no negative vibrational modes for reactants and products, and just one large negative vibrational mode for the transition states. Optimizations were done using tighter criteria for the gradient, gradient maximum and root mean square, and Cartesian step maximum and root mean square. Settings for transition state searches were performed using optimized structures of the reactants initially constrained to a distance of 2.4 Å for the reacting carbon atoms. The thermodynamic data and zero point energies were obtained from the normal mode analysis calculations at 25, 40, 60, and 80 ˚C. All calculations were performed as gas phase, ignoring solvent effects.

Synthesis of nanoparticles:

Colloidal silver nanoparticles (SNPs) were prepared as described in [30] which yielded nanoparticles of 75 nm in diameter size in that study. Briefly, at room temperature 35 mL of each 125 mM silver nitrate ($AgNO_3$) and 61.5 mM formaldehyde (HCOH) were incrementally added 0.5 mL/min into a pre-made solution consisting of 0.5 g NaOH, 0.31 g HPC, 330 mL deionized (DI) water (18.2 MΩ), and 5 µL Antifoam A. For purification, the nanoparticles were filtered via

dialysis and freeze-dried under vacuum for 72 h before use. A stock solution of 200 ppm in DI water was later prepared for further chemical modification.

Synthesis of Diels-Alder linkers & siRNA attachment:

For the cycloaddition between 6-maleimidohexanoic acid and 2-furanmethanethiol, the protocol outlined in [23] was followed with minor modifications. Briefly, 4.18 g of the dienophile, the maleimide, was combined with 1 mL of the diene reagent, in a 1:1 (v/v) DCM:MeOH solvent mixture. The reaction was allowed to proceed for 7 days under agitating conditions at room temperature in a sealed container. For the Diels-Alder reactions between the 2-thienylmethanethiol (0.5 mL) and the 6-maleimidohexanoic acid (2.11 g), and the pyrrole-2-carboxylic acid (0.555 g) and 6-maleimidohexanoic acid (2.11 g), the reagents were again mixed together in MeOH-only solvent. Both the reactions for the pyrrole and thiophene were carried out in an oil bath at 60 ˚C for 3 days under controlled ventilation. The bicyclic products between the different dienes and dienophile were purified by High Performance Liquid Chromatography (HPLC) and characterized via ESI MS, ^{1}H and ^{13}C NMR. For SNP attachment, the solutions were simply dried with nitrogen gas to remove excess solvent and concentrate the sample prior to suspension, without HPLC purification. Additionally, in the case of the pyrrole-2-carboxylic acid Diels-Alder reaction, the diene was first crosslinked with cysteamine using EDC coupling chemistry for SNP modification. Briefly, EDC (0.500 g), NHS (0.800 g) and cysteamine (0.400 g) were added to the pyrrole-2-carboxylic acid (0.555 g) and agitated overnight at room temperature. After centrifugation of the 1 mL-aliquoted SNPs (10,000 rpm, 15 min) and removal of the supernatant, 0.5 mL of the Diels-Alder products were added directly to the pelleted nanoparticles. The NP surface modification step was left to proceed at room temperature for 24 hours, for all the three generated products. The nanoparticles were then washed thrice by

centrifuging for 10 min at 10,000 rpm consecutively, in which each step involved removal of the supernatant and resuspension in 1 mL of 70 % (v/v) ethanol. To conjugate the FAM-tagged RFP antisense siRNA mimic, the EDC coupling protocol was again used with 100 μL of an aqueous EDC/NHS (100 mM) stock solution added to each of the resuspended nanoparticle aliquots followed by 50 μL of the amine-terminated siRNA (4 μM). After 24 hours, the particles were again centrifuged, washed, and resuspended in DI water. A control sample in which cysteamine modified SNPs were linked to the 6-maleimidohexanoic acid via EDC coupling was also prepared, similarly to the pyrrole-based reaction described above but without addition of the diene, to test the stability of both the amide and thiol linkages. Conjugation of the linkers and siRNA was tested by chemically reducing the Ag-SR bond using TCEP reagent and measuring FAM intensity of the supernatant.

Water-bath heating:

The siRNA-functionalized nanoparticles were placed in a water bath and heated at 3 different temperatures, 40, 60, and 80 ˚C, each for duration of 2 h. Release of the siRNA at each temperature was quantified by measuring FAM fluorescence intensity of the supernatant at 485/520 nm (ex/em) (Spectramax M5 Microplate/Cuvette Reader, Molecular Devices, Pennsylvania, USA), and normalizing to TCEP-treated samples. All fluorescence measurements were also measured against a non-treated sample consisting of modified nanoparticles, to take into account any freely dispersed siRNA. The supernatant of the non-treated sample was established as the baseline and subtracted from the values plotted for all samples.

Second Harmonic Generation measurements:

The experimental setup for SHG measurement has been described previously [31]. Briefly, the experimental setup consisted of a Ti: sapphire oscillator laser having 800 nm central

wavelength, 80 MHz repetition rate and 70 fs pulse duration with an average power of 2.5 W. For SHG measurements, the 800 nm probe laser at an attenuated, average power of 300 mW was focused into a 1 cm × 1 cm quartz cuvette containing the sample. The SHG signal from the siRNA-SNP complex was collected in the forward direction in real-time at different sample temperatures using heating tape. A LabVIEW program was used to control a magnetic stir bar, beam block to open and shut every 15 s and to collect background-subtracted time-dependent SHG spectroscopic measurements.

Light activated photothermal release:

SNP samples surface-modified with each of the three different Diels-Alder crosslinked with FAM-siRNA molecules were investigated for release via localized heating, by light irradiation at 405 nm using a mounted LED light source (measured output power of 1 W). Solutions of the modified SNPs were contained in a 35 mm Petri dish and irradiated from the bottom of the dish for 20, 40, 60, and 80 min time intervals. The suspension samples were then collected, centrifuged, washed and treated with TCEP to measure the remaining oligonucleotide on the surface of the nanoparticles, by measuring directly the FAM fluorescence intensity at 485 nm/525 nm (ex/em) in the supernatant. Bulk solution temperature during irradiation was measured with a T-type thermocouple.

High Performance Liquid Chromatography (HPLC):

Diluted samples of the three different products were injected (10 uL) through a Dursan®-coated stainless steel column packed at high pressure with a silica-C18 bed using a binary gradient Shimadzu UHPLC system. The mobile phase consisted of dual flow of acetonitrile and water, with the different compositions used for each DA product listed in the SI document.

Electron-Spray Ionization Mass Spectrometry:

Mass spectrometric analysis was performed on a Waters Q-TOF Premier quadrupole/time-of-flight (TOF) mass spectrometer (Waters Corporation (Micromass Ltd.), Manchester, UK). Operation of the mass spectrometer was performed using MassLynx™ software Version 4.1 (http://www.waters.com). Samples were introduced into the mass spectrometer using a Waters 2695 high performance liquid chromatograph. The samples were analyzed using flow injection analysis (FIA), in which the sample was injected into the mobile phase flow and passes directly into the mass spectrometer, where the analytes are ionized and detected. The mobile phase used was 90 % acetonitrile (LC-MS grade), and 10 % aqueous 10 mM ammonium acetate. The flow rate was 0.15 mL/min. The nitrogen drying gas temperature was set to 300 °C at a flow of 7 L/min. The capillary voltage was 2.8 kV. The mass spectrometer was set to scan from 100-100 m/z in both positive and negative ion modes, using electrospray ionization (ESI).

Results & Discussion

DFT Computations

DFT methods provide essential quantum mechanical computations of forward and reverse barriers and energies of reactions [32]. The structures used in the pericyclic reaction schemes for the B3LYP/6-311G* set are shown in **Table 1**, and an example input for one of the optimizations is included in the supporting information **(Table S1, Appendix A)**. The Gibbs free energy and enthalpy barriers are summarized in **Table 2**. For emphasis, in all three cases the same maleimide structure was used to link the dienes, with variation occurring with only the latter group. The data presented in **Table 2** portray a consistent pattern; higher energy barriers for ΔG and ΔH_{rxn} for the retro-Diels-Alder reaction with thiophene than either the pyrrole or furan, while the values for the former diene appear as the lowest. This trend holds true at all

temperatures with little variation. Based on the computations, it would suggest that the rDA reaction would occur at higher temperatures with the thiophene than the furan diene, while the pyrrole would initiate release at even lower temperatures.

Table 1. Optimized structures used for B3LYP/ 6-311G* computation. Yellow=S, Red=O, Black=C, Blue=N, White=H. Images rendered using PyMOL [33].

Diene	Maleimide	Transition State	Product
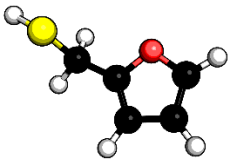 2-furanmethanethiol	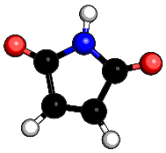	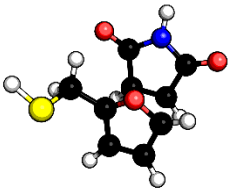	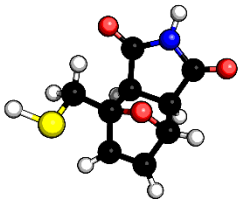
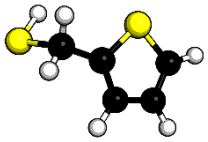 2-thienylmethanethiol	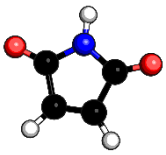	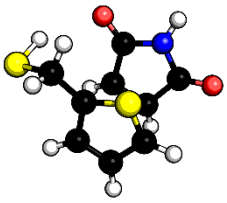	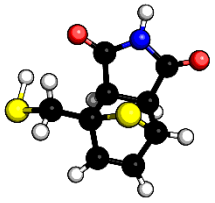
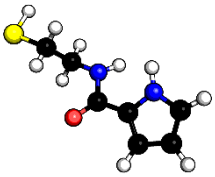 Pyrrole-2-carboxylic acid + cysteamine	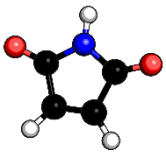	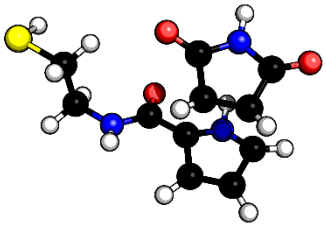	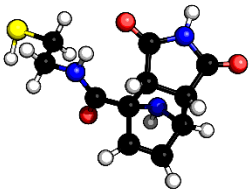

Table 2. Gibbs free energy & enthalpy reaction barriers generated from B3LYP/6-311G* theory.

Diene	Reaction	Reaction Barriers for ΔH_{rxn} kcal/mol				Reaction Barriers for ΔG kcal/mol			
		25 °C	40 °C	60 °C	80 °C	25 °C	40 °C	60 °C	80 °C
2-furanmethanethiol	Forward	21.32	21.33	21.34	21.36	35.56	36.28	37.23	38.18
	Reverse	23.15	23.17	23.19	23.21	21.82	21.75	21.66	21.57
2-thienylmethanethiol	Forward	28.66	28.67	28.67	28.68	43.88	44.65	45.67	46.69
	Reverse	30.42	30.43	30.45	30.47	29.32	29.26	29.19	29.11
Pyrrole-2-carboxylic acid + cysteamine	Forward	23.86	23.86	23.86	23.87	39.14	39.91	40.93	41.96
	Reverse	18.98	19.01	19.04	19.08	17.53	17.45	17.35	17.25

Synthesis of SNPs & Diels-Alder products

Characterization of the synthesized SNPs has previously been reported in Qureshi et al. [30] [34]. The HPC-stabilized nanoparticles' hydrodynamic diameter was determined to be 170 nm ± 1.46 with a zeta potential of -10.0 mV ± 0.41. Additionally, the UV-Vis spectra of the SNPs were collected and reported in the supporting information document **(Figure S1, Appendix A)**.

The furan-based Diels Alder reaction was performed similarly to the previous procedure [23]. The thiophene and pyrrole reactions, however, required elevated temperatures to proceed as the conditions used for the furan did not yield the desired products after the seven day period. The former two dienes are less electronegative than the furan and as a result possess increased aromaticity [35]. Previous reports have highlighted the difficulty of cycloaddition reactions involving thiophene as a result of its lack of reactivity [36]. Increased temperatures and pressures are required to overcome its reaction barrier to produce modest yields of bicyclic products [37].

Nanoparticle conjugation of the thermally-labile linkers was achieved via thiol-linkage. In the case of the pyrrole reaction, cross-linking of the molecule with cysteamine was performed for nanoparticle modification. The terminal thiol group on the bicyclic molecules allows for the facile Ag-SR functionalization on nanoparticle surfaces, as has been described elsewhere [38]. One important note to make is all three dienes are functionalized with a terminal thiol group that could potentially react directly with the maleimide. That thiol-maleimide reaction is a subclass of the thiol-Michael Addition click reactions, which are typically either base- or nucleophile-catalyzed [39] [40]. The former is unlikely to occur in the outlined reactions, as the Diels-Alder cycloaddtion was carried out at slightly acidic conditions at a measured mixture pH of 5-6. The dienes themselves are unlikely to be strong enough nucleophiles to react with the C=C bond on

the maleimide and remove the H from the –SH group to bond with the maleimide. But more importantly, the Diels-Alder cycloadduct was selected for by surface modification with the Ag NPs. The thiolate conjugation chemistry can only occur with free thiols or by reducing disulfides [38]. By-products from any thiol-maleimide reaction were likely washed away in the discarded supernatant as they were unable to bind to the nanoparticle surface. Yield values, electron-spray ionization mass spectrometry, ^{13}C and ^{1}H NMR analysis for the three Diels-Alder products, between 6-maleimidohexanoic acid and the furan-, thiophene-, and pyrrole-based dienes are reported in the supporting information document.

Water bath heating

The fluorescence intensities indicating FAM-siRNA release in the supernatant for all three samples, at the three different water bath temperatures are reported in **Figure 2**. The temperatures were selected for their physiological relevance, where higher local temperatures on nanoparticles may cause irreversible tissue damage and necrosis. The values shown were normalized to chemically reduced samples using TCEP. Normalized values were used to account for the variable particle loadings across the three different systems. The loading efficiencies for each system was determined, based on the ratio of siRNA NP-loading to the total added siRNA. These efficiencies for the furan, pyrrole, and thiophene DA were 83.43 % ±0.76, 77.84 % ±1.8, and 32.89 % ±0.24, respectively.

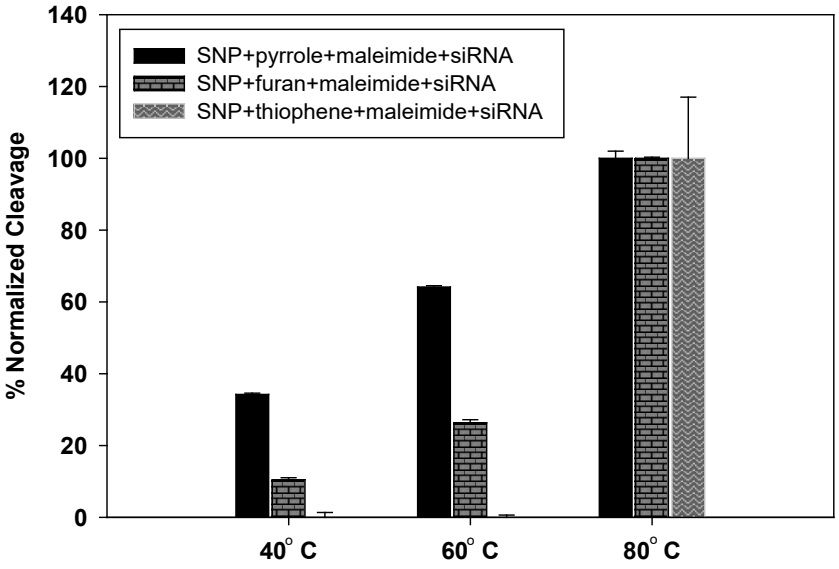

Figure 2. Normalized fluorescence of FAM-siRNA release from covalently-linked SNPs via retro-Diels-Alder reaction at different water bath temperatures, +/-SEM.

Based on the heating results, release of the pyrrole sample occurred most readily, even at the lowest applied temperature with 38% reversion, while release with the thiophene was not detected until 80 ˚C. All three DA structures were observed to fully release siRNA at 80 ˚C, after 2 h. The trend shown in **Figure 2** agrees with the computational results above **(Table 2)**, in which higher energy barriers are required for the reverse reaction to occur for the following reactions in specific order: thiophene > furan > pyrrole. At 60 °C, the pyrrole-malemide cycloadduct was synthesized at a yield of 23.8 wt% (Supporting Information), but undergoes cycloreversion at the same temperature at almost 65% conversion rate. This was likely due to a shift in equilibrium in the opposite direction in the different states. In the synthesis state, formation of the cycloadduct was aided by concentration buildup of the diene and excess maleimide, which at higher temperatures propelled the addition reaction to produce the DA linker. After conjugation to the particle, the presence of free diene and maleimide was removed, thus at the same temperature the equilibrium likely shifted further in the opposite direction to

cause the reversion. Additionally, the modification of the pyrrole with the nanoparticles and siRNA molecule will likely alter the kinetics of the linker compared to its simpler diene+dienophile construct during its synthesis. While furan-based cycloadducts have always been favored due to their susceptibility to break at lower temperatures, pyrrole's superior dienofugacity over furan is often overlooked, despite the lower activation energy for cycloreversion reported by other groups [41], as well as in the current study.

With regards to the activity and stability of the siRNA exposed at these temperatures, it was determined that single stranded siRNA integrity was maintained for short incubations up to 95 °C via gel electrophoresis and functional activity assay [42]. In the current study, the thiophene-based linker required temperatures of at least 80 °C for substantial release, while the pyrrole and furan DA discharge occurred at lower and physiologically safer temperatures. It is possible at extended localized heat the siRNA may degrade if it is not timely detached, in the case of the thiophene-based linker. However in all cases, heat dissipation from the surface is expected to decrease significantly away from the immediate surface [43], and thermal stresses should swiftly be reduced as the siRNA is detached and allowed to diffuse away from the surface of the nanoparticle down its chemical potential gradient.

Second Harmonic Generation

Second harmonic generation (SHG) is a surface-sensitive technique that can be used to study the buried interfaces within solids and liquids. It is a second order non-linear spectroscopic process in which two photons of frequency ω add coherently to generate a third photon of frequency 2ω [44] [45] [46]. However, SHG is a dipole forbidden process which does not generate from centrosymmetric and isotropic bulk media but can be generated from the interfaces where the inversion symmetry is broken. There is no SHG from randomly oriented

molecules in the bulk of the liquid but their attachment on the nanoparticle interfaces produces the SHG signal. The label-free probe technique of SHG spectroscopy has been used to study oligonucleotides at nanoparticle interfaces [47] [48], photocleaving dynamics from the surface of plasmonic nanoparticles [31] [49], binding of anti-cancer drug to DNA [50], and interfacial properties of nanoparticles [51] [52] [53]. The SHG signal is induced by the second-order polarization under an incident optical electric field E_ω characterized by the second-order and third-order nonlinear susceptibilities, $\chi^{(2)}$ and $\chi^{(3)}$, respectively. The total second harmonic electric field E_{SHG} is a coherent process given by the equation [31] [49] [53] [54],

$$E_{SHG} = \sqrt{I_{SHG}} = \chi^{(2)} E_\omega E_\omega + \chi^{(3)} E_\omega E_\omega \phi_0 \qquad (1)$$

where I_{SHG} is the SHG intensity and ϕ_0 is the interfacial electrostatic potential arising from the nanoparticle surface charge density in aqueous suspension. $\chi^{(2)}$ is the second-order susceptibility originating from the two-photon spectroscopy of the colloidal nanoparticle and the attached interfacial molecules. $\chi^{(3)}$ is the third-order susceptibility caused by polarized water molecules that are aligned by the static electric field near the nanoparticle surface.

The thermal release of siRNA from the surface of silver nanoparticles was studied in real time using second harmonic generation spectroscopy. Representative SHG spectra of SNP+pyrrole+maleimide+siRNA complex at 80 °C temperature are shown in **Figure 3a**. The SHG signal from the sample is centered at 400 nm with full width half maximum of 4.5 nm. The small rise in SHG intensity at longer wavelengths is due to two-photon fluorescence from the nanoparticle sample. The initial SHG intensity of the sample is larger due to the presence of cargo molecules on the surface of nanoparticles resulting primarily in higher $\chi^{(3)}$ contribution due to the negatively charged phosphate groups of the oligonucleotides which is consistent with our previous works [31] [49]. In fact, the use of a nucleic acid molecule as opposed to simply a

fluorophore molecule results in enhancement in SHG signal that allows for the observation of a clear and distinct reduction in signal upon cleavage. The decrease in SHG intensity under increasing heating time is due to the thermal release of siRNA from the colloidal SNP surface. A control experiment showing the variation of SHG intensity as a function of heating time for SNP+pyrrole+maleimide+siRNA and SNP+cysteamine+maleimide (no diene) complex at 80 °C is shown in **Figure 3c**. The latter experiment was to observe the thermal effect on the stability of the thiol linkage alone to the nanoparticles. Based on **Figure 3b**, it can be shown that at the highest temperature treatment, no observable SHG decay representative of linker release was detected for the control sample. In **3c**, the SHG intensity from SNP+cysteamine+maleimide complex is smaller (green), as a result of the smaller surface charge density and remains constant with time. This indicates that the thiol and amide bonds are stable enough over longer periods of time at 80 °C temperature. However, the SHG intensity from SNP+pyrrole+maleimide+siRNA complex decreases with time and reaches a minimum value. This minimum value of SHG intensity is equal to the SHG intensity from SNP+cysteamine+maleimide complex, indicating a complete thermal release of siRNA from the nanoparticle interface.

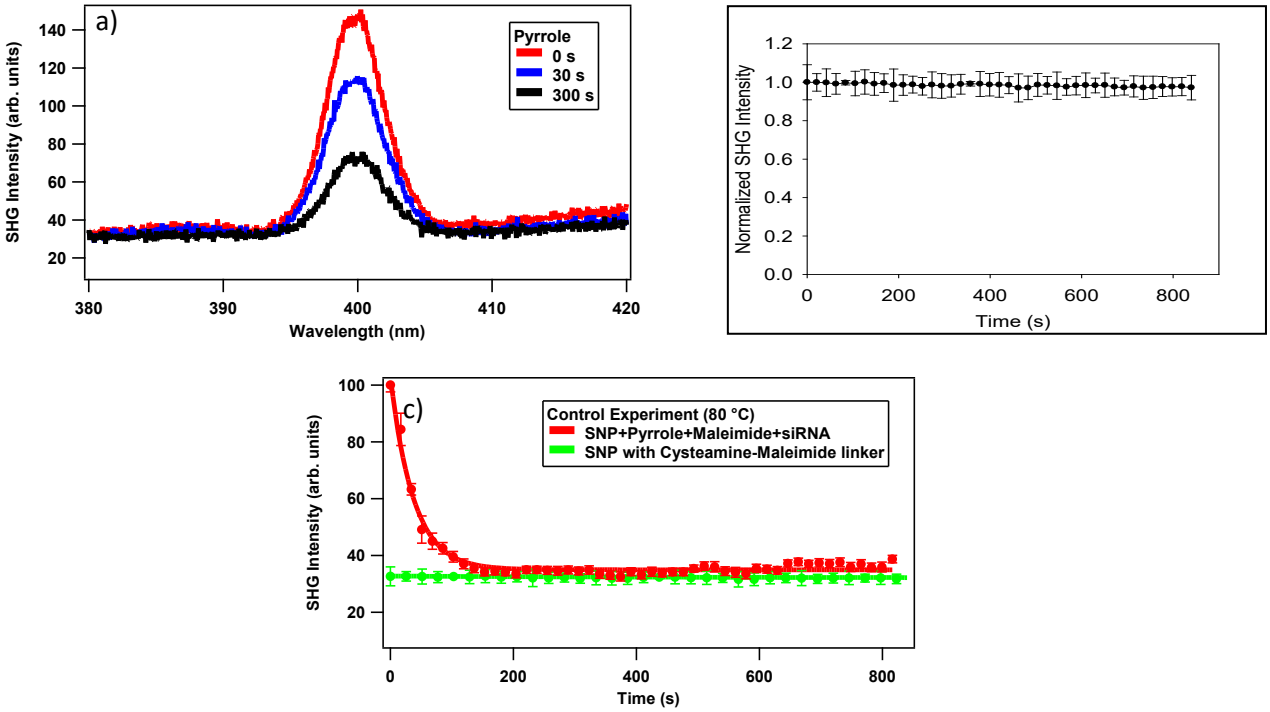

Figure 3. a) SHG spectra for SNP+pyrrole+maleimide+siRNA sample at 0, 30, and 300 s, b) normalized SHG spectra for control sample, SNP+cysteamine+maleimide, c) and real time decay of SHG maxima at 400 nm for SNP+pyrrole+maleimide+siRNA and SNP+cysteamine+maleimide linker, +/-SEM.

Time-dependent SHG spectroscopy was used to study the thermal release of siRNA at different temperatures for the three different complexes; SNP+pyrrole+maleimide+siRNA, SNP+furan+maleimide+siRNA and SNP+thiophene+maleimide+siRNA. **Figure 4a** shows the variation of SHG intensity from SNP+pyrrole+maleimide+siRNA complex at 40, 60 and 80 °C temperatures. The small changes in SHG intensity (1-2 %) at 40 °C is observed for all three complexes might be due to the unavoidable small photothermal effect generated by the nanoparticle itself in the presence of the probe laser resulting in miniscule release of siRNA. To minimize this effect, a fundamental laser source having minimum power was used, the threshold to generate SHG signal. However, there were significant changes in SHG intensities at 60 and 80 °C temperatures due to the thermal release of siRNA. Similarly, the release of siRNA from

the SNP+furan+maleimide+siRNA and SNP+thiophene+maleimide+siRNA complexes at the three different temperatures are shown in **Figure 4b** and **4c** respectively.

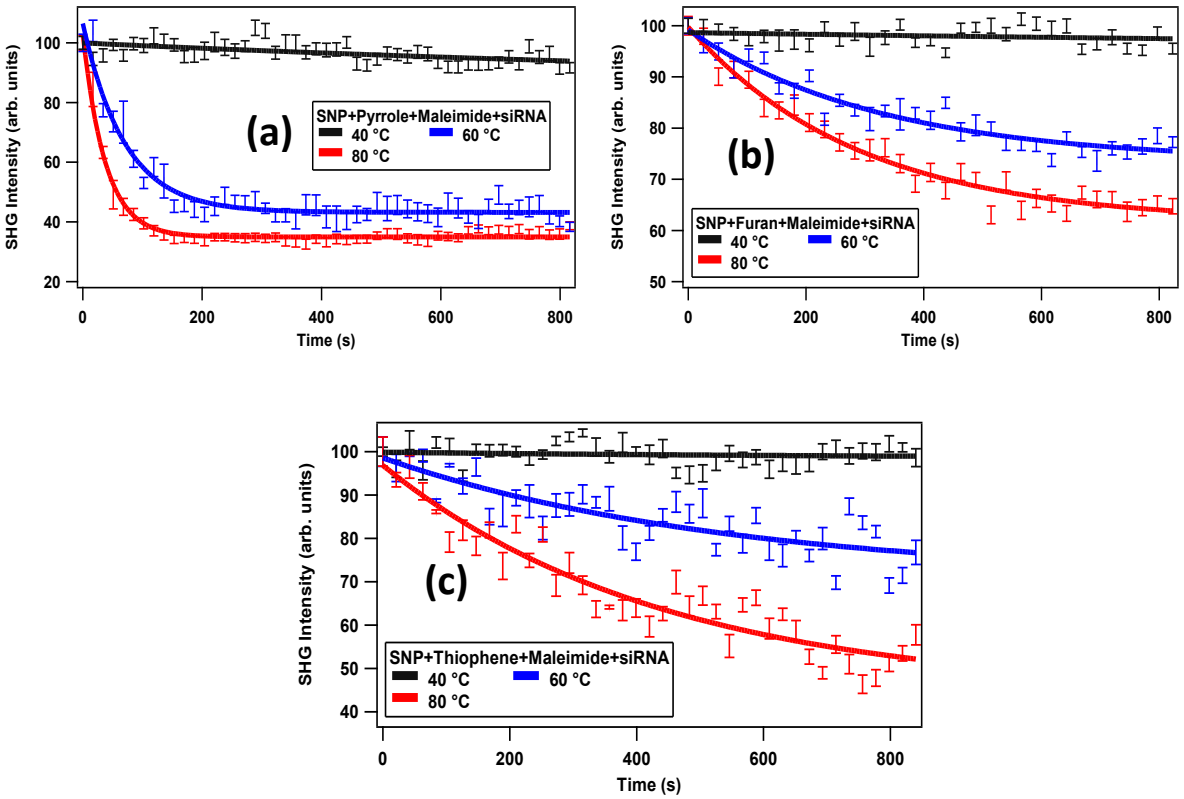

Figure 4. Time-dependent SHG profile of thermal release of siRNA from (a) SNP+pyrrole+maleimide+siRNA, (b) SNP+ furan+maleimide+siRNA and (c) SNP+thiophene+maleimide+siRNA complexes, +/-SEM.

The thermal-cleaving rate of siRNA was shown to be maximum in the pyrrole-based cycloadduct and minimum in the case of the thiophene cycloadduct chemistry. The thermal-cleaving rate constants at different temperatures were obtained by fitting the SHG data using a pseudo-first order exponential rate equation, as described in previous works [31] [49]. The different saturation levels reached at 60 and 80 ˚C for each rDA reaction indicates the likelihood that endo isomers, typically more sterically hindered and hence easier to reform into their corresponding reagents [23], are triggered at lower temperatures while the more stable exo isomers are released

at the higher temperature. The endo isomer is usually thermodynamically favored to form in the Diels-Alder reaction, and is often referred to as Alder's rule [55]. In the reaction between cyclopentadiene and maleic anhydride the product formed is in the endo isomer form at room temperature but forms the exo isomer at high temperatures as the latter has fewer sterically repulsive interactions [56]. The rate constants obtained for the three different complexes at three different temperatures are summarized in **Table 3**.

Table 3. List of fit parameters obtained by fitting SHG data using first order exponential equation, +/- SEM.

Temperature (°C)	Rate Constant ($s^{-1} \times 10^{-2}$)		
	Pyrrole	Furan	Thiophene
40	0.056 ± 0.020	0.037 ± 0.008	0.021 ± 0.013
60	1.426 ± 0.109	0.304 ± 0.055	0.182 ± 0.105
80	2.650 ± 0.119	0.345 ± 0.036	0.227 ± 0.053

Light activated photothermal release

The SNP samples conjugated with the three different DA linkers were irradiated at 405 nm, a wavelength that overlaps with the SNP plasmon resonance (**Figure S1**). Localized heating of the nanoparticle induced cycloreversion of the DA linkers, with varying rates based on the demonstrated kinetics previously illustrated. The normalized release profiles are shown in **Figure 5**. All the samples were normalized to the total oligo on the surface of the nanoparticle, represented by sulfide-reducing a non-irradiated control sample. The patterns show a similar trend in which faster photothermal release is observed with the pyrrole-based sample, while a much slower decay is observed with the thiophene sample. Localized heating in plasmonic nanoparticles can be explained by the metal's ability to absorb far field radiation and produce

enhanced near fields [57]. Plasmonic resonances decay by re-emission of an electron or creation of hot electron-hole pairs by Landau damping [58]. For plasmonic energies greater than the interband transition threshold, hot holes will mainly form at the upper edge of the noble metal d band with the electrons located at the thermal Fermi energy level or higher [59]. Hot electrons will then re-distribute that energy to lower energy electrons via electron-electron scattering until equilibrium is reached and heat is dissipated from the lattice to the surroundings. The choice of silver nanoparticles was based on their utility in biological applications, a result of their non-toxicity to human cells and their anti-microbial and anti-fungal properties [60]. Optically, they exhibit a large absorption cross section [61], suggesting a more efficient light-to-heat conversion response [62]. This localized heat phenomena can be utilized to generate adequate thermal energy and induce the rDA reaction. Bulk solution temperatures were measured and reached a steady state of 48 °C, as shown in **Figure S2**. The trends in **Figure 5** highlight the impactful use these linkers possess to achieve sequential gene delivery with enhanced temporal control utilizing plasmonic metal nanoparticles. For example, by altering exposure time to light stimulation delivery of three different nucleic acid cargo can be potentially achieved as a result of the varying thermal kinetics of the linker conjugation and their respective rDA initiation. Varying doses can be achieved by altering the delivered light energy with a more rapid release applied with the pyrrole DA linker, and a more sustained and prolonged release with the thiophene DA.

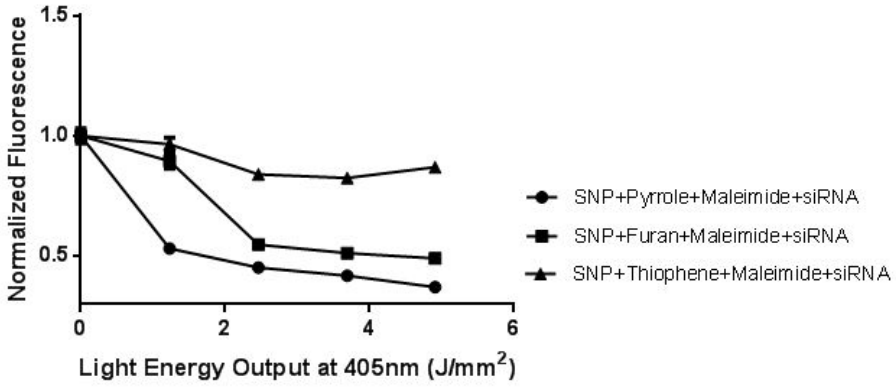

Figure 5. Photothermal release of SNPs conjugated with the 3 different DA linkers, after 405 nm resonant irradiation, measured with fluorescence intensity, +/-SEM.

The residual groups on the silver nanoparticles after the rDA reaction will be the heterocyclic dienes. Furan is listed as a carcinogenic substance by the FDA and Department of Health and Human Services Report on Carcinogens, based on animal tests, and it is considered possibly carcinogenic to humans by the International Agency for Research on Cancer. However, it was recently published by the FDA that intake of furan-contaminated foods averaged 15 µg/day [63] but was still deemed safe for consumption. Our delivery system will contain less than 1µg of the furan, depending on dosages of therapeutic in future studies. Meanwhile, toxicity information on pyrrole-based drugs is scarce, but was recently shown to have acute effects on blood glucose levels with no significant morbidity impacts on the studied rat models [64]. Of the three linkers, thiophene shows the most possible potential for induced toxicity. Biotransformation of heterocyclic rings present in drugs have raised concerns, and of them, thiophene was declared as a structural alert [65] [66]; its metabolism forms reactive metabolites, which are responsible for drug-induced hepatotoxicity. Unsubstituted thiophene has reported LD50 values of 1902 and > 500 mg/kg body weight in mice [67]. At this stage it is difficult to assess accurate toxicology responses of the residual dienes, given their conjugated nature, at the

given dosages. Further studies involving *in vitro* and *in vivo* applications of these DDSs will determine their respective toxicities which will hopefully be showcased in future manuscripts.

Additionally, the presence of the maleimide on the 3' terminal of the siRNA sequence may impact the activity of the siRNA. Previous studies indicate that siRNA retain RNAi activity after 3' modification with several different chemical moieties [68] [69] [70], but at this time, it is not clear what effect, if any, the 3' modification has on the siRNA's ability to interact with the 3' UTR region of mRNA. Further studies are required to address this concern.

Conclusion

The above results demonstrate predictable thermal and photothermal responses for three rDA compositions. The heated pyrrole-based DA cycloadduct had the most rapid release of the siRNA, with entire release occurring within minutes under excitation. Both the furan and thiophene linkers required several minutes to initiate the rDA reaction, with the thiophene in particular showing prolonged stability at high temperature. While furan-based DA cycloaddition is considered the gold standard in the field of drug delivery systems, here we have utilized the additional chemistries of pyrrole-based and thiophene-based bycyclic products with demonstrated breaking responses. Based on the kinetic information gained here from SHG spectroscopy and other analytical methods, the retro-Diels-Alder reaction can be utilized as a powerful tool to temporally release genes, with alternate chemistries generating a range of temperature trigger zones to initiate cleavage. Employing nano-vehicles with localized heat generation abilities, such as plasmonic or magnetic particles, temperatures high enough to release cargo but also limit thermal degradation to surrounding tissue can be achieved for sequential gene delivery. Application of these linkers as effective therapeutic delivery systems will need to be demonstrated in future *in vitro* and *in vivo* studies.

Acknowledgements

This work was supported by the National Science Foundation (CBET-1254281 & NRT-1449785) and the National Institutes of Health (RDE024790A). The authors of this study are grateful to Dr. Debashish Sahu and Ryan Hoff for their assistance with NMR spectroscopy, and the Materials Computation Center at PSU for their recommendations with the computational work. The authors would also like to thank Connie David, James Miller and Dr. Tatiana Laremore for their assistance with mass spectrometry and fluorescence spectroscopy.

References

[1] J. Li, Y. Zhu and D. Oupicky, "Recent Advances in Delivery of Drug-Nucleic Acid Combinations for Cancer Treatment," *J. Controlled Release,* vol. 172, no. 2, pp. 589-600, 2013.

[2] R. Kanasty, J. Dorkin, A. Vegas and D. Anderson, "Delivery Materials for siRNA Therapeutics," *Nat. Mater. ,* vol. 12, no. 11, pp. 967-77, 2013.

[3] H. Lee, A. Lytton-Jean, Y. Chen, K. Love, A. Park, E. Karagiannis, A. Sehgal, W. Querbes, C. Zurenko, M. Jayaraman, C. Peng, K. Charisse, A. Borodovsky, M. Manoharan, J. Donahoe, J. Truelove, M. Nahrendorf, R. Langer and D. Anderson, "Molecularly Self-assembled Nucleic Acid Nanoparticles for Targeted in Vivo SiRNA Delivery," *Nat. Nanotechnol. ,* vol. 7, no. 6, pp. 389-93, 2012.

[4] T. Chu, "Aptamer Mediated siRNA Delivery," *Nucleic Acids Res. ,* p. e73, 2006.

[5] D. Peer, E. Park, Y. Morishita, C. Carman and M. Shimaoka, "Systemic Leukocyte-Directed siRNA Delivery Revealing Cyclin D1 as an Anti-Inflammatory Target," *Science,* vol. 319, no. 5863, pp. 627-30, 2008.

[6] A. Derfus, A. Chen, D. Min, E. Ruoslahti and S. Bhatia, "Targeted Quantum Dot Conjugates for siRNA Delivery," *Bioconjugate Chem.,* vol. 18, no. 5, pp. 1391-396, 2007.

[7] A. Qureshi, A. Doyle, C. Chen, D. Coulon, V. Dasa, F. D. Piero, B. Levi, W. Monroe, J. Gimble and D. Hayes, "Photoactivated miR-148b-nanoparticle conjugates improve closure of critical size mouse calvarial defects," *Acta Biomater.,* vol. 12, pp. 166-73, 2015.

[8] G. Kwon and D. Furgeson, "Biodegradable Polymers for Drug Delivery Systems," *Biomed. Polym. ,* pp. 83-110, 2007.

[9] R. Pandey, A. Zahoor, S. Sharma and G. Khuller, "Nanoparticle Encapsulated Antitubercular Drugs as a Potential Oral Drug Delivery System against Murine Tuberculosis," *Tuberculosis,* vol. 83, no. 6,

pp. 373-78, 2003.

[10] R. Mo, T. Jiang and Z. Gu, "Enhanced Anticancer Efficacy by ATP-Mediated Liposomal Drug Delivery," *Angew. Chem. ,* vol. 126, no. 23, pp. 5925-30, 2014.

[11] M. Lotze and T. Kost, "Viruses as Gene Delivery Vectors: Application to Gene Function, Target Validation, and Assay Development," *Cancer Gene Ther. ,* vol. 9, no. 8, pp. 692-99, 2002.

[12] Y. Lv, L. Hao, W. Hu, Y. Ran, Y. Bai and L. Zhang, "Novel Multifunctional pH-sensitive Nanoparticles Loaded into Microbubbles as Drug Delivery Vehicles for Enhanced Tumor Targeting," *Sci. Rep. ,* vol. 6, no. 1, p. 29321, 2016.

[13] D. Needham and M. Dewhirst, "The Development and Testing of a New Temperature-Sensitive Drug Delivery Sysytem for the Treatment of Solid Tumors," *Adv. Drug Delivery Rev. ,* vol. 53, no. 3, pp. 285-305, 2001.

[14] W. Gao, J. Li, J. Cirillo, R. Borgens and Y. Cho, "Action at a Distance: Functional Drug Delivery Using Electromagnetic-Field-Responsive Polypyrrole Nanowires," *Langmuir,* vol. 30, no. 26, pp. 7778-788, 2014.

[15] M. Gregoritza and F. Brandl, "The Diels-Alder Reaction: A Powerful Tool for the Design of Drug Delivery Systems and Biomaterials," *Eur. J. Pharm. Biopharm.,* vol. 97, pp. 438-53, 2015.

[16] S. Presolski, V. Hong and M. Finn, "Copper-Catalyzed Azide-Alkyne Click Chemistry for Bioconjugation," *Curr. Protoc. Chem. Biol. ,* pp. 153-162, 2011.

[17] M. Dewar and A. Pierini, "Mechanism of the Diels-Alder Reaction. Studies of the Addition of Maleic Anhydride to Furan and Methylfurans," *J. Am. Chem. Soc.,* vol. 106, no. 1, pp. 203-08, 1984.

[18] P. Alston, R. Ottenbrite and T. Cohen, "Secondary Orbital Interactions Determining Regioselectivity in the Diels-Alder Reactions 3. Disubstituted Dienes," *J. Org. Chem.,* vol. 44, no. 21, p. 3739, 1979.

[19] F. Csende, F. Fülöp and G. Stájer, "Chemistry of norbornane/ene and heteronorbornane/ene β-amino acids," *Curr. Org. Synth.,* vol. 5, no. 2, pp. 173-185, 2008.

[20] F. Csende, G. Stájer and F. Fülöp, "Retro Diels-Alder Reactions," *Comp. Org. Synth.: 2nd Ed.,* vol. 5, pp. 518-594, 2014.

[21] S. Yamashita, H. Fukushima, Y. Niidome, T. Mori, Y. Katayama and T. Niidome, "Controlled-Release System Mediated by a Retro Diels-Alder Reaction Induced by the Photothermal Effect of Gold Nanorods," *Langmuir,* vol. 27, no. 23, pp. 14621-26, 2011.

[22] B. Rickborn, "The Retro–Diels–Alder Reaction Part II. Dienophiles with One or More Heteroatom," *Org. React.,* vol. 53, pp. 223-629, 2004.

[23] A. Bakhtiari, D. Hsiao, G. Jin, B. Gates and N. Branda, "An Efficient Method Based on the Photothermal Effect for the Release of Molecules from Metal Nanoparticle Surfaces," *Angew. Chem.,* vol. 121, no. 23, pp. 4230-33, 2009.

[24] B. Fekete, M. Palkó, I. Mándity, M. Haukka and F. Fülöp, "A Domino Ring-Closure Followed by Retro-Diels–Alder Reaction for the Preparation of Pyrimido[2,1-a]isoindole Enantiomers," *Eur. J. Org. Chem.,* vol. 2016, no. 21, pp. 3519-27, 2016.

[25] F. Miklós, Z. Tóth, M. Hänninen, R. Sillanpää, E. Forró and F. Fülöp, "Retro-Diels–Alder Protocol for the Synthesis of Pyrrolo[1,2-a]pyrimidine and Pyrimido[2,1-a]isoindole Enantiomers," *Eur. J. Org. Chem.,* vol. 2013, no. 22, pp. 4887-94, 2013.

[26] I. Nekkaa, M. Palkó, I. M. Mándity and F. Fülöp, "Continuous-flow retro-Diels–Alder reaction: an efficient method for the preparation of pyrimidinone derivatives," *Beilstein J. Org. Chem.,* vol. 2018, no. 14, pp. 318-24, 2018.

[27] R. Woodward and T. Katz, "The Mechanism of the Diels-Alder Reaction," *Tetrahedron Lett. ,* vol. 1, no. 5, pp. 19-21, 1959.

[28] M. Valiev, E. Bylaska, N. Govind, K. Kowalski, T. Straatsma, H. v. Dam, D. Wang, J. Nieplocha, E. Apra, T. Windus and W. d. Jong, "NWChem: a comprehensive and scalable open-source solution for large scale molecular simulations," *Comput. Phys. Commun. ,* vol. 181, no. 9, pp. 1477-89, 2010.

[29] A. Becke, "Density-functional thermochemistry. III. The role of exact exchange," *J. Chem. Phys. ,* vol. 98, no. 7, pp. 5648-5652, 1993.

[30] A. Qureshi, W. Monroe, M. Lopez, M. Janes, V. Dasa, S. Park, A. Amirsadeghi and D. Hayes, "Biocompatible/bioadsorbable Silver Nanocomposite Coatings," *J. Appl. Polym. Sci. ,* vol. 120, no. 5, pp. 3042-53, 2011.

[31] R. Kumal, M. Abu-Laban, C. Landry, B. Kruger, Z. Zhang, D. Hayes and L. Haber, "Plasmon-Enhanced Photocleaving Dynamics in Colloidal MicroRNA-Functionalized Silver Nanoparticles Monitored with Second Harmonic Generation," *Langmuir,* vol. 32, pp. 10394-401, 2016.

[32] V. Guner, K. Khuong, A. Leach, P. Lee, M. Bartberger and K. Houk, "A Standard Set of Pericyclic Reactions of Hydrocarbons for the Benchmarking of Computational Methods: The Performance of Ab Initio, Density Functional, CASSCF, CASPT2, and CBS-QB3 Methods for the Prediction of Activation Barriers, Reaction Energetics," *J. Phys. Chem. A,* vol. 107, no. 51, pp. 11445-59, 2003.

[33] "The PyMOL Molecular Graphics System," *Version 2.0 Schrodinger, LLC..*

[34] A. Qureshi, W. Monroe, V. Dasa, J. Gimble and D. Hayes, "miR-148b Nanoparticle Conjugates for Light Mediated Osteogenesis of Human Adipose Stromal/Stem Cells," *Biomaterials,* vol. 34, no. 31, pp. 7799-810, 2013.

[35] K. Horner and P. Karadakov, "Chemical Bonding and Aromaticity in Furan, Pyrrole, and Thiophene: A Magnetic Shielding Study," *J. Org. Chem.,* vol. 78, no. 16, p. 8037–43, 2013.

[36] K. Kumamoto, I. Fukada and H. Kotsuki, "Diels-Alder reaction of thiophene: dramatic effects of high-pressure/solvent-free conditions," *Angew. Chem.,* vol. 43, no. 15, pp. 2015-17, 2004.

[37] D. Margetic, D. Butler and R. Warrener, "Sulfur-bridged molecular racks: O,S-sesquinorbornadienes, CNS-[3] and CNOS-[4]polynorbornane," *Arch. Org. Chem.,* vol. 2002, no. 6,

pp. 234-56, 2002.

[38] A. Pakiari and Z. Jamshidi, "Nature and Strength of M-S Bonds (M = Au, Ag, and Cu) in Binary Alloy Gold Clusters," *J. Phys. Chem. A,* vol. 114, no. 34, pp. 9212-21, 2010.

[39] D. Nair, M. Podgórski, S. Chatani, T. Gong, W. Xi, C. Fenoli and C. Bowman, "The Thiol-Michael Addition Click Reaction: A Powerful and Widely Used Tool in Materials Chemistry," *Chem. Mater.,* vol. 26, no. 1, pp. 724-44, 2014.

[40] R. Stolz and B. Northrop, "Experimental and theoretical studies of selective thiol-ene and thiol-yne click reactions involving N-substituted maleimides.," *J. Org. Chem. ,* vol. 78, no. 16, pp. 8105-16, 2013.

[41] R. Warrener, D. Margetic and G. Sun, "The N,O-bridged sesquinorbornadienes: a testing ground for establishing the superiority of N-Z pyrrole over furan as a dienofuge in retro-Diels–Alder reactions," *Tetrahedron Lett.,* vol. 42, no. 25, pp. 4263-65, 2001.

[42] R. Hickerson, A. Vlassov, Q. Wang, D. Leake, H. Ilves, E. Gonzalez, C. Contag, B. Johnston and R. Kaspar, "Stability Study of Unmodified siRNA and Relevance to Clinical Use," *Oligonucleotides,* vol. 18, no. 4, pp. 345-54, 2008.

[43] J. Dunklin and D. Roper, "Heat Dissipation of Resonant Absorption in Metal Nanoparticle-Polymer Films Described at Particle Separation Near Resonant Wavelength," *J. Nanomater.,* vol. 2017, no. 3, pp. 1-9, 2017.

[44] K. Eisenthal, "Second Harmonic Spectroscopy of Aqueous Nano-and Microparticle Interfaces," *Chem. Rev.,* vol. 106, no. 4, pp. 1462-77, 2006.

[45] G. Gonella and H.-L. Dai, "Second Harmonic Light Scattering from the Surface of Colloidal Objects: Theory and Applications," *Langmuir,* vol. 30, no. 10, pp. 2588-99, 2013.

[46] J. I. Dadap, J. Shan and T. F. Heinz, "Theory of Optical Second-Harmonic Generation from a Sphere of Centrosymmetric Material: Small-Particle Limit," *J. Opt. Soc. Am. ,* vol. 21, no. 7, pp. 1328-47, 2004.

[47] F. Boman, J. M. Gibbs-Davis, L. M. Heckman, B. R. Stepp, S. T. Nguyen and F. M. Geiger, "DNA at Aqueous/Solid Interfaces: Chirality-Based Detection via Second Harmonic Generation Activity," *J. Am. Chem. Soc.,* vol. 131, no. 2, pp. 844-48, 2008.

[48] S. Walter and F. Geiger, "DNA on Stage: Showcasing Oligonucleotides at Surfaces and Interfaces with Second Harmonic and Vibrational Sum Frequency Generation," *J. Phys. Chem. Lett. ,* vol. 1, no. 1, pp. 9-15, 2009.

[49] R. Kumal, C. Landry, M. Abu-Laban, D. Hayes and L. Haber, "Monitoring the Photocleaving Dynamics of Colloidal MicroRNA-Functionalized Gold Nanoparticles Using Second Harmonic Generation," *Langmuir,* vol. 31, no. 36, pp. 9983-90, 2015.

[50] B. Doughty, Y. Rao, S. Kazer, S. Kwok, N. Turro and K. Eisenthal, "Binding of the Anti-Cancer Drug Daunomycin to DNA Probed by Second Harmonic Generation," *J. Phys. Chem. B,* vol. 117,

no. 49, pp. 15285-89, 2013.

[51] M. S. Gh, M. Wilhelm and H.-L. Dai, "Label-Free Optical Method for Quantifying Molecular Transport across Cellular Membranes in vitro," *J. Phys. Chem. Lett.,* vol. 7, no. 17, pp. 3406-11, 2016.

[52] B. Xu, G. Gonella, B. DeLacy and H.-L. Dai, "Adsorption of Anionic Thiols on Silver Nanoparticles," *J. Phys. Chem. C,* vol. 119, no. 10, pp. 5454-61, 2015.

[53] E. Yan, Y. Liu and K. Eisenthal, "New Method for Determination of Surface Potential of Microscopic Particles by Second Harmonic Generation," *J. Phys. Chem. B,* vol. 102, no. 33, pp. 6331-36, 1998.

[54] P. Hayes, J. Malin, D. Jordan and F. Geiger, "Get Charged Up: Nonlinear Optical Voltammetry for Quantifying the Thermodynamics and Electrostatics of Metal Cations at Aqueous/Oxide Interfaces," *Chem. Phys. Lett.,* vol. 499, no. 4-6, pp. 183-92, 2010.

[55] R. Jarret, J. New, R. Hurley and L. Gillooly, "Looking Beyond the Endo Rule in a Diels-Alder Discovery Lab," *J. Chem. Educ.,* vol. 78, no. 9, p. 1262, 2001.

[56] F. Fringuelli and A. Taticchi, The Diels-Alder Reaction: Selected Practical Methods, Chichester: Wiley, 2002.

[57] A. Manjavacas, J. Liu, V. Kulkarni and P. Nordlander, "Plasmon-Induced Hot Carriers in Metallic Nanoparticles," *ACS Nano,* vol. 8, no. 8, pp. 7630-38, 2014.

[58] X. Li, D. Xiao and Z. Zhang, "Landau Damping of Quantum Plasmons in Metal Nanostructures," *New J. Phys. ,* vol. 15, no. 2, p. 023011, 2013.

[59] M. Brongersma, N. Halas and P. Nordlander, "Plasmon-induced Hot Carrier Science and Technology," *Nat. Nanotechnol.,* vol. 10, no. 1, pp. 25-34, 2015.

[60] B. L. Ouay and F. Stellacci, "Antibacterial Activity of Silver Nanoparticles: A Surface Science Insight," *Nano Today,* vol. 10, no. 3, pp. 339-54, 2015.

[61] Y. Zhang, "Investigation of Gold and Silver Nanoparticles on Absorption Heating and Scattering Imaging," *Plasmonics,* vol. 6, pp. 393-97, 2011.

[62] E. Alarcon, "Silver Nanoparticle Applications: In the Fabrication and Design of Medical and Biosensing Devices," *Springer,* pp. 1-11, 2015.

[63] U. FDA, "Furan in food, thermal treatment; request for data and information," *Fed. Regist.,* vol. 69, pp. 25911-13, 2004.

[64] M. Mohamed, S. Ali, D. Abdelaziz and S. Fathallah, "Synthesis and Evaluation of Novel Pyrroles and Pyrrolopyrimidines as Anti-Hyperglycemic Agents," *BioMed Res. Int.,* vol. 2014, pp. 1-13, 2014.

[65] C. Jaladanki, N. Taxak, R. Varikoti and P. Bharatam, "Toxicity Originating from Thiophene Containing Drugs: Exploring the Mechanism using Quantum Chemical Methods," *Chem. Res.*

Toxicol., vol. 28, no. 12, pp. 2364-76, 2015.

[66] D. Gramec, L. Mašič and M. Dolenc, "Bioactivation Potential of Thiophene-Containing Drugs," *Chem. Res. Toxicol.,* vol. 27, no. 8, pp. 1344-58, 2014.

[67] S.M.Cohen, S.Fukushimal, N. Gooderham, F. Guengerich, S.S.Hecht, I. Rietjens, R.L.Smith, M. Bastaki, C. Harman, M. McGowenh, L.G.Valerio(Jr.) and S.V.Taylor, "Safety evaluation of substituted thiophenes used as flavoring ingredients," *Food Chem. Toxicol.,* vol. 99, pp. 40-59, 2017.

[68] R. Valenzuela, K.Onizuka, A. Ball-Jones, T. Hu, S. Suter and P. Beal, "Guide Strand 3'-End Modifications Regulate siRNA Specificity," *ChemBioChem,* vol. 17, no. 24, pp. 2340-45, 2016.

[69] D. Schwarz, G. Hutvágner, B. Haley and P. Zamore, "Evidence that siRNAs function as guides, not primers, in the Drosophila and human RNAi pathways," *Mol. Cell,* vol. 10, no. 3, pp. 537-48, 2002.

[70] G. Deleavey, J. Watts and M. Damha, "Chemical modification of siRNA," *Curr. Protoc. Nucleic Acid Chem.,* vol. 16, no. 3, 2009.

CHAPTER 3.

Combinatorial Delivery of miRNA-nanoparticle Conjugates in Human Adipose Stem Cells for Amplified Osteogenesis

*Mohammad Abu-Laban[1], Prakash Hamal[2], Asela S. Dikkumbura[2], Raju Kumal[3], Louis H. Haber[2] and Daniel J. Hayes[1, 4 ,5]**

[1] The Department of Biomedical Engineering, The Pennsylvania State University, University Park, Pennsylvania 16802

[2] The Department of Chemistry, Louisiana State University, Baton Rouge, Louisiana 70803

[3] John and Willie Leone Family Department of Energy and Mineral Engineering, Pennsylvania State University, University Park, Pennsylvania 16802

[4] Materials Research Institute, Millennium Science Complex, Pennsylvania State University, University Park, Pennsylvania 16802

[5] The Huck Institute of the Life Sciences, Millennium Science Complex, Pennsylvania State University, University Park, Pennsylvania 16802

*Corresponding author: djh195@psu.edu

Keywords: microRNA, gold, silver, nanoparticles, retro-Diels-Alder, sequential

Abstract

It is becoming more apparent in tissue engineering applications that fine temporal control of multiple therapeutics is desirable to modulate progenitor cell fate and function. Here we describe the independent temporal control of the co-delivery of miR-148b and miR-21 mimic plasmonic nanoparticle conjugates to induce osteogenic differentiation of human adipose stem cells (hASCs), in a *de novo* fashion. By applying a thermally-labile retro-Diels Alder caging and linkage chemistry, these miRNA can be triggered to de-cage serially with discrete control of activation times. The method relies on illumination of the nanoparticles at their resonant wavelengths to generate sufficient local heating and trigger the untethering of the Diels-Alder cycloadduct. Characterization of the photothermal release using fluorophore-tagged miRNA mimics *in vitro* were carried out with fluorescence measurements, second harmonic generation, and confocal imaging. Osteogenesis of hASCs from the sequential co-delivery of miR-21 and miR-148b mimics was assessed using Xylenol Orange and Alizarin Red staining of deposited minerals, and quantitative polymerase chain reaction (qPCR) for gene expression of osteogenic markers. The results demonstrated that sequential miRNA mimic activation resulted in upregulation of osteogenic markers and mineralization relative to miR-148b alone, and co-activation of miR-148b and miR-21 at the same time.

Graphical Abstract

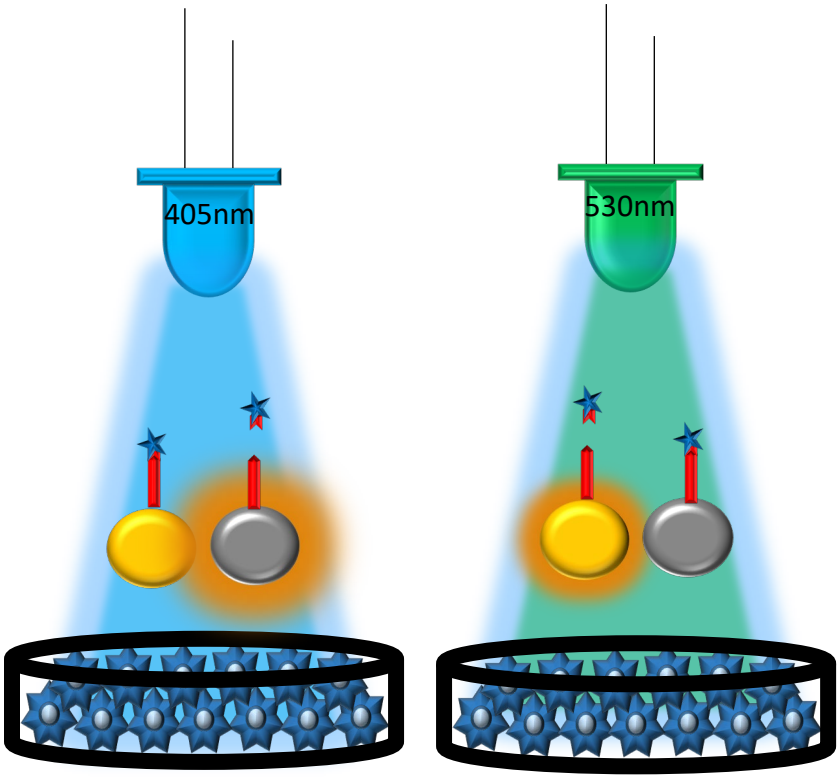

Introduction

Short non-coding RNA molecules participate in post-transcriptional regulation pathways and have gained much attention in regulating gene expressions for a variety of treatments. In particular, microRNAs (miRNA) offer promise in improving repair of tissue damage through well-controlled regenerative processes [1, 2]. These short RNA sequences associate with RNA-induced silencing complexes (RISC) and regulate mRNA localization, polyadenylation and translation [3]. Canonically, they negatively regulate gene expression through degradation or translational inhibition, by binding to the 3' untranslated region (3'UTR) of mRNA transcripts [3, 4]. Modulation of human mesenchymal stem cells (hMSCs), including adipose-derived (hASCs) and bone marrow stem cells (hBMSCs), using miRNAs has widely been studied [5, 6, 7] with a keen focus on blueprinting therapies for bone defects and skeletal reconstruction.

MicroRNA-148b was studied in [8, 9] and identified to upregulate alkaline phosphatase to stimulate osteogenesis activity de novo in hBMSCs and hASCs. Kuei-Chang Li et al. [10] investigated miR-148b in hASCs and reported noggin (NOG), a well-known BMP gene repressor, as a direct gene target. miR-148b initiated downregulation of NOG and promoted osteogenic differentiation through upregulation of BMP expression.

MicroRNA-21 is another widely studied RNA sequence, particularly in examining cell proliferation of cancer cells and stem cells [11, 12]. In [13], miR-21 was found to be overexpressed in non-small cell lung cancer cells, and played a role in repressing PTEN, a tumor suppressor, leading to lung cancer cell growth and invasion. In contrast, overexpression in mouse embryonic stem cells was found to down-regulate the "stem-ness" and pluripotency of cells by directly targeting Sox2 [14].

To circumvent the issue of non-specificity, a host of drug delivery systems have been proposed [15, 16, 17, 18], from liposomal, and viral vectors, to proteins and nano-vehicles. While their mechanisms are many, their purpose is identical: drug dormancy and inactivation prior to reaching their intended target. From the aforementioned drug vehicles, plasmonic nanoparticles have acquired considerable interest. Silver and gold nanoparticles have been investigated for siRNA delivery, specifically for their release kinetics [19, 20] as well as in the delivery of miR-148b [9, 21] to induce osteogenesis in hASCs.

While targeted delivery is an important concept for clinical and translational applications of gene therapy systems, the ability to also co-deliver therapies sequentially and temporally opens the door for a wide variety of effective treatments. The presented study demonstrates the novel concept of delivering two different miRNA mimics, miR-21 and miR-148b, on two separate nanoparticle vehicles, photo-thermally responsive gold (GNPs) and silver nanoparticles (SNPs), in hASCs to demonstrate augmented osteogenesis.

Results & Discussion

Gold & silver nanoparticle photo-thermal release

Prior to investigating the osteogenic inductive ability of co-transfecting miR-21 and miR-148b, the photo-thermal release of the miRNA mimic molecules from the surfaces of SNPs and GNPs was initially characterized. While gold nanoparticles were commercially procured, the HPC-stabilized silver nanoparticles were synthesized in house as previously described and characterized in [22, 23]. The latter yielded particles with an average diameter size of 75.05 ±0.65 nm, while the gold nanoparticles' average diameter size was 78.8 ±2.85 nm. These nanoparticles were used for all experiments while second harmonic generation measurements (SHG) were conducted with a separate batch of each particle. As has been extensively published,

metallic particles at the nano-scale can exhibit plasmonic resonances. Noble metals, in particular, demonstrate this phenomenon within visible light frequencies. These sub-100 nm particles have demonstrated high transfection efficiency in mammalian cells [24], and, in the case of noble metal nanoparticles, the ability to respond to visible light frequencies upon illumination. The latter occurs as a result of a polariton generated between the oscillating conduction band electrons and positively charged lattice [25]. Upon illumination at resonant wavelength of oscillation, these electrons enter an electron-hole pair excited state, which results in electron-electron scattering as well as electron-lattice scattering. The extinction spectra of both nanoparticles used in the present study are reported in **Figure 1A &1B**, along with their TEM images. The plasmon peak was observed at 405-415 nm for SNPs and 551-557 nm for GNPs. As a result of this plasmonic response, generation of localized heating on the nanoparticle surfaces can be achieved in what is referred to as the photothermal effect. This has been explained by the metal's ability to absorb far-field radiation, generating enhanced near fields, with plasmonic resonances decaying by re-emission of electrons and producing hot electron-hole pairs via Landau damping [26, 27]. Heat dissipation into the local surroundings arises from electron-electron scattering between 'hot' electrons and lower energy electrons, as well as electron-phonon interactions that give rise to lattice energy losses [25].

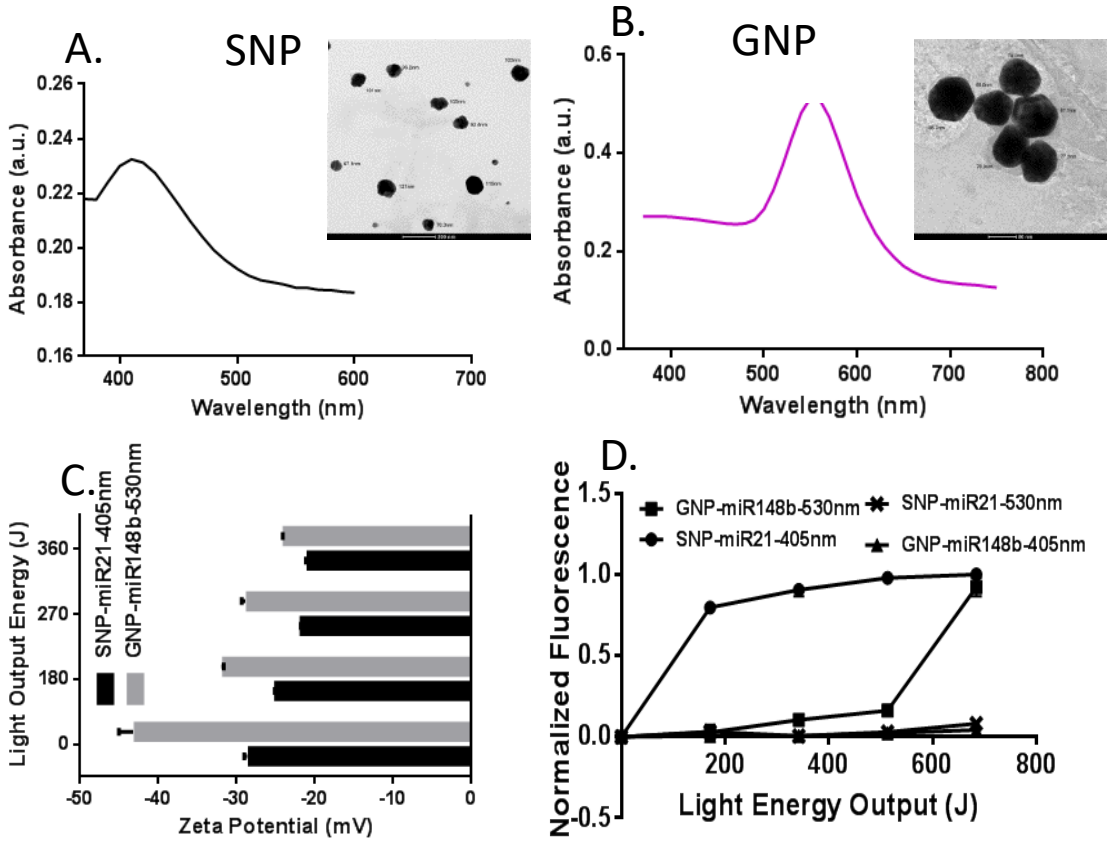

Figure 1. A. TEM image and UV-Vis spectra for silver nanoparticles, and **B**. gold nanoparticles. **C.** Zeta potential measurements of miRNA-NP conjugates for silver and gold surfaces with increasing doses of incident light. **D**. Normalized fluorescence measurements of nanoparticle supernatant solutions, irradiated at 405 and 530 nm light wavelengths. Gold nanoparticle surfaces in this experiment were modified with Diels-Alder linked miRNA mimic-FAM dye molecules, while silver nanoparticles were surface-modified similarly with Cy3-tagged dye molecules.

With any RNA delivery vehicle, a stable conjugation is crucial to protect the structure and function of therapeutics against opsonization and RNase degradation. For effective therapeutic activity, however, a controlled and targeted mechanism for the release of molecules is also significant. Early exposure to acidic environments in endo/lysosomal structures within cells will mute nucleic acid molecules‘ biological effects, requiring a large deliverable dose to mitigate this loss. While there have been several advances made in the design of nanoparticle systems, their release mechanisms are largely assumed or neglected. To design a nanoparticle vehicle with

targeted ability to decage and release miRNA mimics, a thermally-labile linker, responsive to the nanoparticles' photothermal phenomenon was developed that could cleave and release conjugated miRNA mimics at localized temperatures greater than 60 °C [22, 28]. The covalently bound linker was based on Diels-Alder chemistry which relies on the cycloadduct formation between a diene molecule and dienophile. The advantage this linker presents is the ability to slectively release conjugated miRNA upon photo-irradiation of the nanoparticle substrate at their plasmon wavelength, generating adequate localized heat to initiate the retro-Diels-Alder reaction and release the miRNA. This study is the first to our knowledge that demonstrates the proposed delivery vehicle in a biological application.

A type of click chemistry, the Diels Alder cycloaddition takes place between a diene and dienophile possessing overlapping orbital energies (diene's LUMO and dienophile's HOMO), generating sigma bonds from π bonds [4+2] [29, 30, 31]. The result is a stable covalently-bound linker capable of conjugating molecular cargo to surfaces. In the present study, a cycloadduct between a furan group and maleimide was prepared, with additional modifications on the terminal ends. The thiol terminal group on the furan end allows for the facile linkage between the –SH group and Ag & Au surfaces, as has been described [32]. On the maleimide terminal a hexanoic acid group was added which enabled the covalent crosslinking between carboxyl ends and the 5' amine-modified miRNA mimics to yield a robust amide bond. At temperatures 60 ˚C or higher it was demonstrated that the retro-Diels-Alder reaction, i.e. the reversal of the cycloadduct, could be triggered [22, 28]. Using photo-activation, sufficient localized heat was generated to thermally cleave the linker.

Different miRNA-mimics with distinct fluorophores were attached to the SNPs and GNPs using Diels-Alder chemistry, and irradiated to quantify the photo-release. At different LED light

energies at their respective plasmon wavelengths, the zeta potentials of the nanoparticle surfaces were measured and are shown in **Figure 1C**. To further investigate the extent of release at their plasmon wavelengths, fluorescence measurements of the released miRNA in the supernatant were taken, upon irradiation at 530 nm and 405 nm with increasing incident light exposure. These results are presented in **Figure 1D**. In these samples, miR-21 on SNPs were tagged with Cy3 molecules, while miR-148b on GNPs were labelled with FAM. As shown, photo-release was achieved at each particle's plasmonic wavelength, while almost no release was observed upon reversal of the applied light wavelengths. Furthermore, at equal light energy outputs, the SNPs exhibited much more robust de-caging than the GNPs. To investigate further, the absorbance of the Diels-Alder adduct only was measured and is presented in **Figure S1**, in the Supporting Information. From this data, high absorbance was observed at ~400 nm with a discernable local maximum at around 450 nm. This suggests a possibly more complex process involved in the photothermal response of SNPs on the retro-Diels-Alder reaction, with likely a coupled phononic/thermal response and electron-ejection or photon-generating phenomenon triggering the untethering of the cycloadduct. This phenomenon of "hot carriers" has been well described in photocatalytic reactions [33, 34], playing a role in lowering the activation energy barriers in bonds adhered to the surface and has been shown to be distinct from the typical photothermal effect. This relationship between the thermal and non-thermal response was found to be synergistic and co-dependent, increasing super-linearly with increased illumination. Experiments to confirm this are outside the scope of this study, but are recommended for future studies. However, the argument that the cycloadduct can sever in response to direct 405 nm LED light alone seems unlikely, as a result of the observed release profile for the GNP-FAM sample at 405 nm. The non-plasmon resonant state of the GNPs at 405 nm led to little or no photo-

release. Overall, the release trends in Figure 1D suggest more effective release of the miRNA from SNPs than GNPs at shorter light exposures, offering the ability to co-deliver small molecules at separate and distinct intervals.

Second harmonic generation measurement

SHG is a noninvasive, nondestructive, surface-sensitive, nonlinear spectroscopy for characterizing physical and chemical properties at colloidal nanoparticle interfaces [35, 36, 37]. In the SHG process, two incident photons of frequency ω add coherently to generate a third photon with a frequency of 2ω. SHG is dipole forbidden in centrosymmetric media, like bulk solution, but can be generated at the surface of nanoparticles where the symmetry is broken. Recently, SHG has been used as an accurate method to determine molecular adsorption and chemical reactions at nanoparticle surfaces [38, 39], ion-transport processes in liposomes [40, 41, 42], and the release of oligonucleotides from the surface of plasmonic nanoparticles [19, 20, 22, 43].

The release of miRNA from the surface of gold and silver plasmonic nanoparticles was measured in real time using surface-specific SHG spectroscopy. Representative SHG spectra, centered at 400 nm with a full width half-maximum of approximately 4.5 nm, of SNP-miR-21complex are shown in **Figure 2A**. The miRNA-functionalized nanoparticles have higher SHG intensities than the corresponding nanoparticles without miRNA functionalization due to the increased surface charge density through the $\chi^{(3)}$ effect, in agreement with our previous results [19, 20, 22, 43]. Upon irradiation at 400 nm, the SNP absorbed energy at the plasmon resonance, leading to the cleaving of the linker and release of miRNA mimic, resulting in a lower SHG intensity, as shown in **Figure 2A**. Similar results are also obtained for GNP-miR-148b upon irradiation at 530 nm (**Figure S2**). These cleaving dynamics were caused by the photothermal

response of the plasmonic nanoparticles, by hot electrons generated from the plasmon resonance leading to cleavage of the linker, or likely a combination of these two processes [44, 45].

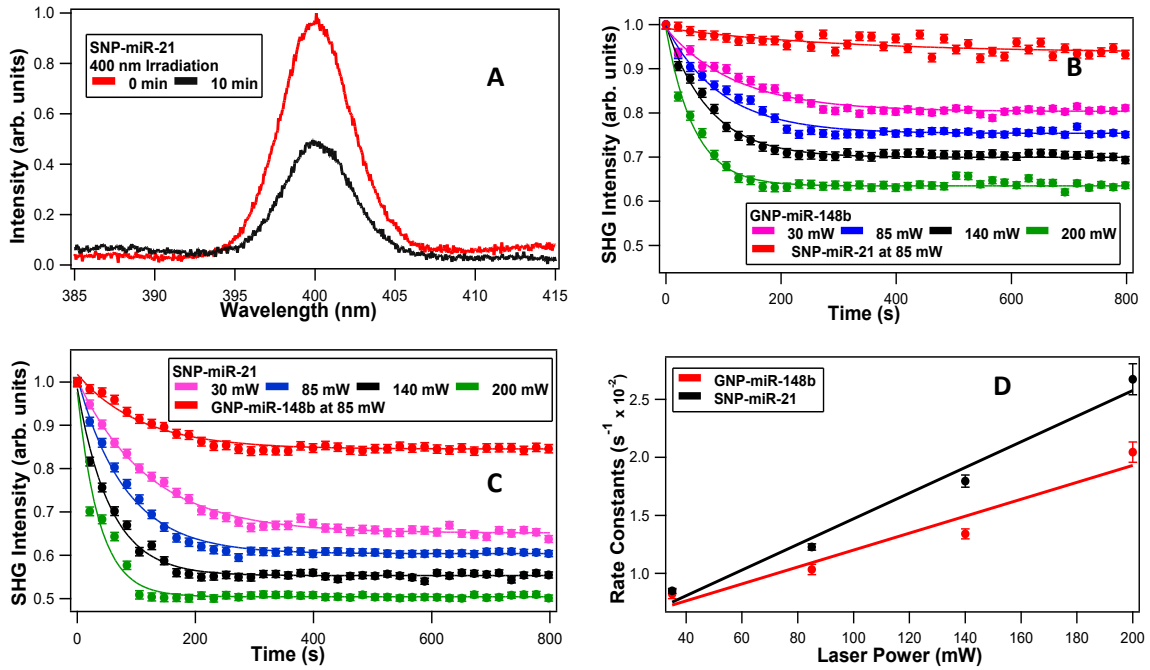

Figure 2. A. Representative SHG spectra of miRNA-functionalized silver nanoparticles at different wavelengths and irradiation times. SHG intensity of the miRNA-functionalized gold and silver nanoparticles as a function of time under varying laser irradiation powers using 530 nm (**B**) and 400 nm (**C**). **D.** The obtained photothermal cleaving rate constants as a function of laser power for miRNA-functionalized gold and silver nanoparticles, using 530 nm and 400 nm irradiation, respectively.

The time-dependent SHG experiments for both sets of nanoparticles were analyzed using power-dependent fits, with higher irradiation powers leading in faster and more complete photothermal cleaving, as shown in **Figure 2B, C**. The experimentally obtained results were fit to a pseudo first-order exponential function given by $E_{SHG} = A + B\, e^{-kt}$, where k is the cleaving rate and A and B are proportionality constants. The values of the fit parameters are summarized in **Tables S1** and **S2**. **Figure 2D** displays the obtained rate constants plotted as a function of laser power for the gold and silver nanoparticles, with corresponding linear fits. The obtained slopes from the fits are (0.007 ± 0.001) s^{-1} mW^{-1} and (0.011 ± 0.001) s^{-1} mW^{-1} for the

gold and silver nanoparticles, respectively. Similarly, the obtained y-intercepts from the fits are $(0.471 \pm 0.166)\ s^{-1}$ and $(0.366 \pm 0.147)\ s^{-1}$ for the gold and silver nanoparticles, respectively. The nonzero y-intercepts are a result of small amount of cleaving caused by the 800 nm laser needed for the SHG measurements. These experimental results indicate that the photothermal release of miRNA mimic at the corresponding plasmon resonances was more efficient for silver nanoparticles, as seen earlier in the fluorescence measurements. This result can be attributed to a higher concentration of hot electron formation in silver nanoparticles leading to higher cleaving efficiencies, although more research is needed to study this process in greater detail. Additionally, control experiments show that the SNP-miR-21complex has only minimal cleaving upon irradiation with 530 nm, as displayed in **Figure 2B**. In contrast, the GNP-miR-148b complex has a greater amount of cleaving upon irradiation at 400 nm, as shown in **Figure 2C**. The gold nanoparticle plasmon peak is centered near 530 nm; however, the gold nanoparticles still have substantial absorption near 400 nm. This absorption at 400 nm can raise the local temperature of the gold nanoparticle surface leading to the photothermal release of miRNA and the corresponding decrease in the SHG intensity that was observed.

In vitro photo-release of GNPs and SNPs

To investigate the photothermal release of the Diels-Alder linked and FAM-tagged oligonucleotides *in vitro* between the two sets of nanoparticles, colocalization between the nanoparticles and fluorescent molecules in the transfected cells were examined using confocal microscopy. For all light irradiation experiments, cells were cultured in Opti-MEM reduced serum media. This was due to the possibility of near-UV wavelengths generating toxic photo-products and radical oxygen amongst amino acid components of DMEM medium [46]. At 405 nm, hASCs transfected with SNP-FAM were illuminated at 50 J of incident light energy, while

those transfected with GNP-FAM were illuminated at 565 J. Due to the observed toxic cellular response to the 405 nm LED light source, the SNPs group was maintained at a much less intense exposure than the GNP samples to mitigate its adverse effects. More importantly, release rates in **Figure 1D** revealed that 550-600 J was needed for substantial thermal cleavage in gold nanoparticle samples. For each nanoparticle system, images were taken of non-illuminated samples, samples irradiated at 405 nm (50 J), and at 530 nm (565 J). These images are presented in **Figures 3** and **4.** The green channel was used to view the FAM conjugated to the nanoparticles, while the blue and red channels were selected to view silver and gold nanoparticles, respectively. The overlay images between the nanoparticles' and FAM channels are also shown as a qualitative assay in determining release of the payload upon photo-activation based on colocalization of the channels. In **Figure 3**, SNP-FAM 405 nm treated cells showed more intense and punctate spots of green that do not colocalize with the blue pixels contributed by the silver nanoparticles' plasmon scattering. The calculated Mander's colocalization coefficients for the non-irradiated silver nanoparticle samples, 530 nm-irradiated, and 405 nm-irradiated samples were calculated to be 0.934, 0.938 and 0.695, respectively. The results indicate only thermal release at the particles' plasmon resonance wavelength, as anticipated.

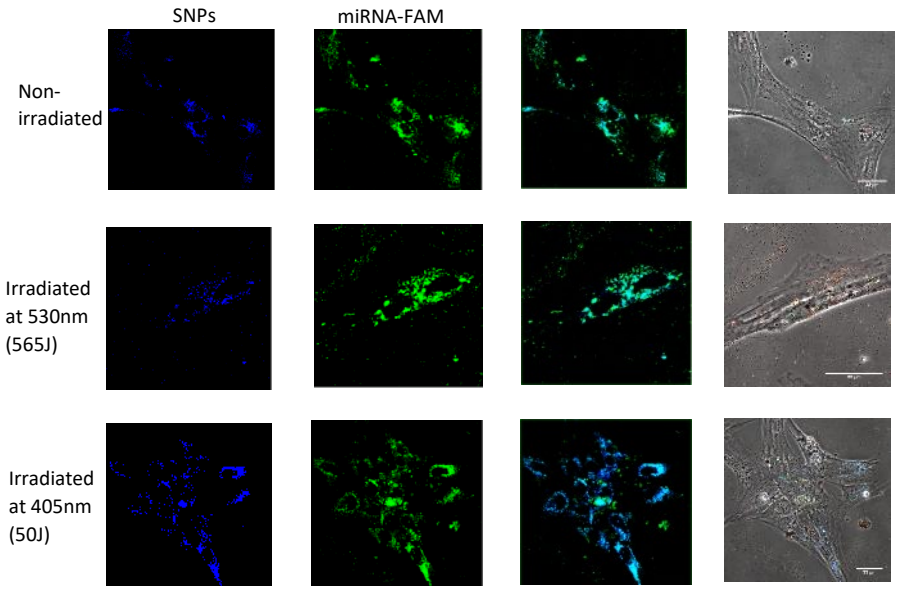

Figure 3. Colocalization of SNPs (blue) & conjugated FAM molecules (green) in hASCs. Irradiation at 400 nm (50 J) and 530 nm (565 nm). 60X magnification used with scale bars annotated at 33 μm.

SNP-treated hASCs were also treated with Texas-Red-tagged transferrin endosomal staining, to investigate the nanoparticle-miRNA conjugates ability to escape from the encapsulations after endocytic uptake [47, 48]. Those images along with the z-stack images are presented in **Figure S5**, in the Supporting Information. FAM was used on the SNPs instead of Cy3 only in this experiment to avoid overlapping between the Cy3 emission and Texas Red labeled transferrin. Low to moderate amounts of colocalization was found between the red-stained endosomes and green SNP-FAM molecules regardless of illuminated state, suggesting clathrin-mediated endosomal encapsulation to be present but limited. The transfection mechanism of metal nanoparticles has been demonstrated to be non-specific [49]. Receptor-mediated uptake as well as phagocytosis, macropinocytosis, adhesion and passive transport, have all been demonstrated to play a role in nanoparticle entry into cells [50]. Whether one mechanism dominates over the others is largely dependent on the particle's size and shape, surface charge, and chemical moiety [48, 49, 51].

In **Figure 4**, images of hASCs treated with GNP-FAM are represented. Once again, upon inspection of the overlay channels between the FAM and GNPs, a greater degree of de-colocalization is observed in the 530 nm-irradiated sample, GNPs' plasmonic resonant wavelength. The calculated Mander's coefficients for the non-irradiated, 405 nm-irradiated, and 530 nm-irradiated samples here were calculated to be 0.935, 0.834, and 0.660, respectively.

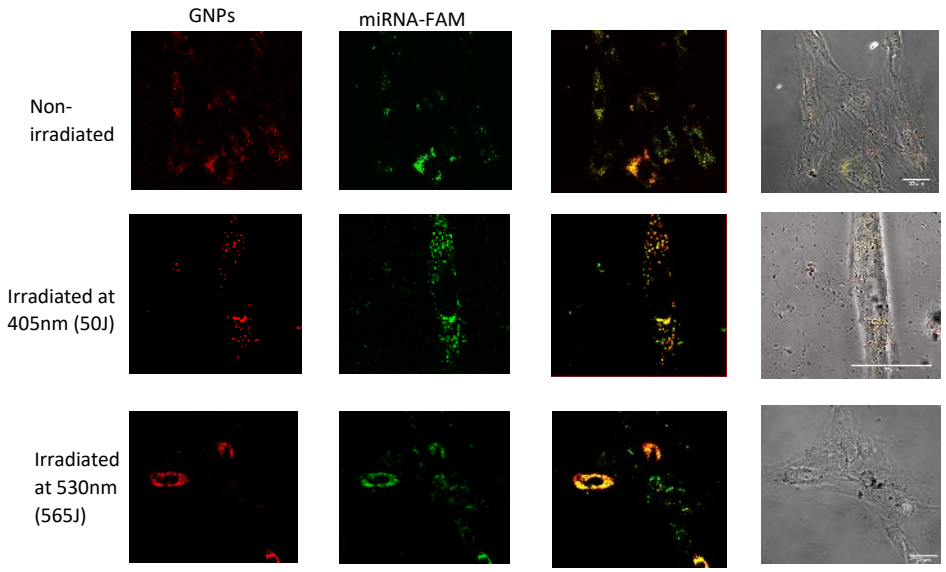

Figure 4. Colocalization of GNPs (red) & conjugated FAM molecules (green) in hASCs. Irradiation at 400 nm (50 J) and 530 nm (565 nm). 60X magnification used with scale bars annotated at 33 µm.

Osteogenic induction

Studies with MSCs suggest miR-21 plays a role in exiting stem cells from their G1-S-G2-M cell cycle and towards non-specific differentiation. Reports of miR-21 mimics promoting osteogenic differentiation in hBMSCs by targeting the SMAD-7 gene a suppressant of the TGF-β family [52], and adipogenesis in hASCs via TGF-β/SMAD 3 signaling modulation [53], have been demonstrated. These results allude to the strong possibility of miR-21 acting to promote differentiation towards the most probable and likely lineage associated with the cell type; adipocytes for hASCs and osteoblasts for hBMSCs. It is, therefore, hypothesized that it is

possible to drive cells down a differentiation pathway with one post-transcriptional regulator, miR-148b, and amplify their differentiation effect with miR-21.

For effective clinical use of miRNA mimic therapies there is a need for targeted and precise delivery of these small molecules for treatment to mitigate off-target effects and non-specific accumulation. There is also the need to protect the vulnerable nucleotide sequences from intra and extra cellular nuclease degradation. In cases of bone defect repair and regeneration, the need for spatial and temporal control was proven necessary as was demonstrated in [54], in which the formation of uncontrolled heterotrophic bone growth from delivered BMPs in other parts of the body became a clinical and health concern.

The miR-21/miR-148b-treated hASC groups listed in **Table 1** were maintained at 37 ˚C incubation for 21 days post-illumination prior to analysis, replenishing the stromal media for all wells every 3 days. To assess mineralization between the different samples, two chemical stain methods were used: Xylenol Orange (XO) and Alizarin Red (ARS). While the latter is more common and replete in literature involving osteogenic assays, its non-specific binding to hydroxyapatite as well as lack of aqueous solubility has led to investigations into alternative assays that can supplement the information provided by ARS, such as XO [55, 56]. XO is a calcium-binding stain, highly water soluble, non-toxic at low concentrations, and fluorescent [55]. Accumulations of calcium deposits such as in mineralized nodules produce intense orange fluorescence upon staining of those nodules. All hASC groups were stained overnight with XO, and imaged after rinsing with DPBS. These results are presented in **Figure 5**. For the SM control group (A), only a diffusive light stain is observed, reflective of the lack of mineralized nodules of these non-differentiated hASCs. In the positive control group (C), in which hASCs were left in OM for 21 days, high mineralization was apparent with intense fluorescence in this sample. In

groups E through I, in which miR-21 and miR-148b were delivered to hASCs using SNPs and GNPs, respectively, small mineralized nodule formations were evident. More intense stain was observed in groups H & I, where the second miRNA (148b or 21) was delivered following a 48 h delay after the initial dose. Sporadic staining was evident in Group B, hASCs treated with GNPs-miR-148b and SNPs-miR-21 but without photo-activation. This suggests some premature and random cleaving of the miRNAs during incubation at 37 °C before their removal from media. Remainder control groups and their images can be found in **Figure S6**, in the supporting information.

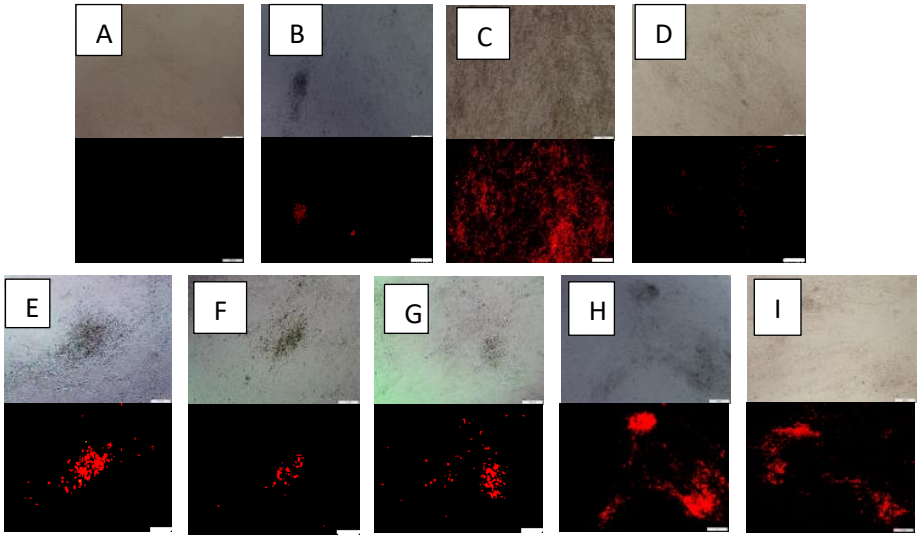

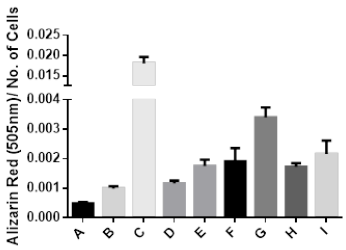

	D	E	F	G	H	I
A	*	*	*	*	*	*
B	X	*	**	*	*	**
D	-	**	X	*	*	**

Figure 5. Xylenol Orange stained samples, imaged 24h after applied staining solution (Top). All images were collected at constant exposure conditions and magnification as indicated by the scale bar set at 200 µm. (Bottom) Quantification of mineralization using Alizarin Red S staining solution and P-value summary between 3 negative controls and experimental groups. Values less than 0.05 are denoted as (*), and (**) for those less than 0.1, and X for no statistical significance. The labels indicate the different

samples as follows: A = Stromal media control; B = miR-21-SNPs & miR-148b-GNPs without activation; C = Osteogenic differentiation media control; D = miR-21-SNPs & miR-148b-GNPs, light activated at 405 nm and 530 nm wavelengths of light, simultaneously, 16 h after transfection; E = miR-21-SNPs & miR-148b-GNPs, light activated at 405 nm 16 h post-transfection, followed by 530 nm at 40 h; F = miR-21-SNPs & miR-148b-GNPs, light activated at 530 nm 16 h post-transfection, followed by 405 nm at 40 h; G = miR-21-SNPs & miR-148b-GNPs, light activated at 405 nm 16 h post-transfection, followed by 530 nm at 64 h; H = miR-21-SNPs & miR-148b-GNPs, light activated at 530 nm 16 h post-transfection, followed by 405 nm at 64 h.

To quantify the extent of mineralization of each sample, ARS was applied to fixed hASCs. All ARS images for all groups can be found in **Figure S7**. In **Figure 5**, the measured absorbances of ARS after de-staining the samples, normalized to the number of hASCs, are shown. Groups with miR-21 & miR-148b co-delivery regardless of sequence of delivery or duration, showed significantly higher ARS than group A, the SM control. Group D which consisted of hASCs treated with GNP-miR-148b only after 530 nm irradiation, yielded higher ARS than the SM group but lower than the groups with both miRNAs delivered. The statistical differences at a 95 % or 90 % confidence level between the groups, specifically the three negative controls, A (SM), B (non-irradiated), and D (miR-148b), and the co-delivered groups are summarized in **Figure 5.** Group C (OM), was statistically significant with respect to all groups with p-values less than 0.001. To determine whether the increased mineralization effect of the combined miRNAs was artifactual or real, osteogenic gene marker expressions were measured and analyzed.

miR-148b has been demonstrated to upregulate ALP activity *de novo* in bone marrow-derived stem cells [8]. To evaluate ALP activity, all experimental groups were measured for ALP gene expression at day 7, summarized in **Figure 6**. Group A (SM) was used to normalize -ΔΔCt values, with 18s used as the housekeeping gene. All treated groups exhibited modest up-regulation of ALP expression with respect to group A and B. While miR-148b alone displayed

lower ALP up-regulation than the other groups except B (non-irradiated), no statistical significance at a 95 % confidence level was found between experimental groups at this stage.

At day 21, gene expression levels of Runx2, BMP-2 and OPN were measured to elucidate the osteogenic pathways of the different treatments. Runx2 is a mid-stage marker and typically a strong indicator of osteogenesis in stem cells [57]. In Figure 7, group C (OM) showed up-regulation at this late time-point with –ΔΔCt mean of 2.25, and similar up-regulation for groups E-I. There was no determined statistical differences at a 95% confidence level between the positive control and experimental groups, however, groups H&I exhibited statistical differences at 90 % confidence level with respect to group D. Group D, with GNP-miR-148b only, displayed only modest up-regulation compared to other groups, with a mean –ΔΔCt value of 0.64.

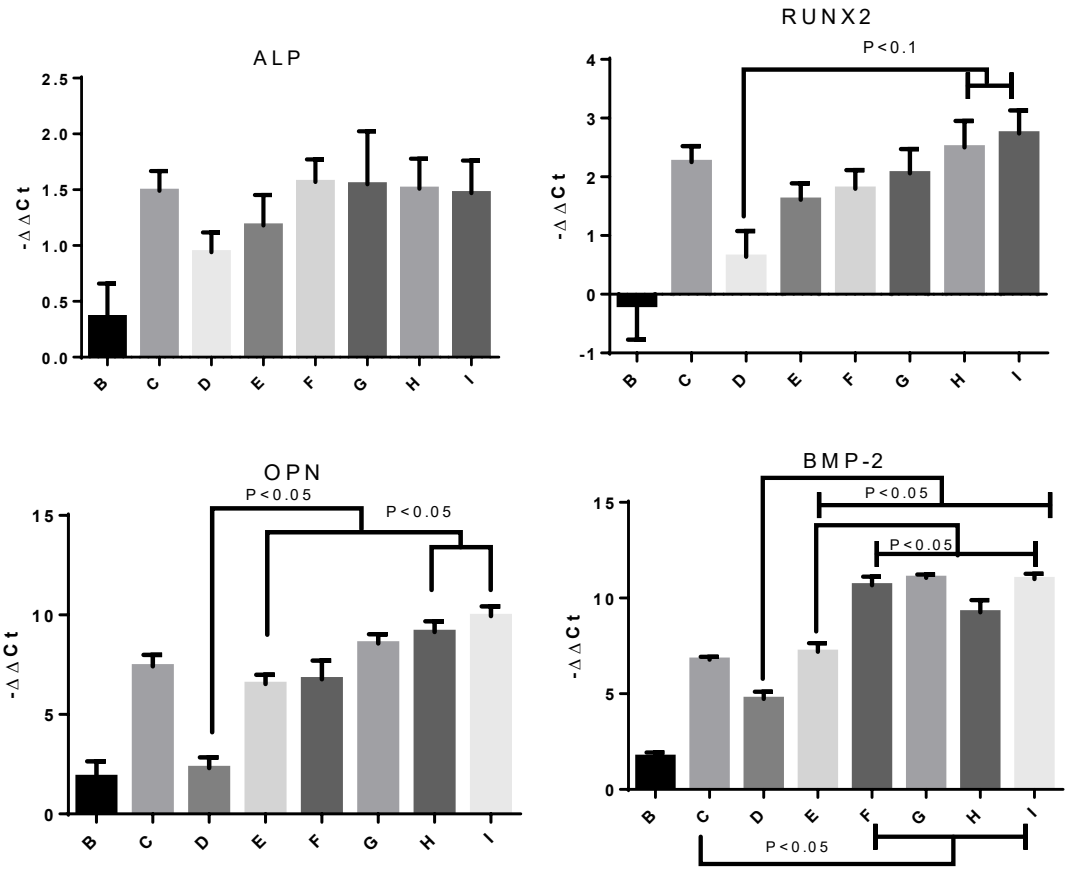

Figure 6. Day 7 & 21 PCR Results. ALP expression was measured at day 7, while Runx2, OPN and BMP-2 were measured at day 21. The legends indicate the different samples as follows: B = miR-21-SNPs & miR-148b-GNPs without activation; C = Osteogenic differentiation media control; D = miR148-GNPs light activated at 530 nm 16 h post-transfection; E = miR-21-SNPs & miR-148b-GNPs, light activated at 405 nm and 530 nm wavelengths of light, simultaneously, 16 h after transfection; F = miR-21-SNPs & miR-148b-GNPs, light activated at 405 nm 16 h post-transfection, followed by 530 nm at 40 h; G = miR-21-SNPs & miR-148b-GNPs, light activated at 530 nm 16 h post-transfection, followed by 405 nm at 40 h; H = miR-21-SNPs & miR-148b-GNPs, light activated at 405 nm 16 h post-transfection, followed by 530 nm at 64h; I = miR-21-SNPs & miR-148b-GNPs, light activated at 530 nm 16 h post-transfection, followed by 405 nm at 64 h.

Osteopontin (OPN), and BMP-2 are mid-to-late stage gene markers, and highly expressed in osteoblast cells [58]. The gene expression results for OPN and BMP-2 displayed the most significant results for the enhanced effect the co-delivery of miR-148b and miR-21 have on osteogenesis (**Figure 7**). At this timepoint, groups E through I (miR-21 & 148b co-delivered) all showed non-statistical differences from group C (OM) for OPN expression, while demonstrating statistical significance from groups D & B (148b only & non-irradiated) and robust up-regulation with $-\Delta\Delta Ct$ values ranging from 6.63 to 9.95 for the co-delivered groups, compared to 2.31 for miR-148b alone. Amongst the co-delivered groups, delivery of the miRNAs over a 48 h period (H & I) produced the most substantial and significantly highest OPN up-regulation. Interestingly, groups F through I, in which delivery of miRNA mimics was performed sequentially over 24 or 48 h after the initial dose, showed statistically higher expressions of BMP-2, with values ranging from 9.26-11.05, than even the positive control group C with a reported value of 6.78. The gene expression results provide compelling evidence for the potent effect of co-delivering miR-21 and miR-148b on inducing an enhanced osteogenic pathway for hASCs.

In examining Sox2 gene expressions at day 7, single release groups of either miR-148b or miR-21 displayed down-regulation of the potency marker, as predicted for cells undergoing differentiation (**Figure S10**). However, for all miR-21 & miR-148b co-delivered samples

(groups E through I), Sox2 is shown to be significantly up-regulated. At day 21, this upregulation was amplified even more so, with –ΔΔCt values reaching as high as 11 (**Figure 7**). Examination of the light-activated only group, presented in **Figure S11**, also demonstrated a modest increase in Sox2 expression. One explanation is the possibility of induced toxicity post-irradiation that might instigate cells to proliferate and regenerate. There have been reports of far-infrared exposure causing up-regulation of Sox2 gene expressions in hBMSCs [59]. The cell count numbers for the different groups are also displayed in **Figure 7** with a notable reduction in cell numbers for some of the groups. These results may indicate the effect of miR-21 in arresting the cell cycle pathway and driving them towards a specific lineage. However, the upregulation of Sox2 in groups E through I may also attest to a premature tumorigenic growth response in these stem cells that may not be captured within the timeframe of this study. In [60], Sox2 expression was positively correlated with cancer stem cells, specifically in osteosarcomas. Despite the lack of extensive proliferation seen from the cell number trends, the occurrence of osteosarcomas will likely need be validated in future *in vivo* trials with extended differentiation profiles.

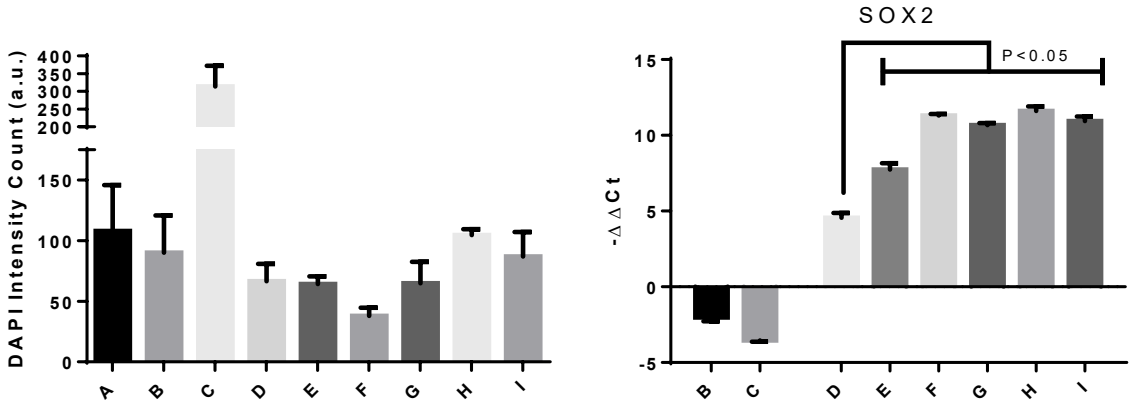

Figure 7. Cell count number, measured by DAPI staining of cells, and Sox2 gene expression at day 21. The legends indicate the different samples as follows: **B** = miR-21-SNPs & miR-148b-GNPs without activation; **C** = Osteogenic differentiation media control; **D** = miR148-GNPs light activated at 530 nm 16

h post-transfection; **E** = miR-21-SNPs & miR-148b-GNPs, light activated at 405 nm and 530 nm wavelengths of light, simultaneously, 16 h after transfection; **F** = miR-21-SNPs & miR-148b-GNPs, light activated at 405 nm 16 h post-transfection, followed by 530 nm at 40 h; **G** = miR-21-SNPs & miR-148b-GNPs, light activated at 530 nm 16 h post-transfection, followed by 405 nm at 40 h; **H** = miR-21-SNPs & miR-148b-GNPs, light activated at 405 nm 16 h post-transfection, followed by 530 nm at 64 h; **I** = miR-21-SNPs & miR-148b-GNPs, light activated at 530 nm 16 h post-transfection, followed by 405 nm at 64 h.

Overall, histochemical staining and PCR results suggest the co-delivery of miR-21 and miR-148b to have an increased effect on the osteogenic differentiation of hASCs. While there exist some discrepancies on the extent of mineralization and gene expressions between simultaneous delivery and sequential delivery at different times and sequences, they were not significant enough to down-regulate or nullify miR-148b's osteogenic ability, at least not within the time points selected for this study. On the contrary, they all demonstrated enhanced faculty in this regard. The implications of this suggest that, under a single dose of miR-21 and miR-148b conjugated to two different nanoparticles, hASC osteogenesis can be upregulated with temporally discrete delivery of the miRNA mimics. Interestingly, sequential delivery of the miRNA versus simultaneous delivery did exhibit greater upregulation of osteogenic markers and mineralization, significantly in some cases. This may be a result of a variety of reasons, including overloading the RISC pathway during simultaneous release, and hence diminishing the efficacy of miRNA targeting, or that the fluctuating expressions of targeted genes and the delivery of miRNA mimics at 64 h coincided with an ideal amount of expression for knockdown or upregulation. To assess and confirm this, sequencing of the entire RNA within these cells would need to be performed.

The presented model provided a working framework in which the delivery of two nucleic acid therapies could be co-delivered at different time points with a single applied dose. Complete staining assays and PCR results for chemically-transfected miR-21 and 148b mimics are

presented in the Supporting Information, in **Figures S8 and S9**. Additionally, the complete set of NP groups, including groups where both sets of NPs are present but illuminated at only a single wavelength, and PCR results used in this study are presented in **Figure S10 and S11**. Cell counts of NP-transfected and chemically transfected hASCs for each group by measuring DAPI intensities are presented in **Figure S12**.

Transfection and uptake efficiency

Transfection efficiencies measured by flow cytometry, and NP uptake efficiency measured by ICP-AES are presented in **Figure S13.** Fluorescence measurements inside the cells indicated SNP transfection at 40 %, while GNP at 20 % within 4h after addition. The low numbers are likely due to quenching effects on the fluorophore from the overlapping nanoparticles‘ optical states during conjugation or degradation from exposure of the 5‘ fluorophore to Rnase enzymes in subcellular compartments.

Using inductively coupled plasma atomic emission spectroscopy (ICP-AES), SNPs uptake efficiency, calculated by normalizing the particle mass inside cells to the total added, was determined to be 70.71 ±2.14 % at 16 h after transfection. Meanwhile, 40 h after transfection that efficiency decreased to 48.57 ±14.29 % while interestingly increasing again to 102.00 ±5.00 % after 64 h. These values suggest a role of the uptake efficiency in improving osteogenesis, where groups in which the second miRNA was released 64 h post-transfection showed the most dramatic results, possibly due to increased intake of nanoparticles at this timepoint. In the closed environment of the 2D cell cultures, the nanoparticles are likely undergoing exocytosis and re-entering cells during the incubation cycle prior to media exchange.

Raman spectroscopy

To determine the compositional nature of the mineralized nodule formed, Raman spectroscopy was used to identify the unique vibrational modes of hydroxyapatite. In **Figure 8**, the peaks attributed to hydroxyapatite include the three minor peaks at 400-490, 570-625, and 1020-1095 cm^{-1}, and a single intense peak at around 960 cm^{-1} [61]. Both OM and miR-21/miR-148b samples displayed similar profiles to the hydroxyapatite sample, particularly at the sole signature peak of 960 cm^{-1}. These results give confidence that the mineralization process was forming hydroxyapatite and not some other calcium salt as a result of non-bone related biomineralization. As a negative control, the SM group was tested and displayed no hydroxyapatite crystal formation.

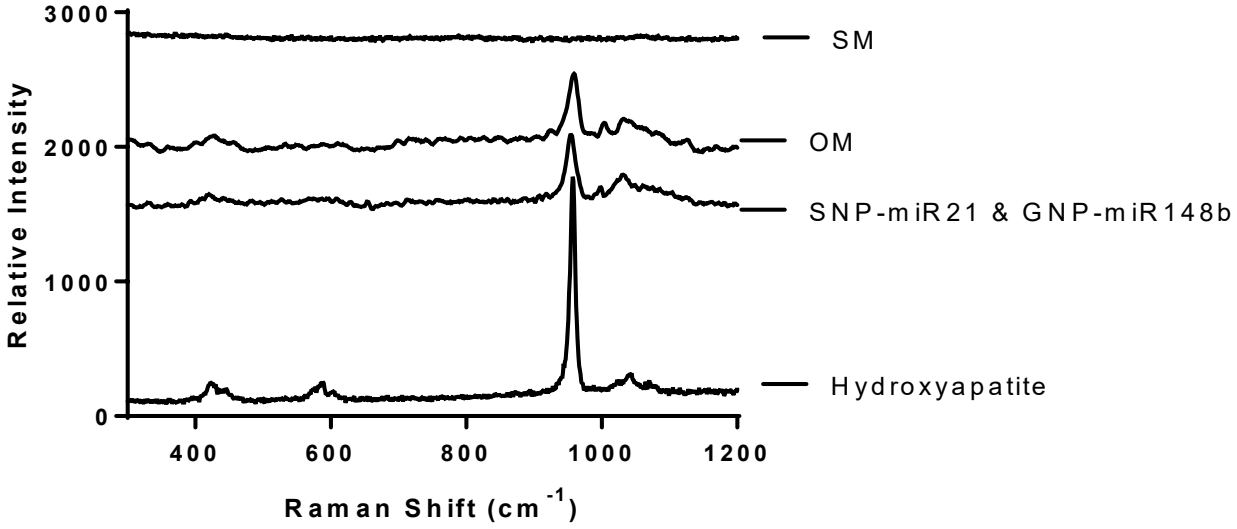

Figure 8. Raman spectroscopy results for Groups A (SM), C (OM) and I (SNP-miR-21 & GNP-148b) with hydroxyapatite powder used as a reference**.**

Materials and Methods

Materials

6-Maleimidohexanoic acid (90 %), 2-furanmethanethiol (98 %), methanol (>99.9 %), isopropanol (>99.9 %), dichloromethane (99.8 %), N-hydroxysuccinimide (NHS) (98 %), silver nitrate (99 %), formaldehyde (36.5 - 38 %), sodium hydroxide (98 %, pellets), hydroxypropyl cellulose (HPC, Mn = 80,000, 99 %), antifoam A (100 %), tris(2-carboxyethyl)phosphine hydrochloride solution (TCEP) (0.5 M), Alizarin-Red Staining Solution (40 mM), Xylenol Orange tetrasodium salt, glacial acetic acid and gold nanoparticles stabilized in 0.1 mM PBS were purchased and used as received from Sigma Aldrich (St. Louis, MO). EDC (1-ethyl-3-(3-dimethylaminopropyl) carbodiimide hydrochloride), Dulbecco's Modified Eagle Medium/Nutrient Mixture F-12 (DMEM F-12), Dulbecco's phosphate-buffered saline (DPBS) without Ca/Mg, Lipofectamine RNAiMAX Transfection Reagent, DEPC-treated water, DAPI (diamidino-2-phenylindole), Transferrin From Human Serum/Texas Red™ Conjugate and Opti-MEM reduced serum medium were purchased from ThermoFisher Scientific (Waltham, MA), fetal bovine serum (FBS) from Lonza, and human adipose stem cells (hASCs) at passage zero were acquired from LaCell (New Orleans, LA). Custom amine-modified oligonucleotides (miR-21: 3' C6-NH2 2'OMe CAA CAC CAG UCG AUG GGC UGU Cy3 5'; miR-148b: 5' C6-NH2 2'OMe UCA GUG CAU CAC AGA ACU UUG U 6-FAM 3') were ordered from Trilink Bio Technologies (San Diego, CA). Mounted 405 nm & 530 nm LED lights from ThorLabs, Inc. (Newton, NJ) were used for photo-activation experiments.

Cell Culture

Commercially acquired hASCs from three different donors were cryopreserved at passage 0, and later thawed for subsequent use for in vitro experiments at passage 2. The cells were passaged in 25 cm^2 flasks (BD Falcon, Franklin Lakes, NJ) in stromal culture medium (SM), which consisted of DMEM F-12, supplemented with 10 % FBS and 1 % antibiotic solution (10,000 μg/mL with penicillin and streptomycin) at 37 ˚C and 5 % CO2 [9]. For the osteogenic positive control (OM), SM was supplemented with dexamethasone (1 nM), ascorbic acid (50 μM) and β-glycerophosphate (20 mM).

Gold and Silver Surface Modification

HPC-silver nanoparticles (SNPs) were synthesized as described in [22, 23], while PBS-stabilized, 80 nm diameter gold nanoparticles (GNPs) were purchased from Sigma-Aldrich. To conjugate both sets of nanoparticles with the miR-21 and miR-148b mimics, the surfaces were first conjugated with thiol- & carboxyl- terminated Diels-Alder cycloadducts as outlined in [22]. In the present study, miR-21 was coupled with silver, while miR-148b was coupled with gold. Briefly, 6-maleimidohexanoic acid (2.11 g) & 2-furanmethanethiol (0.5 g) were mixed in 20 mL methanol and DCM (1:1) for 7 days. The linkers were then mixed with the nanoparticles at approximately 8E9 particles/mL, in 1 mL aliquots for 24 h at room temperature to allow for surface attachment through thiol linkage. For oligonucleotide addition, the nanoparticles were first centrifuged (10,000 g, 10 min) and resuspended in isopropanol thrice, followed by mixing with 100 mM (100 μL) EDC/NHS and the respective 5'amine miRNA mimics (4 μM, 30 μL) for 24 h at room temperature to allow for covalent coupling. Verification of conjugation was tested after centrifugation and resuspension in DEPC water, by displacing the ligands with TCEP treatment (10 μL), and measuring supernatant fluorescence at 525 nm for FAM, and 575 nm for Cy3.

Photothermal release of oligonucleotides

To test and compare the photothermal release rates of silver and gold nanoparticles, light irradiation studies were set up. Equal concentrations (200 ppm) and volumes (100 μL) of each conjugated nanoparticle were dropped separately into a 35 mm Petri dish, after which they were irradiated at either 405 nm or 530 nm wavelength light. The measured power outputs for each LED light source were reported as 570 mW at 405 nm, and 317 mW at 530 nm. The irradiation times were selected to normalize the total energy at each wavelength. 25 μL of each sample was used at each time point, and later collected, diluted, and spun down to measure the supernatant fluorescence for either FAM or Cy3. All measurements were normalized to a non-irradiated control as well as a TCEP-treated sample used to represent the total particle loading. Additionally, zeta potential measurements of the nanoparticles were carried out to monitor the change in surface charge as the negatively charged molecules were cleaved and removed.

Second harmonic generation measurement

Nanoparticles for SHG measurements were prepared as follows: gold and silver nanoparticles were prepared in colloidal aqueous suspension using chemical reduction of chloroauric acid and silver nitrate, respectively [19, 20, 62, 63, 64]. All chemicals were purchased from Alfa Aesar (Haverhill, MA) and used without further purification in ultrapure water. The colloidal gold nanoparticle sample was prepared by a seeded-growth method using hydroquinone and sodium citrate as reducing agents [19, 62, 63]. Briefly, an aqueous solution of 300 μL of 25 mM chloroauric acid in 30 mL of ultrapure water was brought to reflux under vigorous stirring conditions, followed by the addition of 900 μL of 34 mM sodium citrate to synthesize gold seeds. The colloidal gold seed solution underwent a color change from pale yellow to deep red after 15 min and was then removed from heating and cooled to room

temperature. For the seeded-growth synthesis of gold nanoparticles, 200 μL of prepared gold seeds and 100 μL of 25 mM chloroauric acid was added to 10 mL of water, followed by the addition of 30 μL of 34 mM sodium citrate, and 100 μL of 30 mM hydroquinone at room temperature under vigorous stirring conditions for 60 min. For the silver nanoparticle synthesis, an aqueous solution was first made by mixing 250 μL of 59 mM silver nitrate, 1 mL of 34 mM sodium citrate, 30 μL of 98 μM potassium iodide, and 1.25 mL of ultrapure water. This solution was added to 100 μL of 100 mM ascorbic acid solution in 47.5 mL of boiling water and the mixture was refluxed for 60 min under vigorous stirring conditions to prepare the silver nanoparticles [20, 64]. The nanoparticles were further modified with the Diels-Alder linked miRNA mimics as described above.

The experimental setup for the second harmonic generation, which consisted of an ultrafast laser system, an optical setup, and a high-sensitivity spectroscopy detector, has been described previously [19, 20, 43]. A portion of the Titanium:sapphire oscillator laser beam, centered at 800 nm with 75 fs pulses at 80 MHz repetition rate and an average power of 2.6 W, was used to seed the amplifier laser which pumps an optical parametric amplifier (OPA) for tunable-wavelength laser light. The beam from the OPA was used for irradiation studies at 400 nm and 530 nm, corresponding to the plasmon resonances of the silver and gold nanoparticles, respectively. For SHG measurements, the remaining portion of the 800 nm oscillator laser was attenuated to an average power of 790 mW and was focused to a 1 cm quartz cuvette containing the nanoparticle sample. An integrated data acquisition program controlled a magnetic stir bar and a beam block to open and shut every 20 s for collecting the SHG and background spectra in order to measure the background-subtracted SHG signal as a function of time.

In vitro photo-release of SNPs & GNPs

To monitor the in vitro release of the fluorescently-labelled payload, human adipose stem cells (hASCs) were transfected with each of the nanoparticles. For this experiment, the FAM fluorophore was used on both nanoparticle sets. The hASCs were initially seeded at a density of 300,000 cells per dish, on 35mm glass-bottom Petri dishes in SM and incubated at 37 ˚C, 5 % CO2. After 24 h, 100 uL each of the conjugated gold and silver nanoparticles were added separately to the cells for transfection and incubated for an additional 16 h. The groups tested included hASCs with GNPs-FAM non-irradiated, SNPs-FAM non-irradiated, GNPs-FAM irradiated at 530 nm, GNPs-FAM irradiated at 405 nm, SNPs-FAM irradiated at 530 nm, and SNPs-FAM irradiated at 405 nm, for a total of 6 dishes.

All cells treated with SNPs were additionally stained with the endosomal tracking agent transferrin, tagged with Texas Red, as described in [24, 47]. The transfected cells were placed in Opti-MEM medium prior to LED irradiation. Cells were irradiated at the 405 nm LED light (50 J), and at 530 nm (565 J). Post-irradiation, the dishes were incubated at 37 ˚C for an additional 4 h prior to imaging. The dishes were mounted in an Olympus FV10i-LIV confocal microscope at objective 60X phase contrast water immersion/NA1.2. SNPs-FAM samples were viewed at blue (405 nm/420-520 nm) and FITC (495 nm/519 nm) channels, while GNPs-FAM samples were viewed at POPO-3 (533 nm/574 nm) and FITC (495 nm/519 nm) channels.

Osteogenic Induction

To assess the effect of co-delivering miR-21 and miR-148b on the osteogenic induction of hASCs, 2 x 105 cells per well were seeded in 24-well tissue culture plates (BD Falcon, Franklin Lakes, NJ). Prior to treatment, the hASCs were left to incubate in stromal media (SM) at 37 ˚C for 24 h. A total of 13 groups in duplicates were set up to measure different effects of sequence and dosage time, as well as controls. These are summarized in **Table 1**. Only results for groups

A through I are depicted in the main article, while comprehensive results with the remaining 4 control groups can be found in the Supporting Information. Prior to transfection, all groups to be irradiated were placed in Opti-MEM solution. For transfection, 5 μL of SNP-miR-21 (~8E9 particles/mL, 0.123 μM miR-21) and/or 10 μL GNP-miR-148b (~4E9 particles/mL, 0.128 μM miR-148b) suspended in Opti-MEM were added to the respective groups for 16 h prior to photo-release. Where indicated, the treated cells were exposed to 405 nm LED light (50 J), and/or 530 nm LED light (565 J). The cells were maintained in the same Opti-MEM at 37 ˚C in between the different photo-release wavelengths, as well as for an additional 24 h after the final irradiation step, prior to replacing media with SM. Thereafter, the culture media was replaced every 3 days with SM. Evaluation of osteogenesis was conducted at day 7 and day 21 using PCR, and histochemical staining at day 21.

For investigating the effect of the miRNAs alone, additional groups in which the miRNA mimics were chemically transfected using RNAiMAX transfection reagent only, per the manufacturer's protocol, were set up and are presented in the Supporting Information.

Table 1. hASC groups treated with GNP-miR-148b and/or SNP-miR-21, illuminated at different wavelengths.

Group	Description
A	hASCs in stromal medium (SM) only
B	hASCs transfected with SNP-miR-21 & GNP-miR-148b, but non-irradiated
C	hASCs in osteogenic differentiation medium (OM)
D	hASCs transfected with GNP-miR-148b only, and irradiated at 530nm
E	hASCs transfected with SNP-miR-21 & GNP-miR-148b, and irradiated at 405nm and 530nm 16h post-transfection (taken as 0h reference)
F	hASCs transfected with SNP-miR-21 & GNP-miR-148b, and irradiated at 405nm at 0h and 530nm at 24h
G	hASCs transfected with SNP-miR-21 & GNP-miR-148b, and irradiated at 530nm at 0h and 405nm at 24h

H	hASCs transfected with SNP-miR-21 & GNP-miR-148b, and irradiated at 405nm at 0h and 530nm at 48h
I	hASCs transfected with SNP-miR-21 & GNP-miR-148b, and irradiated at 530nm at 0h and 405nm at 48h
LA	*hASCs transfected with non-conjugated SNPs & GNPs, and irradiated at 405nm and 530nm at 0h*
miR-21+405nm	*hASCs transfected with SNP-miR-21 only, and irradiated at 405nm*
miR-21+miR-148b+405nm	*hASCs transfected with SNP-miR-21 & GNP-miR-148b, and irradiated at 405nm only*
miR-21+148b+530nm	*hASCs transfected with SNP-miR-21 & GNP-miR-148b, and irradiated at 530nm only*

Histochemical Staining

To evaluate mineralization of the cultured cells after 21 days, Alizarin Red and Xylenol Orange staining were conducted independently. In the latter case, the wells were rinsed with DPBS and fixed with 4 % paraformaldehyde solution for 15 min at room temperature. They were then rinsed again and stained with 40 mM Alizarin Red staining solution for 20 min [9]. The dye was removed and wells washed with DPBS 5 times prior to imaging on an Olympus light microscope. For quantification, 10 % acetic acid was used for de-staining, as outlined in [65]. Briefly, 200 uL of 10 % acetic acid was added to each well, and incubated at room temperature for 30 min. The well contents were scraped and collected in microcentrifuge tubes, followed by heating at 85 ˚C for 10 min. After leaving on ice for 5 min, the solid components were centrifuged out, the supernatant collected and measured at 505 nm absorbance. All values were normalized to the number of hASCs at day 21, measured by DAPI staining.

For Xylenol Orange staining, a 20 mM stock solution was prepared, and transferred to the live cells in SM at a final concentration of 20 μM. The stained samples were left overnight for 24 h at 37 ˚C, prior to rinsing with DPBS and imaging.

Quantitative real time polymerase chain reaction (qPCR)

To measure gene expressions at day 7 and day 21, RNA was extracted from the hASCs with PureLink RNA Mini Kit (Thermo Fisher), following the manufacturer's protocol. The extracted RNA was converted to cDNA prior to amplification using the Thermo Scientific Verso cDNA Synthesis Kit, and running it on the QuantStudio 3 Real-Time PCR system.

For PCR amplification of the cDNA, the following primer sequences (Integrated DNA Technologies, Coralville, IA) were used to asses osteogenic and pluripotent gene expressions (forward and reverse): ALP, 5'-AATATGCCCTGGAGCTTCAGAA-3' and 5'-CCATCCCATCTCCCAGGAA-3'; RUNX2, 5'-GCAAGGTTCAACGATCTGAGATT-3' and 5'-AGACGGTTATGGTCAAGGTGAAA-3'; OPN, 5'-TTCCAAGTAAGTCCAACGAAAG -3' and 5'-GTGACCAGTTCATCAGATTCAT-3'; BMP-2, 5'-ACTACCAGAAACGAGTGGGAA-3' and 5'-GCATCTGTTCTCGGAAAACCT-3';SOX2, 5'-TACAGCATGTCCTACTCGCAG-3' and 5'-GAGGAAGAGGTAACCACAGGG-3'. All genes were normalized to the 18s rRNA housekeeping gene and -ΔΔCt values were calculated using the ΔΔCt method [66].

Transfection and uptake efficiency

The transfection efficiency by fluorescence measurement was performed using flow cytometry analysis. 4 h after transfection the cells were trypsinized and fixed with 4 % parafolmadehyde, and suspended in 96-well plates for analysis. Cy3-conjugated NPs were used for all measurements. Red fluorescence of the cells was measured using BD SORP LSRFortessa Cytometer (Franklin Lakes, NJ). 50,000 events were counted, with two replicates used for each analyzed group. The percentage of hASCs transfected with either Cy3-GNPs or Cy3-SNPs was

determined using the phycoerythrin (PE) channel to view the fluorophore, while fluorescein isothiocynate (FITC) was used for NP plasmon scattering. The samples were run at a flow rate of 0.5 μL/sec and all analysis were performed using FlowJo software.

To measure the uptake of silver nanoparticles at the proposed illumination timepoints (16 h, 40 h, and 64 h), inductively coupled plasma atomic emission spectroscopy (ICP-AES) (Perkin Elmer Optima 5300 DV Optical Emission Spectrometer, Walthon, MA), was used to measure silver quantities inside the cells. After fixation, the cells were dehydrated overnight at 37 °C, and digested with 37 % HCl solution. 7 % diluted samples were prepared for analysis.

RAMAN Spectroscopy

To empirically corroborate the hydroxyapatite identity of the mineralized nodules produced by hASCs after 21 days, the following groups were prepared for Raman analysis: A, C, and I, as well as commercial hydroxyapatite powder as a reference. The adhered hASCs were detached and loaded onto a glass microscope slide in DPBS suspension prior to analysis. A Horiba LabRam system was used for all measurements, using 488 nm laser and 50X objective. The selected scan range used was 300 to 1200 cm^{-1}.

Statistical Analysis

Results presented are expressed as mean ± SEM, and analyzed with a one-way t-test in which a p-value < 0.05, or 0.1 where indicated, was deemed significant.

Conclusion

A co-delivery system consisting of gold and silver nanoparticles systems was designed with the ability to carry and photothermally release their miRNA payloads at distinct times and wavelengths of light. Mineralization assays demonstrated higher staining with both miR-21 and

miR-148b delivery, with increased gene expressions of Runx2, BMP-2 and OPN. Herein, we demonstrated the potent ability of the retro-Diels Alder chemistry to temporally release genes and drive augmented osteogenesis in a single dose of our developed gene therapy. Systems providing spatiotemporal control have the potential to improve outcomes in surgical reconstruction and regenerative medicine by precise modulation of tissue repair processes. Regulation of gene expression with miRNA mimics is a promising tool for enhancing control of tissue repair processes particularly when combined with endogenous mesenchymal stem cell (MSC) progenitors. Spatiotemporally directing the proliferation and osteogenic differentiation of these progenitors is of particular interest in the design of therapies for segmental bone defects, spinal fusion and craniofacial reconstruction. The capability to target damaged tissues selectively and modulate potency and osteogenic differentiation provides a clinically relevant tool to stimulate osteogenic progenitors and improve segmental defect repair. While the results presented suggest promise, further studies *in vivo* are needed to address differences in diffusion, transfection efficiencies and particle longevity in an active immune system. We hope to investigate this further in future works.

Acknowledgements

This work was supported by the Office of the Assistant Secretary of Defense for Health Affairs through the Peer Reviewed Medical Research Program under Award No. W81XWH-18-1-0115. The opinions, interpretations, conclusions, and recommendations are those of the author and are not necessarily endorsed by the Department of Defense. The authors of this study are grateful to Anoosha Forghani, Lisa Bernsten, and Cong Chen for many insightful discussions about the roles of miR-21 & miR-148b. The authors would also like to thank Maxwell Wetherington for

assisting with Raman Spectroscopy, Trevor Clarke for his help with Transmission Electron Microscopy, and Laura Jean Liermann for her assistance with ICP-AES.

References

[1] C. Sen and S. Ghatak, "miRNA control of tissue repair and regeneration," Am J Pathol, vol. 185, no. 10, pp. 2629-40, 2015.

[2] J. E. Frith, E. R. Porrello and J. J. Cooper-White, "Concise Review: New Frontiers in MicroRNA-Based Tissue Regeneration," Stem Cells Transl Med, vol. 3, no. 8, pp. 969-76, 2014.

[3] C. Catalanotto, C. Cogoni and G. Zardo, "Concise Review: New Frontiers in MicroRNA-Based Tissue Regeneration," Int. J. Mol. Sci., vol. 17, no. 10, p. E1712, 2016.

[4] K. Kapinas and A. M. Delany, "MicroRNA biogenesis and regulation of bone remodeling," Arthritis Res Ther., vol. 13, no. 3, pp. 220-230, 2011.

[5] S. Fang, Y. Deng, P. Gu and X. Fan, "MicroRNAs Regulate Bone Development and Regeneration," Int. J. Mol. Sci., vol. 16, pp. 8227-53, 2015.

[6] Y. Tang, L. Zhang, T. Tu, Y. Li, D. Murray, Q. Tu and J. J. Chen, "MicroRNA-99a is a novel regulator of KDM6B-mediated osteogenic differentiation of BMSCs," J Cell Mol Med., vol. 22, no. 4, pp. 2162-72, 2018.

[7] S. Chen, Y. Zheng, S. Zhang, L. Jia and Y. Zhou, "Promotion Effects of miR-375 on the Osteogenic Differentiation of Human Adipose-Derived Mesenchymal Stem Cells," Stem Cell Rep., vol. 8, pp. 773-86, 2017.

[8] A. Schoolmeesters, T. Eklund, D. Leake, A. Vermeulen, Q. Smith, S. F. Aldred and Y. Fedorov, "Functional Profiling Reveals Critical Role for miRNA in Differentiation of Human Mesenchymal Stem Cells," PLoS One, vol. 4, no. 5, p. e5605, 2009.

[9] A. T. Qureshi, W. T. Monroe, V. Dasa, J. M. Gimble and D. J. Hayes, "miR-148b Nanoparticle conjugates for light mediated osteogenesis of human adipose stromal/stem cells," Biomaterials, vol. 34, pp. 7799-810, 2013.

[10] K.-C. Li, S.-C. Lo, L.-Y. Sung, Y.-H. Liao, Y.-H. Chang and Y.-C. Hu, "Improved calvarial bone repair by hASCs engineered with Cre/loxP-based baculovirus conferring prolonged BMP-2 and MiR-148b co-expression," Tissue Eng. Regen. Med., vol. 11, pp. 3068-77, 2017.

[11] J. Xu, W. Zhang, Q. Lv and Z. D, "Overexpression of miR-21 promotes the proliferation and migration of cervical cancer cells via the inhibition of PTEN," Oncol Rep., vol. 33, no. 6, pp. 3108-16, 2015.

[12] D. Sekar, S. Saravanan, K. Karikalan, K. Thirugnanasambantham, P. Lalitha and V. Islam, "Role of microRNA 21 in mesenchymal stem cell (MSC) differentiation: a powerful biomarker in MSCs derived cells," Curr Pharm Biotechnol., vol. 16, no. 1, pp. 43-8, 2015.

[13] J. Zhang, J. Wang, F. Zhao, Q. Liu, K. Jiang and G. Yang, "MicroRNA-21 (miR-21) represses tumor suppressor PTEN and promotes growth and invasion in non-small cell lung cancer (NSCLC)," Clin Chim Acta., vol. 411, no. 11-12, pp. 846-52, 2010.

[14] S. SK, A. Marisetty, P. Sathyan, M. Kagalwala, Z. Zhao and S. Majumder, "REST-miR-21-SOX2 axis maintains pluripotency in E14Tg2a.4 embryonic stem cells," Stem Cell Res., vol. 15, no. 2, pp. 305-11, 2015.

[15] M. Alavi, N. Karimi and M. Safaei, "Application of Various Types of Liposomes in Drug Delivery Systems," Adv Pharm Bull., vol. 7, no. 1, pp. 3-9, 2017.

[16] D. Lockney, S. Franzen and L. S., "Viruses as nanomaterials for drug delivery," Methods Mol Biol., vol. 726, pp. 207-221, 2011.

[17] B. J. Bruno, G. D. Miller and C. S. Lim, "Basics and recent advances in peptide and protein drug delivery," Ther Deliv., vol. 4, no. 11, pp. 1443-1467, 2013.

[18] J. A. Hubbell and A. Chilkoti, "Nanomaterials for Drug Delivery," Science, vol. 337, no. 6092, pp. 303-305, 2012.

[19] R. R. Kumal, C. R. Landry, M. Abu-Laban, D. J. Hayes and L. H. Haber, "Monitoring the Photocleaving Dynamics of Colloidal MicroRNA-Functionalized Gold Nanoparticles Using Second Harmonic Generation," Langmuir, vol. 31, no. 36, pp. 9983-90, 2015.

[20] R. R. Kumal, M. Abu-Laban, C. R. Landry, B. Kruger, Z. Zhang, D. J. Hayes and L. H. Haber, "Plasmon-enhanced photocleaving dynamics in colloidal microRNA-functionalized silver nanoparticles monitored with second harmonic generation," Langmuir, vol. 32, no. 40, pp. 10394-401, 2016.

[21] A. T. Qureshi, A. Doyle, C. Chen, D. Coulon, V. Dasa, F. Del Piero, B. Levi, W. T. Monroe, J. M. Gimble and D. J. Hayes, "Photoactivated miR-148b–nanoparticle conjugates improve closure of critical size mouse calvarial defects," Acta Biomater., vol. 12, pp. 166-173, 2015.

[22] M. Abu-Laban, R. R. Kumal, J. Casey, J. Becca, D. LaMaster, C. N. Pacheco, D. G. Sykes, L. Jensen, L. H. Haber and D. J. Hayes, "Comparison of thermally actuated retro-diels-alder release groups for nanoparticle based nucleic acid delivery," Journal of colloid and interface science, vol. 526, pp. 312-21, 2018.

[23] A. T. Qureshi, W. T. Monroe, M. J. Lopez, M. E. Janes, V. Dasa, S. Park, A. Amirsadeghi and D. J. Hayes, "Biocompatible/bioabsorbable silver nanocomposite coatings," Journal of applied polymer science, vol. 120, no. 5, pp. 3042-53, 2011.

[24] P. Brown, A. Qureshi, A. Moll, D. Hayes and W. Monroe, "Silver nanoscale antisense drug delivery system for photoactivated gene silencing," ACS Nano., vol. 7, no. 4, pp. 2948-59, 2013.

[25] M. L. Brongersma, N. J. Halas and P. Nordlander, "Plasmon-induced hot carrier science and technology," Nat. Nanotechnol., vol. 10, pp. 25-34, 2015.

[26] A. Manjavacas, J. Liu, V. Kulkarni and P. Nordlander, "Plasmon-induced hot carriers in metallic nanoparticles," ACS Nano, vol. 8, no. 8, pp. 7630-38, 2014.

[27] X. Li, D. Xiao and Z. Zhang, "Landau damping of quantum plasmons in metal nanostructures," New J. Phys., vol. 15, no. 2, p. e023011, 2013.

[28] A. Bakhtiari, D. Hsiao, G. Jin, B. Gates and N. Branda, "An Efficient Method Based on the Photothermal Effect for the Release of Molecules from Metal Nanoparticle Surfaces," Angew. Chem., vol. 48, no. 23, pp. 4166-69, 2009.

[29] M. Dewar and A. Pierini, "Mechanism of the Diels-Alder reaction. Studies of the addition of maleic anhydride to furan and methylfurans," J. Am. Chem. Soc., vol. 106, no. 1, pp. 203-8, 1984.

[30] P. Alston, R. Ottenbrite and T. Cohen, "Secondary orbital interactions determining regioselectivity in the diels-alder reactions 3. Disubstituted dienes," J. Org. Chem., vol. 44, no. 21, p. 3739, 1979.

[31] F. Csende, F. Fülöp and G. Stájer, "Chemistry of norbornane/ene and heteronorbornane/ene β-amino acids," Curr. Org. Synth., vol. 5, no. 2, pp. 173-85, 2008.

[32] A. Pakiari and Z. Jamshidi, "Nature and strength of M-S bonds (M = Au, Ag, and Cu) in binary alloy gold clusters," J. Phys. Chem. A, vol. 114, no. 34, pp. 9212-21, 2010.

[33] L. Zhou, D. Swearer, C. Zhang, H. Robatjazi, H. Zhao, L. Henderson, L. Dong, P. Christopher, E. Carter, P. Nordlander and N. Halas, "Quantifying hot carrier and thermal contributions in plasmonic photocatalysis," Science, vol. 362, pp. 69-72, 2018.

[34] X. Zhang, X. Li, M. Reish, D. Zhang, N. Su, Y. Gutierrez, F. Moreno, W. Yang, H. Everitt and J. Liu, "Plasmon-Enhanced Catalysis: Distinguishing Thermal and Nonthermal Effects," Nano Lett., vol. 18, no. 3, pp. 1714-23, 2018.

[35] K. B. Eisenthal, "Second harmonic spectroscopy of aqueous nano-and microparticle interfaces," Chem. Rev., vol. 106, pp. 1462-77., 2006.

[36] G. Gonella and H.-L. Dai, "Second harmonic light scattering from the surface of colloidal objects: theory and applications," Langmuir, vol. 30, pp. 2588-99, 2013.

[37] L. H. Haber, S. J. Kwok, M. Semeraro and K. B. Eisenthal, "Probing the colloidal gold nanoparticle/aqueous interface with second harmonic generation," Chem. Phys. Lett., vol. 507, pp. 11-14, 2011.

[38] R. A. Khoury, J. C. Ranasinghe, A. S. Dikkumbura, P. Hamal, R. R. Kumal, T. E. Karam, H. T. Smith and L. H. Haber, "Monitoring the Seed-Mediated Growth of Gold Nanoparticles using In-Situ Second Harmonic Generation and Extinction Spectroscopy," J. Phys. Chem. C., vol. 122, no. 42, pp. 24400-406, 2018.

[39] S.-H. Jen, H.-L. Dai and G. Gonella, "The effect of particle size in second harmonic generation from the surface of spherical colloidal particles. II: The nonlinear Rayleigh− Gans− Debye model," J. Phys. Chem. C, vol. 114, pp. 4302-8, 2010.

[40] R. R. Kumal, H. Nguyenhuu, J. E. Winter, R. L. McCarley and L. H. Haber, "Impacts of Salt, Buffer, and Lipid Nature on Molecular Adsorption and Transport in Liposomes As Observed by Second Harmonic Generation," J. Phys. Chem. C, vol. 121, pp. 15851-60, 2017.

[41] A. Srivastava and K. B. Eisenthal, "Kinetics of molecular transport across a liposome bilayer," Chem. Phys. Lett., vol. 292, pp. 345-51, 1998.

[42] Y. Liu, E. C. Yan, X. Zhao and K. B. Eisenthal, "Surface potential of charged liposomes determined by second harmonic generation," Langmuir, vol. 17, pp. 2063-66, 2001.

[43] R. R. Kumal, M. Abu-Laban, P. Hamal, B. Kruger, H. T. Smith, D. J. Hayes and L. H. Haber, "Near-Infrared Photothermal Release of siRNA from the Surface of Colloidal Gold–Silver–Gold Core–

Shell–Shell Nanoparticles Studied with Second-Harmonic Generation," J. Phys. Chem. C, vol. 122, pp. 19699-704, 2018.

[44] A. M. Goodman, N. J. Hogan, S. Gottheim, C. Li, S. E. Clare and N. J. Halas, "Understanding resonant light-triggered DNA release from plasmonic nanoparticles," ACS Nano, vol. 11, pp. 171-9, 2016.

[45] A. Hatef, S. Fortin-Deschênes, E. Boulais, F. Lesage and M. Meunier, "Photothermal response of hollow gold nanoshell to laser irradiation: Continuous wave, short and ultrashort pulse," Int. J. Heat Mass Transfer, vol. 89, pp. 866-71, 2015.

[46] J. D. Stoein and R. J. Wang, "Effect of Near-Ultraviolet and Visible Light on Mammalian Cells in Culture II. Formation of Toxic Photoproducts in Tissue Culture Medium by Blacklight," Proc. Nat. Acad. Sci. , vol. 71, no. 10, pp. 3961-65, 1974.

[47] A. Kapur, S. H. Medina, W. Wang, G. Palui, X. Ji, J. P. Schneider and H. Mattoussi, "Enhanced Uptake of Luminescent Quantum Dots by Live Cells Mediated by a Membrane-Active Peptide," ACS Omega, vol. 3, no. 12, pp. 17164-72, 2018.

[48] S. Zhang, J. Li, G. Lykotrafitis, G. Bao and S. Suresh, "Size-Dependent Endocytosis of Nanoparticles," Adv Mater., vol. 21, pp. 419-424, 2009.

[49] Y. Li and N. Monteiro-Riviere, "Mechanisms of cell uptake, inflammatory potential and protein corona effects with gold nanoparticles," Nanomedicine, vol. 11, no. 24, pp. 3185-203, 2016.

[50] B. Yameen, W. I. Choi, C. Vilos, A. Swami, J. Shi and O. C. Farokhzad, "Insight into nanoparticle cellular uptake and intracellular targeting," J Control Release, vol. 190, pp. 485-99, 2015.

[51] S. Zhang, H. Gao and G. Bao, "Physical Principles of Nanoparticle Cellular Endocytosis," ACS Nano, vol. 9, no. 9, pp. 8655-71, 2017.

[52] Y. Kim, S. Hwang, Y. Bae and J. Jung, "MiR-21 regulates adipogenic differentiation through the modulation of TGF-beta signaling in mesenchymal stem cells derived from human adipose tissue," Stem Cells, vol. 27, no. 12, pp. 3093-102, 2009.

[53] X. Li, L. Guo, Y. Liu, Y. Su, Y. Xie, J. Du, J. Zhou, G. Ding, H. Wang, Y. Bai and Y. Liu, "MicroRNA-21 promotes osteogenesis of bone marrow mesenchymal stem cells via the Smad7-Smad1/5/8-Runx2 pathway," Biochem Biophys Res Commun., vol. 493, no. 2, pp. 928-33, 2017.

[54] J. W. Hustedt and D. J. Blizzard, "The Controversy Surrounding Bone Morphogenetic Proteins in the Spine: A Review of Current Research," Yale J. Biol. Med., vol. 87, pp. 549-61, 2014.

[55] Y.-H. Wang, Y. Liu, P. Maye and D. W. Rowe, "Examination of Mineralized Nodule Formation in Living Osteoblastic Cultures Using Fluorescent Dyes," Biotechnol Prog., vol. 22, no. 6, pp. 1697-701, 2006.

[56] M. Moester, M. Schoeman, I. Oudshoorn, M. van Beusekom, I. Mol, E. Kaijzel, C. Löwik and K. de Rooij, "Validation of a simple and fast method to quantify in vitro mineralization with fluorescent probes used in molecular imaging of bone," Biochem Biophys Res Commun, vol. 443, no. 1, pp. 80-5, 2014.

[57] J. Xu, Z. Li, Y. Hou and W. Fang, "Potential mechanisms underlying the Runx2 induced osteogenesis of bone marrow mesenchymal stem cells," Am J Transl Res, vol. 7, no. 12, pp. 2527-35, 2015.

[58] Q. Chen, P. Shou, L. Zhang, C. Xu, C. Zheng, Y. Han, W. Li, Y. Huang, X. Zhang, C. Shao, A. Roberts, A. Rabson, G. Ren, Y. Zhang, Y. Wang, D. Denhardt and Y. Shi, "An Osteopontin-Integrin Interaction Plays a Critical Role in Directing Adipogenesis and Osteogenesis by Mesenchymal Stem Cells," Stem Cells, vol. 32, no. 2, pp. 327-37, 2014.

[59] Y.-M. Jeong, X. W. Cheng, S. Lee, K. H. Lee, H. Cho, J. H. KAng and W. Kim, "Preconditioning with far-infrared irradiation enhances proliferation, cell survival, and migration of rat bone marrow-derived stem cells via CXCR4-ERK pathways," Sci. Rep., vol. 7, p. 13718, 2017.

[60] G. Maurizi, N. Verma, A. Gadi, A. Mansukhani and C. Basilico, "Sox2 is required for tumor development and cancer cell proliferation in osteosarcoma," Oncogene, vol. 37, pp. 4626-32, 2018.

[61] R. Cuscó, F. Guitián, S. de Aza and L. Artúsa, "Differentiation between hydroxyapatite and β-tricalcium phosphate by means of μ-Raman spectroscopy," J. Eur. Ceram. Soc., vol. 18, no. 9, pp. 1301-5, 1998.

[62] S. D. Perrault and W. C. Chan, "Synthesis and surface modification of highly monodispersed, spherical gold nanoparticles of 50-200nm," J. Am. Chem. Soc., vol. 131, pp. 17042-43, 2009.

[63] K. R. Brown, D. G. Walter and M. J. Natan, "Seeding of colloidal Au nanoparticle solutions. 2. Improved control of particle size and shape.," Chem. Mater., vol. 12, pp. 306-13, 2000.

[64] H. Li, H. Xia, D. Wang and X. Tao, "Simple synthesis of monodisperse, quasi-spherical, citrate-stabilized silver nanocrystals in water.," Langmuir, vol. 29, pp. 5074-79, 2013.

[65] C. Gregory, W. Gunn, A. Peister and D. Prockop, "An Alizarin red-based assay of mineralization by adherent cells in culture: comparison with cetylpyridinium chloride extraction," Anal Biochem, vol. 329, no. 1, pp. 77-84, 2004.

[66] K. Livak and T. Shmittgen, "Analysis of relative gene expression data using real-time quantitative PCR and the 2(-Delta Delta C(T)) Method," Methods, vol. 25, no. 4, pp. 402-8, 2001.

CHAPTER 4.

Spatial Modulation of Osteoblast Differentiation in 3D-cultured Human Adipose Stem Cells

Introduction

Design of tissue regenerative systems that mimic the complex structural and functional aspects of *in vivo* tissues are amongst the most essential fundamentals of tissue engineering. While whole tissues possess complex attributes to emulate and design, an even more challenging engineering design is encountered at the interface of tissues. At these soft-to-hard tissue transitions, such as muscle-tendon interfaces, biomechanical inconsistencies can lead to injury or failure due to high strain exposure [1]. Different approaches to reconstructing tissue types using implanted biomaterials, or new *ex vivo* tissue implants have been proposed [2, 3, 4]. However, the ability to spatially organize osteoblasts and fibroblasts at their respective zones, in the case of ligament/bone interfaces, is crucial in biological platform designs.

In [5, 6], different polymers were utilized as biomaterials at bone-ligament interfaces, using electrospinning of fibers applied layer by layer, with or without minerals to promote spatial organization of cell types. While the polymers possess biodegradability, the reconstructed grafts do not exhibit gradual mechanical and biological responses typical of native tissues and are prone to tear [7, 8]. The hurdles with most injectable scaffolds are many, and include viability with the host, accurate selection of cell types as well as their differentiation ability, differences in mechanical properties, and the lack of vascularization of implants in the defect site which contributes to graft failure and de-stability at the interface [9, 10]. Allogenic and xenogenic grafts are likely to induce a host or immune system response. Autologous cells are seen as a preferred option, with the harvesting of similar cell types to defect sites to generate new tissue

[11, 12]. The challenges with this method are the morbidity risks faced by the patient, and the need to generate a large cell number and maintain the phenotype of the transplanted cells at the defect site. Within this context, mesenchymal stem cells (MSCs) prove to be an attractive alternative.

MSCs are multipotent cell lines, and capable of differentiating into multiple lineages, including cartilage, bone, and ligament [13, 14, 15]. The cultivation of MSCs are less invasive than bone biopsies and result in less donor-site morbidity. Using only short and single stranded miRNA mimics, MSCs have been differentiated into different cell types by post-transcriptional action of these molecules in repressing or promoting different gene expressions [16]. The ability to deliver nucleic acid has garnered much attention, with different vehicles systems designed to provide trigger-release upon application [17, 18]. Effectively translating these therapeutics to the clinic requires new strategies to facilitate spatiotemporal control, which improve the efficiency of delivery *in vivo*, increase tissue specificity and reduce side effects/toxicity.

In the presented study, the technology of plasmonic nanoparticles triggered by visible wavelengths of light are applied, providing stimuli for miRNA release. These particles, when coupled with thermally-responsive linkers to miRNAs, initiate the decaging process by employing local surface heat generated from the surface upon photoactivation; a result of scattering and collisions between conduction electrons [19]. With the ability to trigger different nanoparticles in overlapping volumes of culture, we demonstrate the ability to deliver two miRNA mimics to instigate MSC, specifically human adipose-derived stem cells, differentiation into two tissue types: osteoblast and pre-adipose cells to create a gradient tissue interface. Using miR-148b to promote osteogenesis, as was demonstrated in studies [18, 20], and miR-21 to reduce pluripotency of hASCs [21], spatially controlled delivery and differentiation can be

achieved. This study, is the first to our knowledge, that demonstrates the unique nanotechnology to discretely activate stem cell co-differentiation pathways towards osteogenesis and adipogenesis along spatial lines. The developed technology presents the opportunity to induce co-differentiation of stem cells adjacently to provide a graded tissue structure or interface, biocompatible with host tissues.

Materials & Methods

StemPro™ human adipose-derived stem cells, EDC (1-ethyl-3-(3-dimethylaminopropyl) carbodiimide hydrochloride), Dulbecco's Modified Eagle Medium/Nutrient Mixture F-12 (DMEM F-12), Dulbecco's phosphate-buffered saline (DPBS) without Ca/Mg, DEPC-treated water, DAPI (diamidino-2-phenylindole), Opti-MEM reduced serum medium, and Gibco® Collagen I, Rat Tail were purchased from ThermoFisher Scientific (Waltham, MA). 6-Maleimidohexanoic acid (90%), 2-furanmethanethiol (98%), methanol (>99.9%), isopropanol (>99.9%), dichloromethane (99.8%), N-hydroxysuccinimide (NHS) (98%), tris(2-carboxyethyl)phosphine hydrochloride solution (TCEP) (0.5M), Alizarin-Red Staining Solution (40mM), citrate-stabilized silver nanoparticles (60nm), and gold nanoparticles (60nm) stabilized in 0.1mM PBS were purchased and used as received from Sigma Aldrich (St. Louis, MO). Custom amine-modified oligonucleotides (miR-21: 3' C6-NH2 2'OMe CAA CAC CAG UCG AUG GGC UGU Cy3 5'; miR-148b: 5' C6-NH2 2'OMe UCA GUG CAU CAC AGA ACU UUG U 6-FAM 3') were ordered from Trilink Bio Technologies (San Diego, CA). Mounted 405nm & 530nm LED lights from ThorLabs, Inc. (Newton, NJ) were used for photo-activation experiments.

Collagen hydrogel

Collagen hydrogel substrates were prepared following the manufacturer's protocol. For a working solution of 3 mL, 300 µL of 10x PBS solution was mixed with 50µl sodium hydroxide (1N) and 650 µL DI water. All components were filtered with a sterile, SFCA membrane, 0.2 µm syringe filter prior to use. 2 mL of Gibco Collagen I, Rat Tail solution was added to the mixture and agitated to make 2 mg/mL collagen solution. Onto each Nunclon® 35 mm Petri dish, 1.5 mL of the solution was plated and incubated at 37 °C for at least one hour. Once solidified, the hydrogel was gently washed with DPBS three times prior to cell seeding.

Cell culture

Cryopreserved hASCs at passage 1, were thawed and cultured in stromal media (DMEM F-12, supplemented with 10% FBS and 1% antibiotic solution-10,000 µg/mL with penicillin and streptomycin) at 37 °C and 5% CO_2 until passage 2. The cells were then trypsinized and seeded onto the surfaces of the plated collagen gel at a density of 300,000 cells/dish. The cells were cultured in stromal medium and incubated at 37 °C for at least twenty-four hours.

Nanoparticle modification and transfection

Gold and silver nanoparticles (60 nm, ~10^9 particles/mL) were independently modified with single stranded hsa-miR-148b-3p and hsa-miR-21-3p mimics as described previously [17]. Briefly, thiol-terminal Diels-Alder based cycloadducts were added to the nanoparticles and washed prior to initiating EDC crosslinking between the carboxyl-terminal linker and 5' amine-modified miRNA mimics. The final solution was washed with isopropanol and resuspended in Optim-MEM for cell transfection. 50 µL of each of the final miRNA/NP solutions (0.286 µM, 20 ppm) were added to the seeded hASCs, and incubated at 37 °C for 24h prior to photoactivation.

Photo-activation

All groups were photo-activated at 405nm and 530nm wavelengths of light using continuous wave mounted LED sources. To control for spatial irradiation at the center and surrounding region, a defined center region of 15mm in diameter was blocked at one wavelength and focused on at another wavelength, and similarly done for the outer regions of the Petri dish sample (**Figure 1**). At 405nm, 45mW of incident power was measured and photoactivation at this wavelength was carried out for 10min. At 530nm, 20mW of incident power was measured at this wavelength for a duration of 30min. All analyses were carried out 21 days after photo-activation.

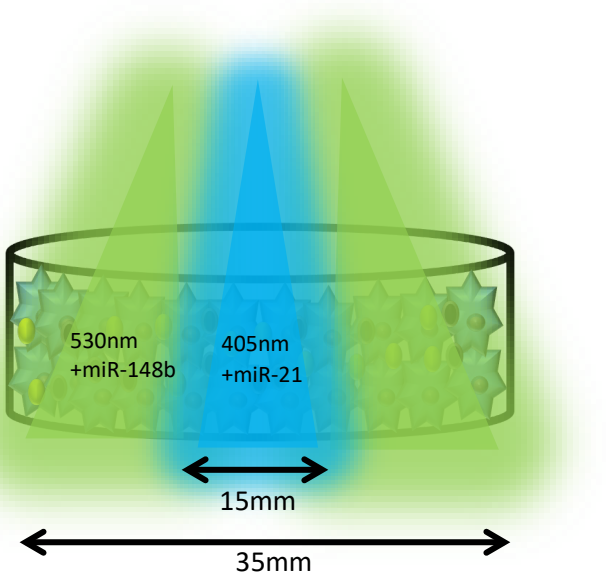

Figure 1. Schematic illustrating experimental setup of spatially-controlled illumination experiments, with one region of hASCs/collagen scaffold exposed to 405nm, and another at 530nm.

Immunostaining

Monoclonal antibody staining was used for detection of OCN and Runx2 proteins, with secondary antibodies each tagged with Alexa 488 and Alexa 555, respectively. The different spatially irradiated regions of each sample were imaged and observed for differences of expression. After fixation in 4% paraformaldehyde for 15 min, the samples were blocked with

3% BSA solution for an hour, and stained with the appropriate primary antibody in 1% BSA solution overnight at 4°C. The secondary antibody was added the following day for 1 h with DAPI staining solution. Imaging of the stained proteins was carried out on an Olympus FV10i-LIV Confocal Microscope. OCN was viewed under the green Alexa 488 channel (499nm/520nm), while Runx2 was observed under the Cy3 channel (547nm/567nm). DAPI staining of the nuclei was observed with the listed DAPI channel (359nm/461nm).

Mineralization Assay

For detection of hydroxyapatite minerals between the osteogenic and non-osteogenic regions of the differentiated hASCs, Alizarin Red and OsteoImage™ stainings were applied. For the latter case, the manufacturer's protocol was followed and confocal microscopy was used to image the formed and fluorescent mineralized nodules. Briefly, after fixation in 4% paraformaldehyde 1 mL of 40mM ARS or 1:100 OsteoImage™ staining reagent was applied to the collagen/hASCs samples for 30min and washed with PBS prior to imaging. In the case of ARS, a more aggressive washing procedure was necessary to remove background stainings of the collagen. After submerging the hydrogel in PBS solution for several hours, with periodic changes in solution, the minerals were destained for quantification as outlined in [22]. The absorbance of ARS was normalized to the number of hASCs, which was quantified using picogreen assay after overnight proteinase K digestion at 56°C.

Lipid Quantification

Lipid formation was measured using Oil Red O staining. 0.3% Oil Red O solution was prepared in 60% isopropanol solution and added to the collagen samples for 5min. The samples were washed in 60% IPA three times prior to imaging. For de-staining, 100% IPA was added as

outlined in [23], and the absorbance of Oil Red O measured at 510nm was normalized to the number of hASCs.

Gene Expression

To measure gene expressions at day 21, RNA was extracted from the hASCs with PureLink RNA Mini Kit (Thermo Fisher), following the manufacturer's protocol. The extracted RNA was converted to cDNA prior to amplification using the Thermo Scientific Verso cDNA Synthesis Kit, and running it on the QuantStudio 3 Real-Time PCR system. For PCR amplification of the cDNA, the following primer sequences (Integrated DNA Technologies, Coralville, IA) were used to asses osteogenic, ligamentogenic, adipogenic and pluripotent gene expressions (forward and reverse): RUNX2, 5'-GCAAGGTTCAACGATCTGAGATT-3' and 5'-AGACGGTTATGGTCAAGGTGAAA-3'; BMP-2, 5'-ACTACCAGAAACGAGTGGGAA-3' and 5'-GCATCTGTTCTCGGAAAACCT-3';SOX2, 5'-TACAGCATGTCCTACTCGCAG-3' and 5'-GAGGAAGAGGTAACCACAGGG-3'OPN, 5'-TTCCAAGTAAGTCCAACGAAAG -3' and 5'-GTGACCAGTTCATCAGATTCAT-3'; COL1A1, 5'-CGTGGTGACAAGGGTGAGAC-3' and 5'-TAGGTGATGTTCTGGGAGGC-3'; Tenasin C, 5'-TCCGAGTGTTCGGTGGATCT-3' and 5'-TTGATGCGATGTGTGAAGACA-3'; Scelarix, 5'-AGAAAGTTGAGCAAGGACC-3' and 5'-CTGTCTGTACGTCCGTCT-3'; Tenomodulin, 5'-TTGAAGACCCAGGAAGTAGA-3' and 5'-ATGACATGGAGCACACTTTC-3'; PLIN1, 5'-CTTTAACCAAACTTGTGGCC-3 ′ and 5′-TACTCAGAAAGTGACACTAG-3. All genes were normalized to the 18s rRNA housekeeping gene and -ΔΔCt values were calculated using the ΔΔCt method [24].

Results & Discussion

Immunostaining

Fluorescent staining of intracellular Runx2 and OCN protein expressions are presented in **Figure 2**. The presented groups include hASCs only without nanoparticle transfection, and two regions of the collagen/hASC sample: the miR-21 targeted center region, and the miR-148b targeted outer band. Runx2 expressions showed higher fluorescence in samples targeted with the osteoinductive miR-148b, while the center region exhibited similar expression levels to the hASC-only control. For OCN expression, higher protein fluorescence was measured in the miR-148b outer bands, with a lower expression present in the center region. The results suggest either a minor osteogenic differentiation pathway with miR-21, or likely the diffusion of osteogenic paracrine factors like OCN from the outer band hASCs throughout the culture dish.

Runx2 is considered a master protein for osteogenesis, as it plays a critical role in promoting the transcriptional activation of other osteogenic genes in the nuclei of progenitor cells [25, 26]. Its expression is often high in pre-osteoblast stages, with a reduced profile during maturation. In osteocytes, Runx2 expression is undetectable. The other promoted osteogenic genes include osteocalcin (OCN), osteopontin (OPN), alkaline phosphatase (ALP), and others. OCN protein is found at high expression levels in mature osteoblasts and plays a critical role in inducing mineralization via hydroxyapatite deposition into the extracellular matrix [27].

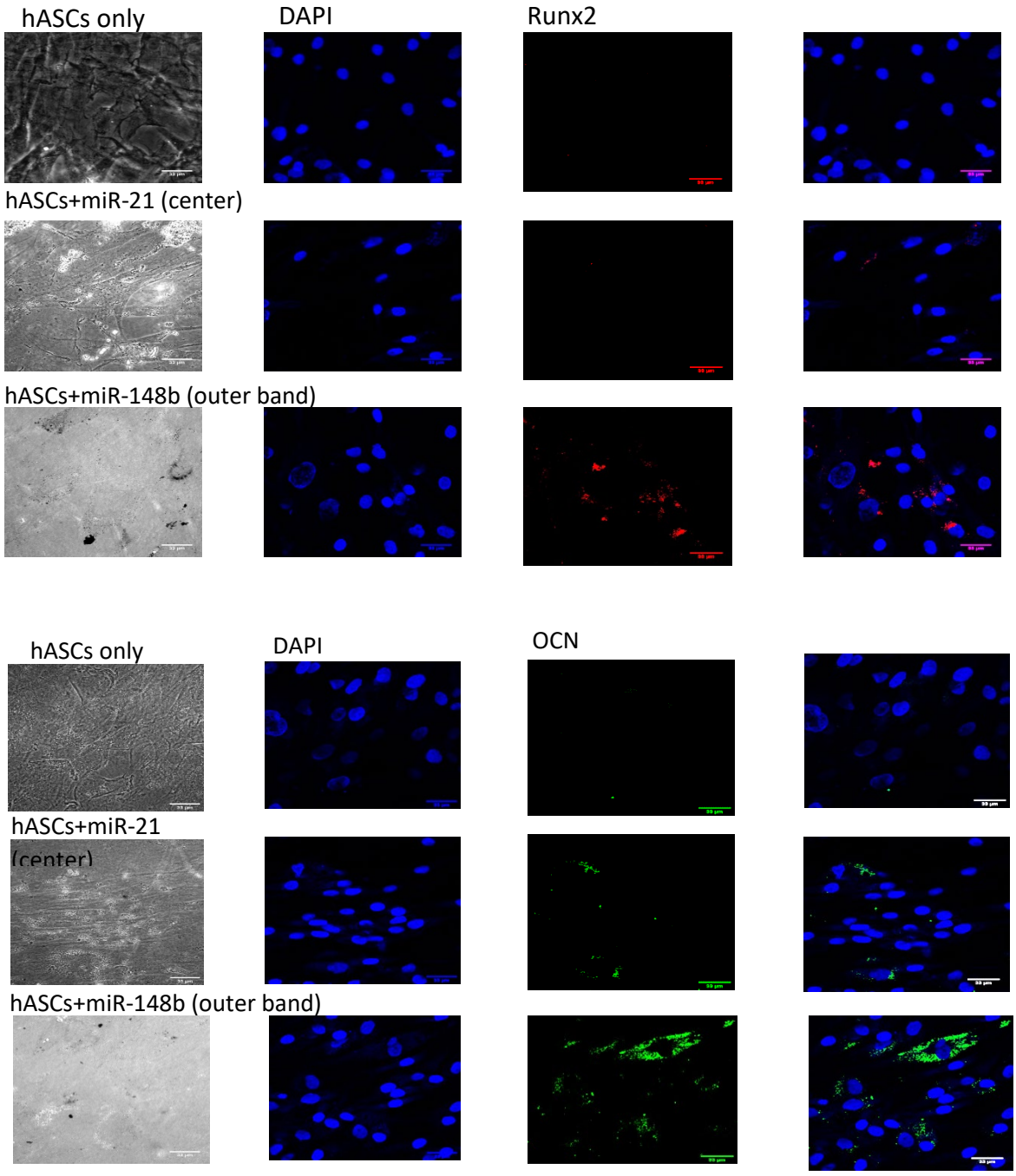

Figure 2. Immunostaining results for Runx2 (above) and OCN expression (below) in hASCs, treated with miR-21 and miR-148b after nanoparticle photoactivation.

Mineralization

To probe for mineralization from the osteogenic-lineated hASCs, OsteoImage^{TM} staining reagent was used for specific hydroxyapatite binding. The reagent can be viewed in the FITC

channel for fluorescence. Different areas of the 405 nm-illuminated center region of the sample are shown in **Figure 3A**, with areas imaged in the 530 nm-illuminated area are presented in **Figure 3B**. The results show considerably higher fluorescence frequency and intensity in the osteogenic-induced areas of the hASCs sample, suggesting successful mineralization.

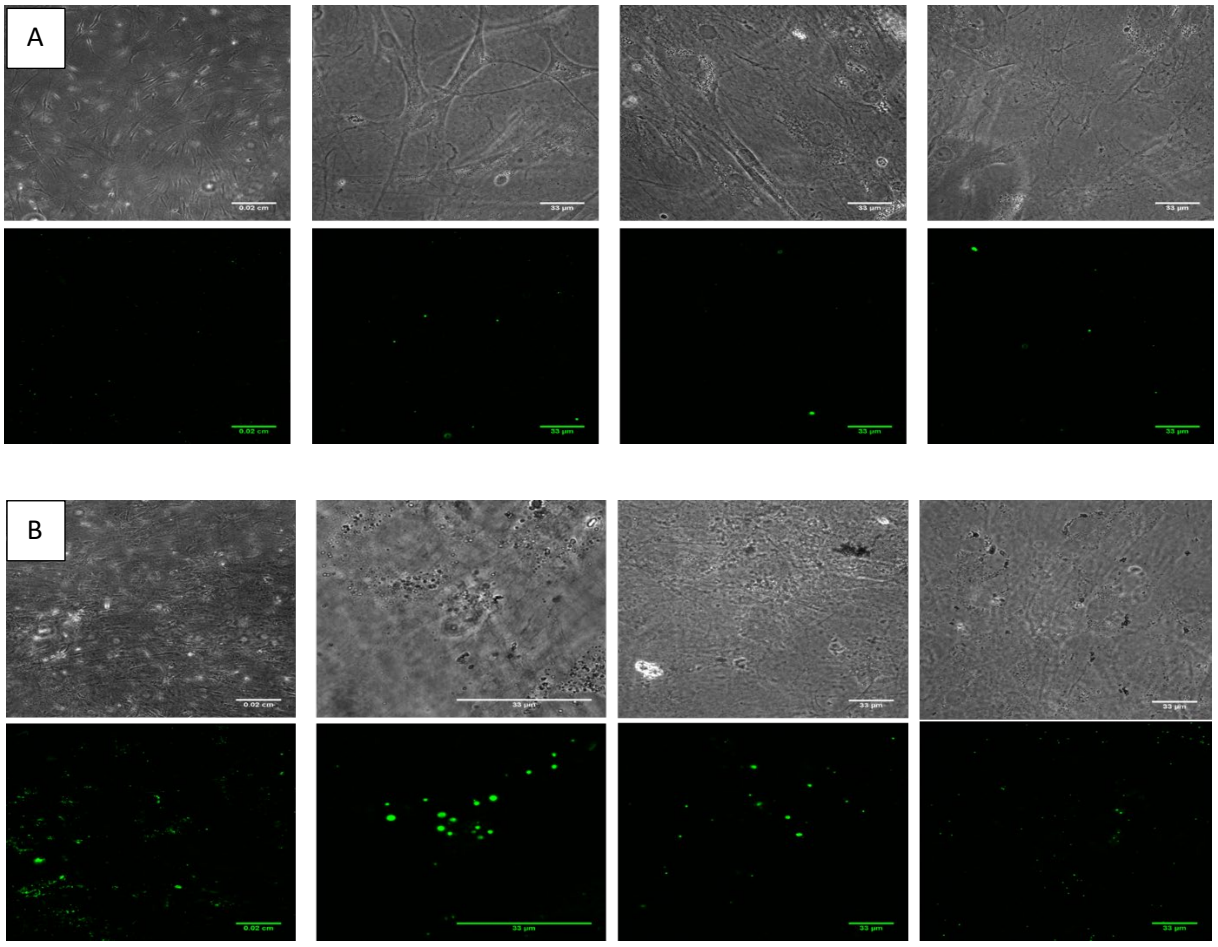

Figure 3. OsteoImage™ staining. **A**. Center region: 405nm-illuminated, miR-21 released. **B**. Outer-band: 530nm-illuminated, miR-148b released.

Alizarin Red staining is a standard histochemical assay for mineralization in osteoblasts, and is a strong calcium-chelating agent. Mineralized nodules can be observed as red specimens with only bright field microscopic imaging. For a more holistic and graded view of the different stimulated regions, serial imaging from the center to the outer-bands of the dish was carried out,

with the images shown in **Figure 4**. Panels A through C display the center region, moving outward. In panel C, small red minerals can be seen in the upper right corner. Moving further outward, the small minerals become more frequent in panel D, and are seen to get larger in panels E and F. The presented data displays the most compelling data thus far of achieved graded differentiation of spatially photo-activated 3D cultured cells. To quantify this effect, the center region was cut out at 15mm, and both the center region and outer band were de-stained with acetic acid. To account for the differences in surface growth area, and hence cell number, between the center and outer band cells, the absorbance measurements were normalized to the number of hASCs in each cut out area, using picogreen assay. The quantification results in **Figure 4** show a statistically significant, seven-fold increase in ARS expression with the miR-148b activated outer band areas of the sample compared to the center region.

Mineralization in osteoblasts occurs with the activation of ALP proteins which play a role in recruiting inorganic phosphate from extracellular fluid and combining it with calcium to produce hydroxyapatite crystals [28]. Frequency and size of these crystals are largely regulated by the osteogenic proteins OCN, OPN, Osterix , and other proteins playing a role in nucleating and growing the crystals.

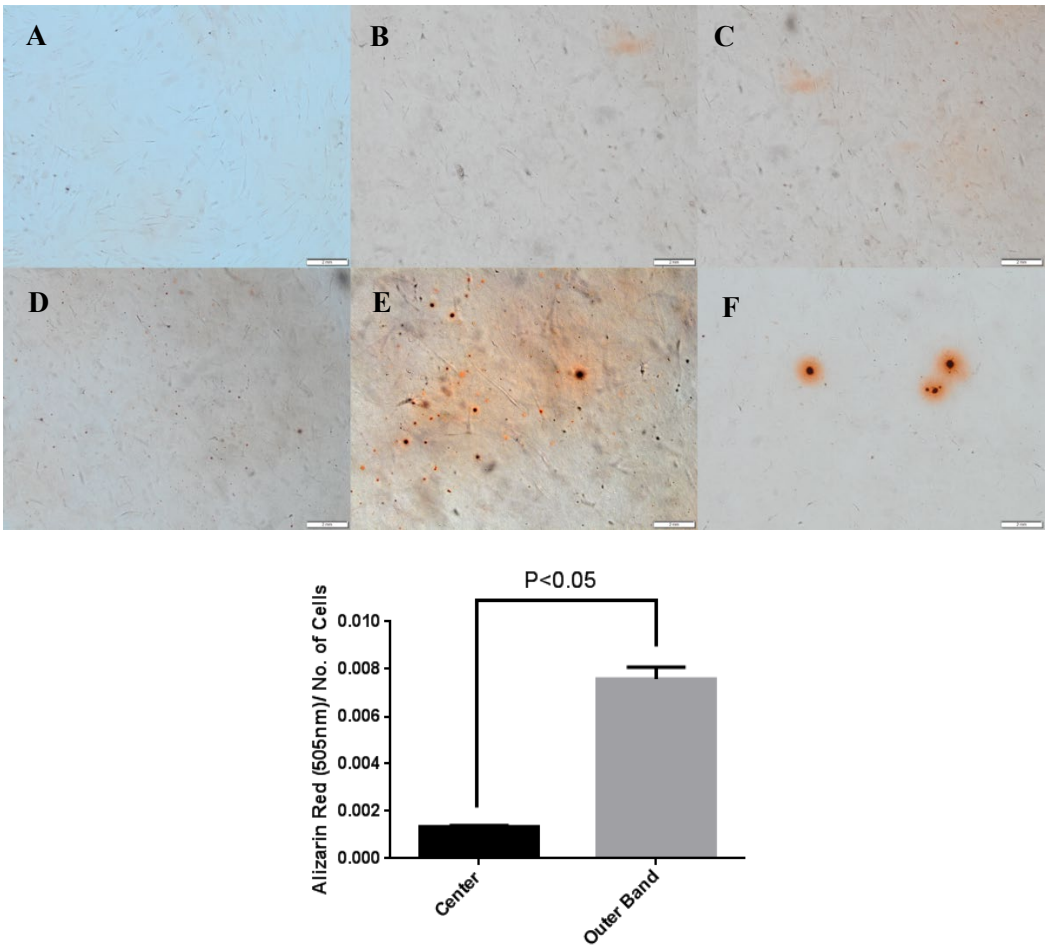

Figure 4. A-F. Panels showing serial imaging of ARS mineralization of hASCs in collagen sample, moving outward from the center region. Quantification of ARS (below) by measuring absorbance and normalizing to the number of cells between regions.

Adipogenesis

To investigate the effect of miR-21 in the 405nm activated center region, Oil Red O staining was conducted to observe the lipid formation quantities in the center vs. outer band region. For comparison, an hASCs-only sample was used to observed the effect of the cells' differentiation in stromal media over the course of time. Human adipose stem cells have been shown to be capable of differentiating into multiple different lineages, including adipocytes and osteoblasts [29]. The mechanism and stages of differentiation to adipocytes is not completely

understood, as the progenitor cells tend to enter a pre-adipose fibroblastic lineage first. In [30], however, it was demonstrated that miR-21 was over-expressed in adipocytes differentiated from hASCs. The results of the Oil Red O staining, shown in **Figure 5**, show higher lipid formation in the center hASCs against the osteogenic differentiated cells in the outer-band, as well as the hASCs control group. A likely explanation of this is the formation of pre-adipose fibroblastic cells in the control group, while a more accelerated differentiation effect is observed with miR-21 towards adipogenesis. The statistically lower formation of lipids in the outer band hASCs is expected as these cells commit to the osteogenic lineage.

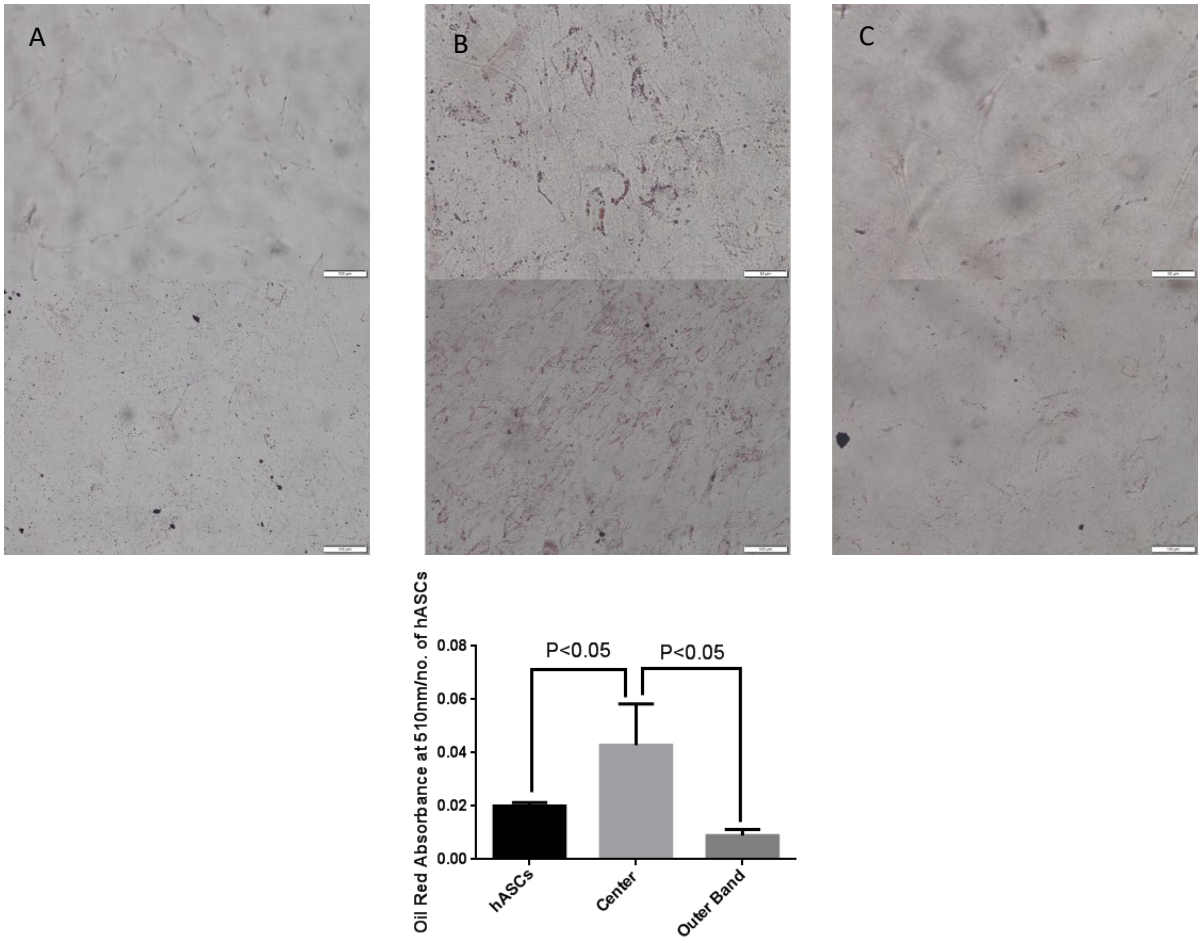

Figure 5. Oil Red O Staining. (Above) A. hASCs-only group, B. Center-region activated with 405nm to release miR-21, and C. Outer-band, osteogenically induced with miR-148b photorelease. (Below) Normalized absorbance quantification of Oil Red O staining, after de-staining.

Conclusion

Spatially-targeted differentiation of stem cells into different types can improve the graded functionality of the new tissue, and prevent mechanical degradation over time. We demonstrated the ability to differentiate hASCs into osteoblast and adipogenic lineages. The model presented enables the design of more complex interface tissues between muscles and ligament, ligament and bone, periodontal and alveolar bone, and tendon and bone. Translational implementation of this technology will need to be addressed in *in vivo* studies that underscore the mechanical and graded benefit of these nanoparticle-targeted regenerative therapies.

References

[1] E. Bayrak and P. Huri, "Engineering Musculoskeletal Tissue Interfaces," Front Mater, vol. 5, no. 24, 2018.

[2] L. Freed, A. Hollander, I. Martin, J. Barry, R. Langer and G. Vunjak-Novakovic, "Chondrogenesis in a cell-polymer-bioreactor system," Exp Cell Res, vol. 240, pp. 58-65, 1998.

[3] K. L. Moffat, A. S. Kwei, J. P. Spalazzi, S. B. Doty, W. N. Levine and H. H. Lu, "Novel nanofiber-based scaffold for rotator cuff repair and augmentation," Tissue Eng. Part A, vol. 15, pp. 115-26, 2009.

[4] L. Carlsson, T. Röstlund, B. Albrektsson, T. Albrektsson and P. I. Brånemar, "Osseointegration of titanium implants," Acta Orthop Scand, vol. 57, pp. 285-89, 1986.

[5] S. F. Tellado, E. R. Balmayor and M. V. Griensven, "Strategies to engineer tendon/ligament to bone interface: biomaterials, cells and growth factors," Adv Drug Deliv Rev, vol. 94, pp. 126-40, 2015.

[6] B. S. Kim, E. J. Kim, J. S. Choi, J. H. Jeong, C. H. Jo and Y. W. Cho, "Human collagen-based multilayer scaffolds for tendon-to-bone interface tissue engineering," J. Biomed. Mater. Res. Part A, vol. 102, pp. 4044-54, 2014.

[7] D. B. Robertson, D. M. Daniel and E. Biden, "Soft-tissue fixation to bone," Am J Sports Med, vol. 14, p. 398–403, 1986.

[8] S. A. Rodeo, S. P. Arnoczky, P. A. Torzilli, C. Hidaka and R. F. Warren, "Tendon-healing in a bone tunnel - a biomechanical and histological study in the dog," J Bone Joint Surg Am, vol. 75A, pp. 1795-1803, 1993.

[9] K. H, Z. Y and V. S, "Functionally graded multilayer scaffolds for in vivo osteochondral tissue engineering," Acta Biomater, vol. 15, pp. 365-77, 2018.

[10] A. Tampieri, M. Sandri, E. Landi, D. Pressato, S. Francioli and R. Quarto, "Design of graded biomimetic osteochondral composite scaffolds," Biomaterials, vol. 29, pp. 3539-46, 2008.

[11] R. Langer and J. Vacanti, "Tissue engineering," Science, vol. 260, pp. 920-26, 1993.

[12] I. Martin, R. Suetterlin and W. Baschong, "Enhanced cartilage tissue engineering by sequential exposure of chrondrocytes to FGF-2 during 2D expansion and BMP-2 during 3D cultivation," J Cell Biochem, vol. 83, pp. 121-128, 2001.

[13] Y. Ogata, Y. Mabuchi, K. Shinoda, Y. Horiike, M. Mizuno, K. Otabe and C. Akazawa, "Anterior cruciate ligament-derived mesenchymal stromal cells have a propensity to differentiate into the ligament lineage," Regen Ther, vol. 8, pp. 20-28, 2018.

[14] R. A. Somoza, J. F. Welter, D. Correa and A. I. Caplan, "Chondrogenic Differentiation of Mesenchymal Stem Cells: Challenges and Unfulfilled Expectations," Tissue Eng Part B Rev, vol. 20, no. 6, pp. 596-608, 2014.

[15] L. Pettersson, P. Kingham, M. Wiberg and P. Kelk, "In Vitro Osteogenic Differentiation of Human Mesenchymal Stem Cells from Jawbone Compared with Dental Tissue," Tissue Eng Reg Med, vol. 14, no. 6, pp. 763-74, 2017.

[16] B. Peng, Y. Chen and K. W. Leong, "MicroRNA Delivery for Regenerative Medicine," Adv Drug Deliv Rev, vol. 88, pp. 108-122, 2015.

[17] M. Abu-Laban, R. Kumal, J. Casey, J. Becca, D. LaMaster, C. Pacheco, D. Sykes, L. Jensen, L. Haber and D. Hayes, "Comparison of thermally actuated retro-diels-alder release groups for nanoparticle based nucleic acid delivery," J. Colloid Interface Sci., vol. 526, pp. 312-321, 2018.

[18] A. Qureshi, W. Monroe, V. Dasa, J. Gimble and D. Hayes, "miR-148b-nanoparticle conjugates for light mediated osteogenesis of human adipose stromal/stem cells," Biomaterials, vol. 34, no. 31, pp. 7799-810, 2013.

[19] X. Li, D. Xiao and Z. Zhang, "Landau Damping of Quantum Plasmons in Metal Nanostructures," New J Phys, vol. 15, no. 2, p. 023011, 2013.

[20] A. Qureshi, A. Doyle, C. Chen, D. Coulon, V. Dasa, F. Pi, B. Levi, W. Monroe, J. Gimble and D. Hayes, "Photoactivated miR-148b–nanoparticle conjugates improve closure of critical size mouse calvarial defects," Acta Biomater, vol. 12, pp. 166-73, 2015.

[21] D. Sekar, S. Saravanan, K. Karikalan, K. Thirugnanasambantham, P. Lalitha and V. Islam, "Role of microRNA 21 in mesenchymal stem cell (MSC) differentiation: a powerful biomarker in MSCs derived cells," Curr Pharm Biotechnol, vol. 16, no. 1, pp. 43-8, 2015.

[22] C. Gregory, W. Gunn, P. A and P. DJ, "An Alizarin red-based assay of mineralization by adherent cells in culture: comparison with cetylpyridinium chloride extraction," Anal Biochem, vol. 329, no. 1, pp. 77-84, 2004.

[23] S. Li, J. Poche, Y. Liu, T. Scherr, J. McCann, A. Forghani, M. Smoak, M. Muir, L. Berntsen, C. Chen, D. Ravnic, J. Gimble and D. Hayes, "Hybrid Synthetic-Biological Hydrogel System for Adipose Tissue Regeneration," Macromol Biosci, vol. 18, no. 12, p. 1800122, 2018.

[24] K. Livak and T. Shmittgen, "Analysis of relative gene expression data using real-time quantitative PCR and the 2(-Delta Delta C(T)) Method," Methods, vol. 25, no. 4, pp. 402-8, 2001.

[25] J. Xu, Z. Li, Y. Hou and W. Fang, "Potential mechanisms underlying the Runx2 induced osteogenesis of bone marrow mesenchymal stem cells," Am J Transl Res, vol. 7, no. 12, pp. 2527-35, 2015.

[26] M. Yavropoulou and J. Yovos, "The role of the wnt signaling pathway in osteoblast commitment and differentiation," Hormones, vol. 6, no. 4, pp. 279-94, 2007.

[27] J. Wei and G. Karsenty, "An overview of the metabolic functions of osteocalcin," Rev Endocr Metab Disord, vol. 16, no. 2, pp. 93-8, 2015.

[28] H. Blair, Q. Larrouture, Y. Li, H. Lin, D. Beer-Stoltz, L. Liu, R. Tuan, L. Robinson, P. Schlesinger and D. Nelson, "Osteoblast Differentiation and Bone Matrix Formation In Vivo and In Vitro," TISSUE ENGINEERING: Part B, vol. 23, no. 3, pp. 268-79, 2017.

[29] S. Yarak and O. OK, "Human adipose-derived stem cells: current challenges and clinical perspectives.," An Bras Dermatol, vol. 85, no. 5, pp. 647-56, 2010.

[30] Y. Kim, S. Hwang, Y. Bae and J. Jung, "MiR-21 regulates adipogenic differentiation through the modulation of TGF-beta signaling in mesenchymal stem cells derived from human adipose tissue," Stem Cells, vol. 27, no. 12, pp. 3093-102, 2009.

CHAPTER 5.

Summary and Conclusion

The efforts presented in this document demonstrate the spatiotemporal control capability of light activated nanoparticles conjugated with small nucleic acids. The ability to trigger release was effectively designed using the thermally responsive properties of the Diels-Alder linkage chemistry. Using this technology, we have demonstrated not only the ability to trigger nanoparticle delivery of miRNA to differentiate hMSCs but also the ability to co-deliver two miRNAs to amplify the effect of osteogenesis by the symbiotic action of miR-21 and miR-148b. Additionally, the ability to differentiate stem cells into multiple lineages along specific spatial dimensions by photoactivation at discrete wavelengths of light was also demonstrated. This technique presents a paradigm shift in the reconstruction technologies of adjacent soft and hard tissue for improved graded interfacial design.

Systems providing spatiotemporal control have the potential to improve outcomes in surgical reconstruction and regenerative medicine by precise modulation of tissue repair processes. Regulation of gene expression with miRNA mimics is a promising tool for enhancing control of tissue repair processes particularly when combined with endogenous mesenchymal stem cell (MSC) progenitors. Spatiotemporally directing the proliferation and osteogenic differentiation of these progenitors is of particular interest in the design of therapies for segmental bone defects, spinal fusion and craniofacial reconstruction. The capability to target endogenous MSCs and modulate pluripotency and osteogenic differentiation provides a clinically relevant tool to stimulate osteogenic progenitors and improve segmental defect repair.

While the nanoparticle vehicle systems may diffuse *in vivo*, they remain inert until photo-activated at resonant wavelengths, which can be spatially constrained. Furthermore, since the

released miRNA mimics are short lived and only transiently modulate mRNA expression, the risk of permanent activity once an activated cell has begun differentiation is unlikely. The miRNA mimics associated with the inactivated particles are expected to degrade slowly intracellularly through enzymatic action or hydrolysis, and cleared by the MPS/RES pathways *in vivo*.

The development of this technology represents a paradigm shift compared to current autograft or allograft reconstruction methods, which often fail as a result of poor graft vascularization, negative immune response and morbidity to the patient. Additionally, this technology addresses a critical limitation of current nucleic acid delivery methods that do not control spatiotemporal expression, resulting in inefficient transport as wells as severe off-target activity and side effects.

APPENDIX A.

Chapter 2 Supporting Information

DFT Computation:

Table S1. Input example used for furan computation at 298.15 K using B3LYP, 6-311G*

All at 298.15K for temp	Furan	Acid Reagent	Product	TS	1 hartree =	
DFT Energy (a.u.)	-667.611746072643	-359.523311860088	-1027.142132893980	-1027.102185	627.5095	kcal/mol
ZPE Correction (a.u)	0.097143	0.068199	0.171185	0.16739		
Thermal correction to Energy (a.u)	0.104053	0.073616	0.182777	0.179716	Temperature	
Thermal correction to Enthalpy (a.u)	0.104996	0.074559	0.183721	0.18066	298.15	K
Total Entropy (cal/mol * K)	84.154	74.941	106.889	111.338		
Cv (cal/mol K)	24.370	19.827	45.365	46.608		
DFT Energy (kcal/mol)	-418932.713	-225604.2937	-644541.4462	-644516.3783		
ZPE Correction (kcal/mol)	60.95815536	42.79552039	107.4202138	105.0388152		
Thermal correction to Energy (kcal/mol)	65.294246	46.19473935	114.6943039	112.7734973		
Thermal correction to Enthalpy (kcal/mol)	65.88598746	46.78648081	115.2866728	113.3658663		
Total Entropy (kcal/mol *K)	0.084	0.075	0.107	0.111		
Corrected Energy(kcal/mol)	-418867.4187	-225558.0989	-644426.7519	-644403.6048		
Corrected Enthalpy(kcal/mol	-418866.827	-225557.5072	-644426.159568385	-644403.0124		
Corrected Gibbs Free Energy	-418891.9175	-225579.8508	-644458.0285	-644436.2078		
Delta H forward (kcal/mol)	21.32176281					
Delta H reverse (kcal/mol)	23.14716363					
Delta G forward (kcal/mol)	35.56051236					
Delta G reverse (kcal/mol)	21.82069428					

SNP & DA Synthesis:

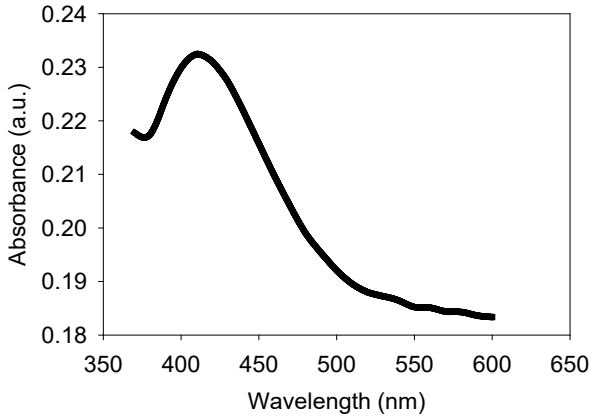

Figure S1. UV-Vis spectra of SNP, with maxima at 415 nm.

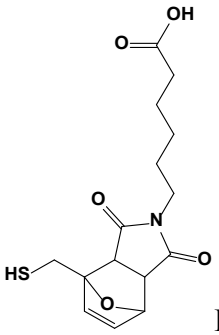

Furan DA linker

Purified with HPLC C18 Column; 100 % H_2O flow at 0.3 mL/min

Yield: 21.6 %

^{1}H NMR (500 MHz, DMSO-d6) δ 1.24 (m, 2H), 1.46 (p, J = 7.5 Hz, 4H), 2.18 (t, J = 6.7 Hz, 2H), 2.92 (d, J = 6.4 Hz, 1H), 3.17 (m, 1H), 3.58 (m, 2H), 4.06 (m, 2H), 5.25 (t, J = 7.1 Hz, 1H), 6.37 (m, 1H), 6.51 (m, 1H).

^{13}C NMR (500 MHz, DMSO-d6): δ 25.67, 27.38, 28.36, 33.26, 34.83, 39.62, 50.81, 51.11, 80.77, 92.88, 135.46, 139.69, 176.94, 177.24, 177.49

MS (ESI+): m/z calculated for $C_{15}H_{21}NO_5S$, 325.40; found ($M+H^+$) 326.1061.

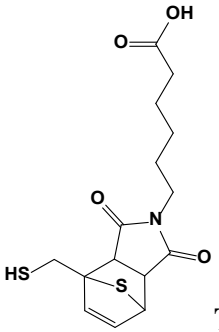

Thiophene DA linker

Purified with HPLC C18 Column; 1.3 % ACN 98.7 % H_20 flow at 0.3 ml/min

Yield: 24.8 %

^{1}H NMR (500 MHz, DMSO-d6) δ 1.20 (m, 2H), 1.46 (m, 4H), 2.17 (t, J = 7.8 Hz, 2H), 2.64 (dd, J = 19.9, 4.3 Hz, 1H), 3.10 (dd, J = 20.1, 9.5 Hz, 1H), 3.31 (m, 2H), 3.42 (dd, J = 12.6, 7.36 Hz, 2H), 3.87 (dd, J = 9.5, 4.4 Hz, 1H), 6.74 (m, 1H), 6.91 (m, 1H).

^{13}C NMR (500 MHz, DMSO-d6): δ 24.49, 26.15, 27.21, 33.50, 35.69, 39.42, 47.71, 51.21, 51.68, 52.58, 134.89, 140.64, 175.54, 175.55, 177.02

MS (ESI+): m/z calculated for $C_{15}H_{21}NO_4S_2$, 341.44; found ($M+H^+$) 342.08.

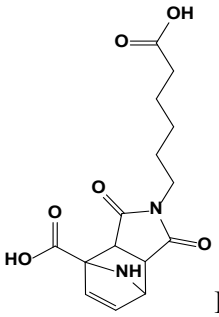

Pyrrole DA linker

Purified with HPLC C18 Column; 20 % ACN and 80 % H_20 flow at 0.3 ml/min.

Yield: 23.8 %

^{1}H NMR (500 MHz, DMSO-d6) δ 1.22 (m, 2H), 1.55 (m, 4H), 2.18 (t, J = 7.4 Hz, 2H), 3.01 (m, 1H), 3.59 (m, 2H), 5.90 (dt, J = 17.7, 5.8 Hz, 1H), 6.13 (q, J = 2.7 Hz, 1H), 6.68 (m, 1H), 7.01 (m, 1H).

^{13}C NMR NMR (500 MHz, DMSO-d6) δ 24.45, 26.10, 27.20, 33.92, 38.43, 44.11, 51.67, 55.82, 56.11, 123.83, 134.93, 162.35, 171.57, 176.14, 177.25.

MS (ESI-): m/z calculated for $C_{15}H_{18}N_2O$, 322.23; found ($M+H^+$): 323.16.

Photothermal Release:

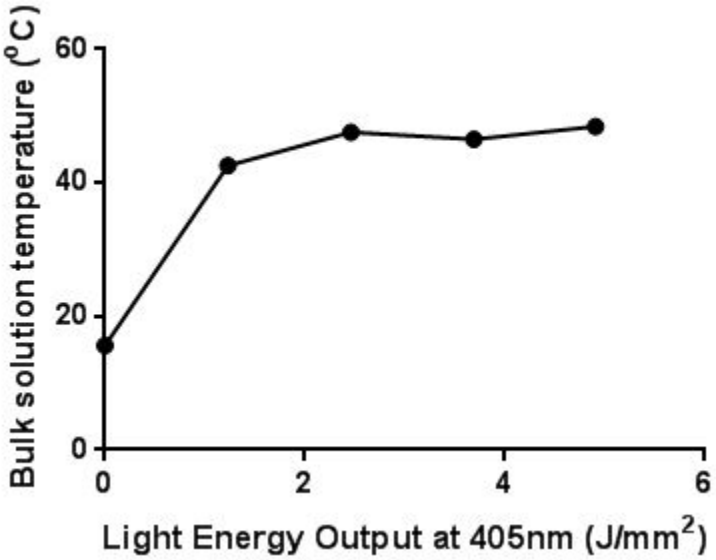

Figure S2. Bulk temperature of SNP solution during irradiation with 405 nm mounted LED, +/-SEM.

APPENDIX B.

Chapter 3 Supplementary Information

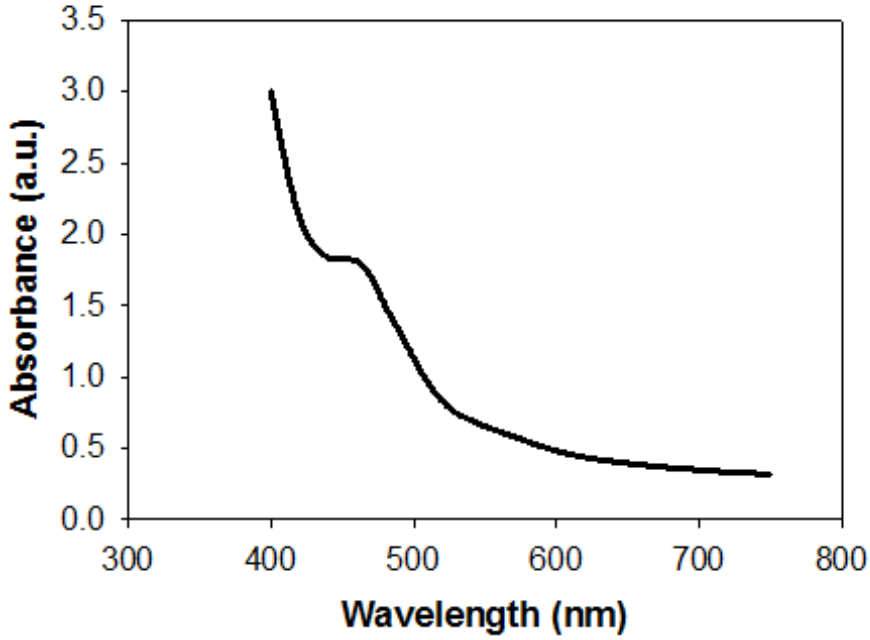

Figure S1. Absorbance spectra of Diels-Alder linker

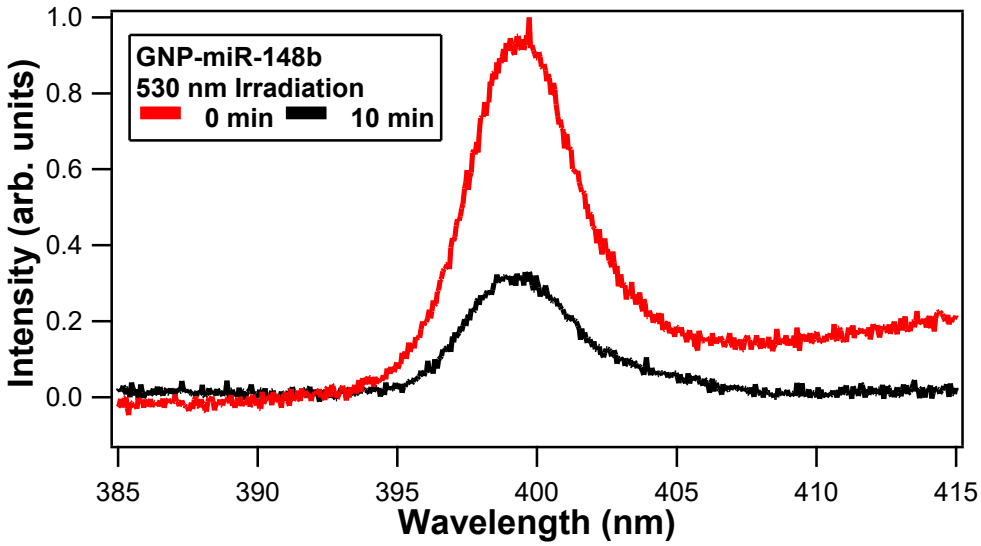

Figure S2. Representative SHG spectra of miRNA-functionalized gold nanoparticles at different wavelengths and irradiation times.

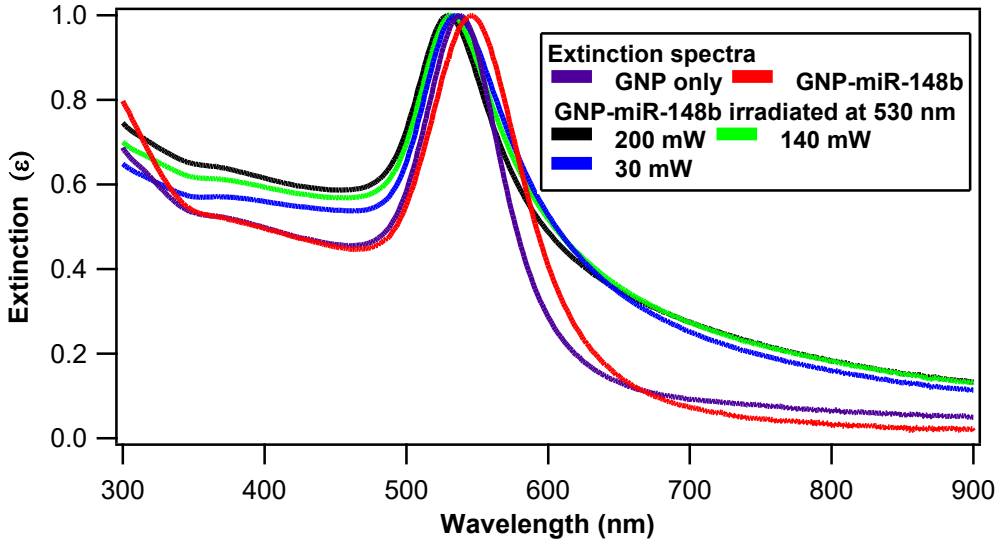

Figure S3. Extinction spectra of the GNPS, the miRNA-functionalized GNPs, and the miRNA-functionalized GNPs after laser irradiation with 530 nm wavelength.

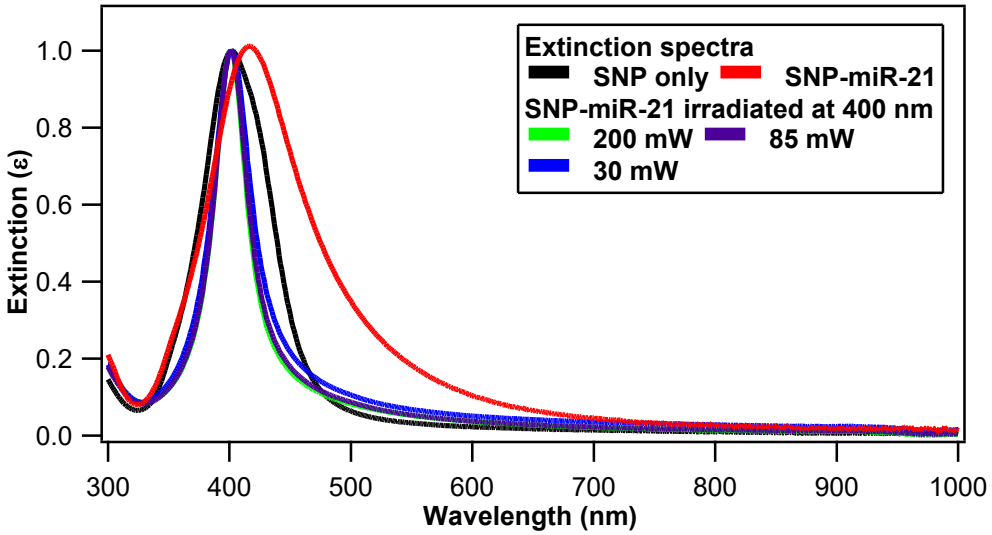

Figure S4. Extinction spectra of the SNPs, the miRNA-functionalized SNPs, and the miRNA-functionalized SNPs after laser irradiation with 400 nm wavelength.

Table S1: Fit parameters obtained for the SNP-miR-21nanoparticle system at different 400 nm laser powers

Power (mW)	Fit Parameters (SNP-miR-21)		
	A	B	k (10^{-2} S^{-1})
35	0.652 ± 0.001	0.353 ± 0.005	0.85 ± 0.02
85	0.603 ± 0.001	0.405 ± 0.005	1.23 ± 0.03
140	0.553 ± 0.001	0.432 ± 0.007	1.80 ± 0.05
200	0.504 ± 0.001	0.472 ± 0.012	2.67 ± 0.13

Table S2: Fit parameters obtained for the GNP-miR-148b nanoparticle system at different 530 nm laser powers

Power (mW)	Fit Parameters (GNP-miR-148b)		
	A	B	k (10^{-2} S^{-1})
35	0.803 ± 0.001	0.188 ± 0.005	0.82 ± 0.04
85	0.754 ± 0.001	0.242 ± 0.006	1.03 ± 0.04
140	0.699 ± 0.001	0.298 ± 0.005	1.34 ± 0.04
200	0.635 ± 0.001	0.356 ± 0.008	2.04 ± 0.09

SNP-FAM overlay images (none-530 nm-405 nm) 0.934, 0.938, 0.695

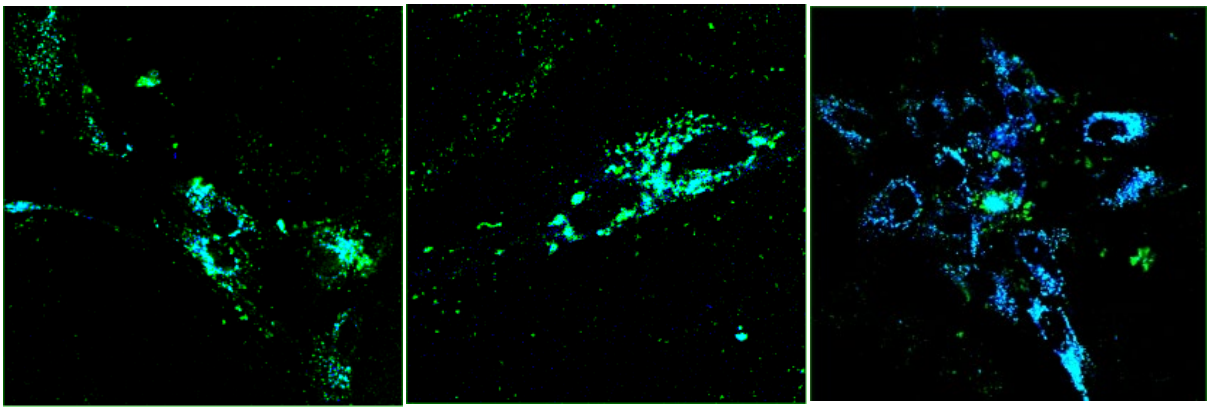

Transferrin-FAM overlay images (none-530 nm-405 nm) 0.45, 0.39, 0.53

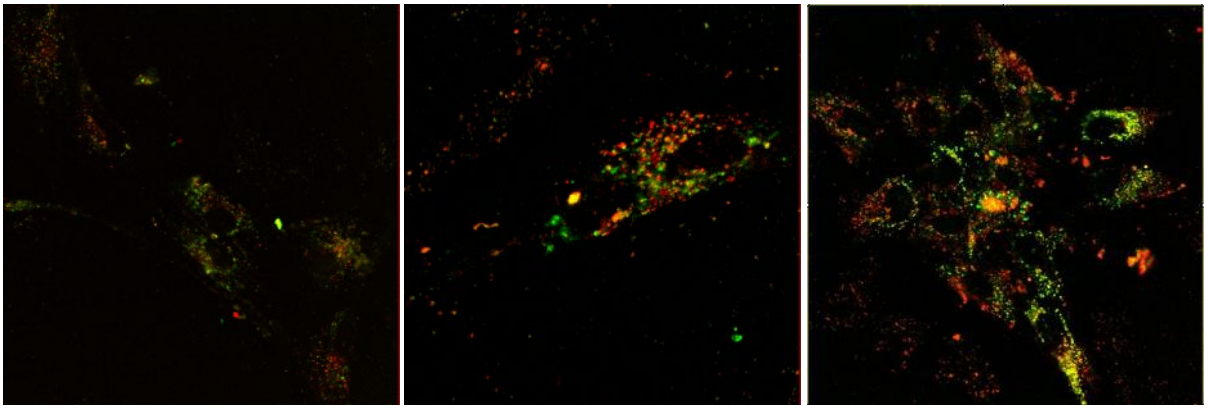

GNP-FAM overlay images (none-405 nm-530 nm) 0.935, 0.834, 0.660

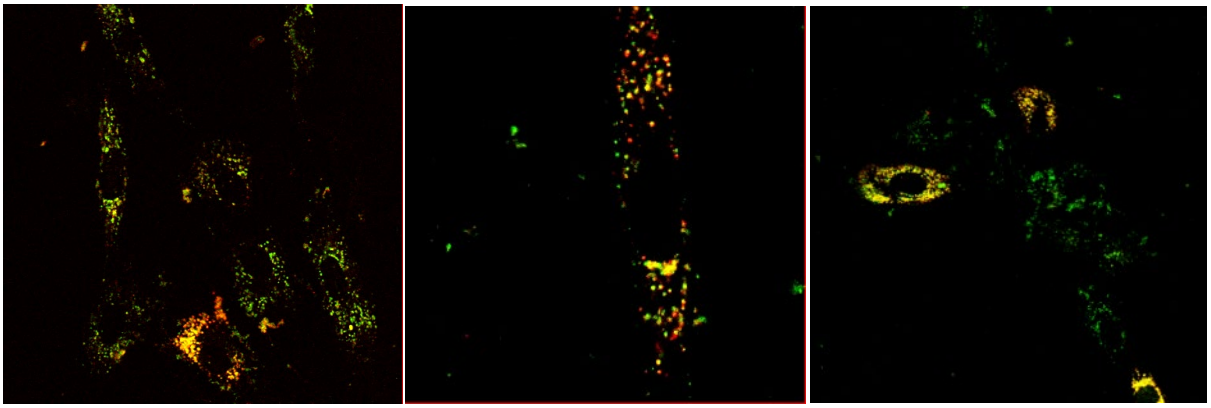

Z Stack images of none irradiated (top) and 405 nm irradiated (bottom) SNP-FAM-transferrin samples

None

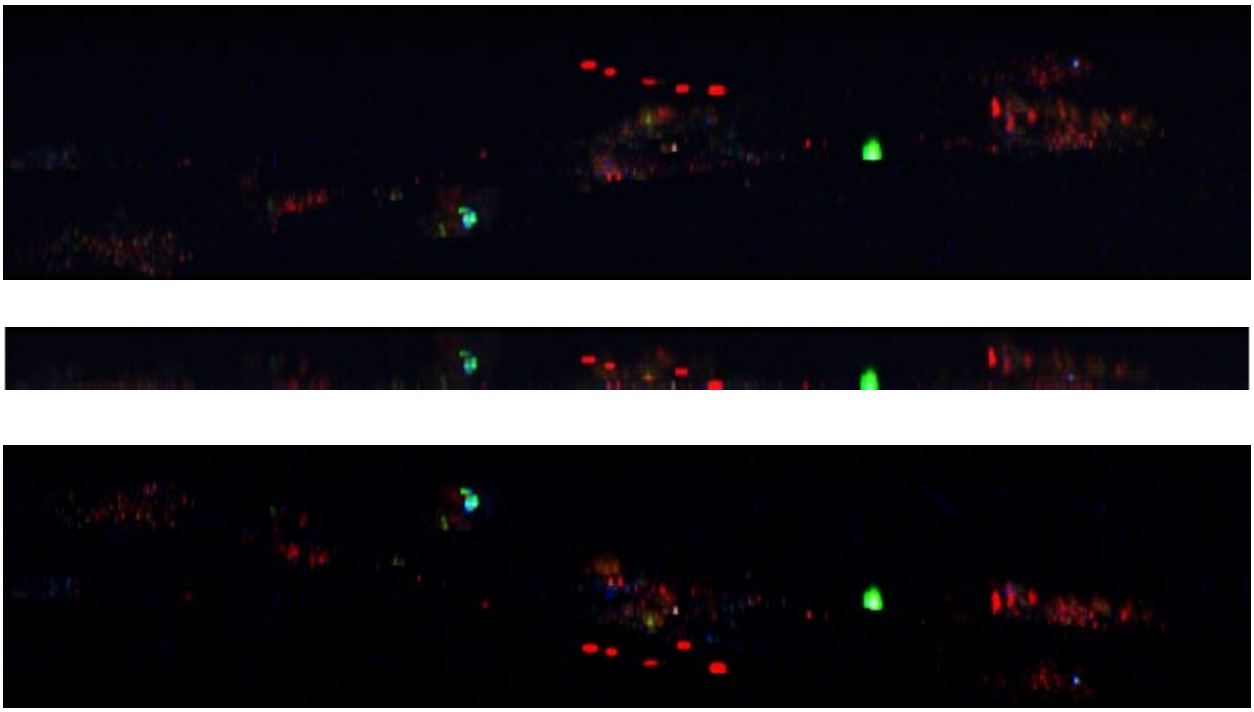

405nm

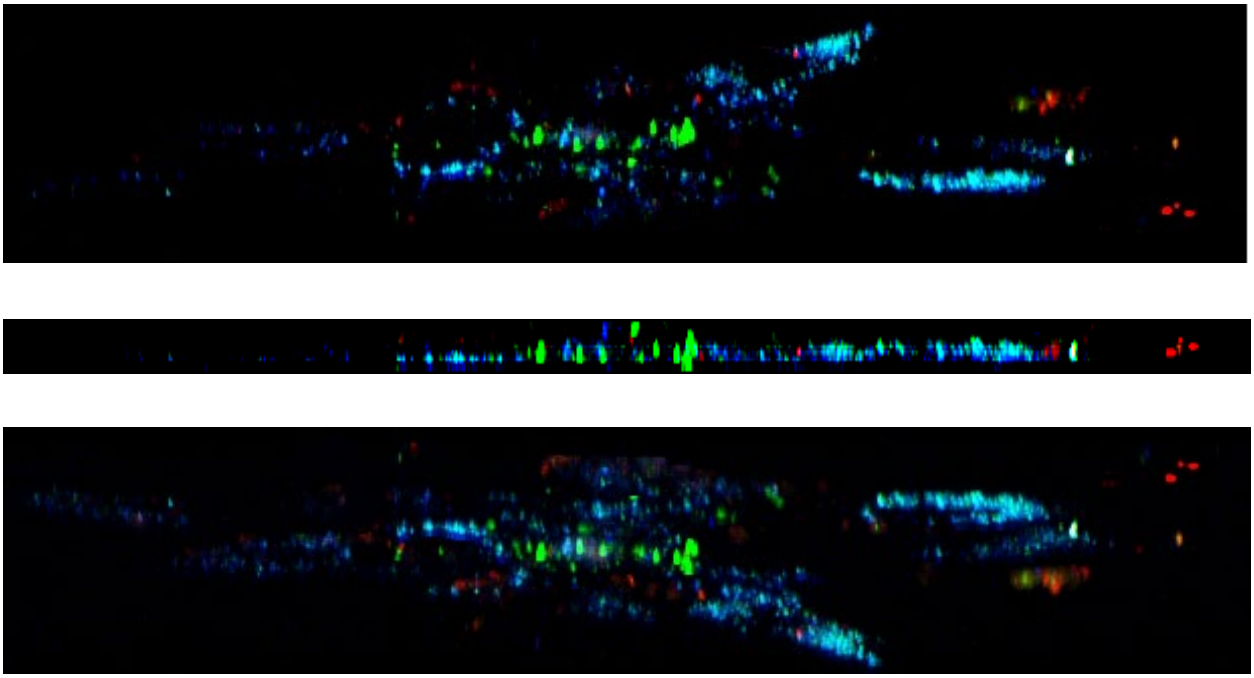

Figure S5. Colocalization, z-stack images of SNP/GNP with FAM-miRNA molecules

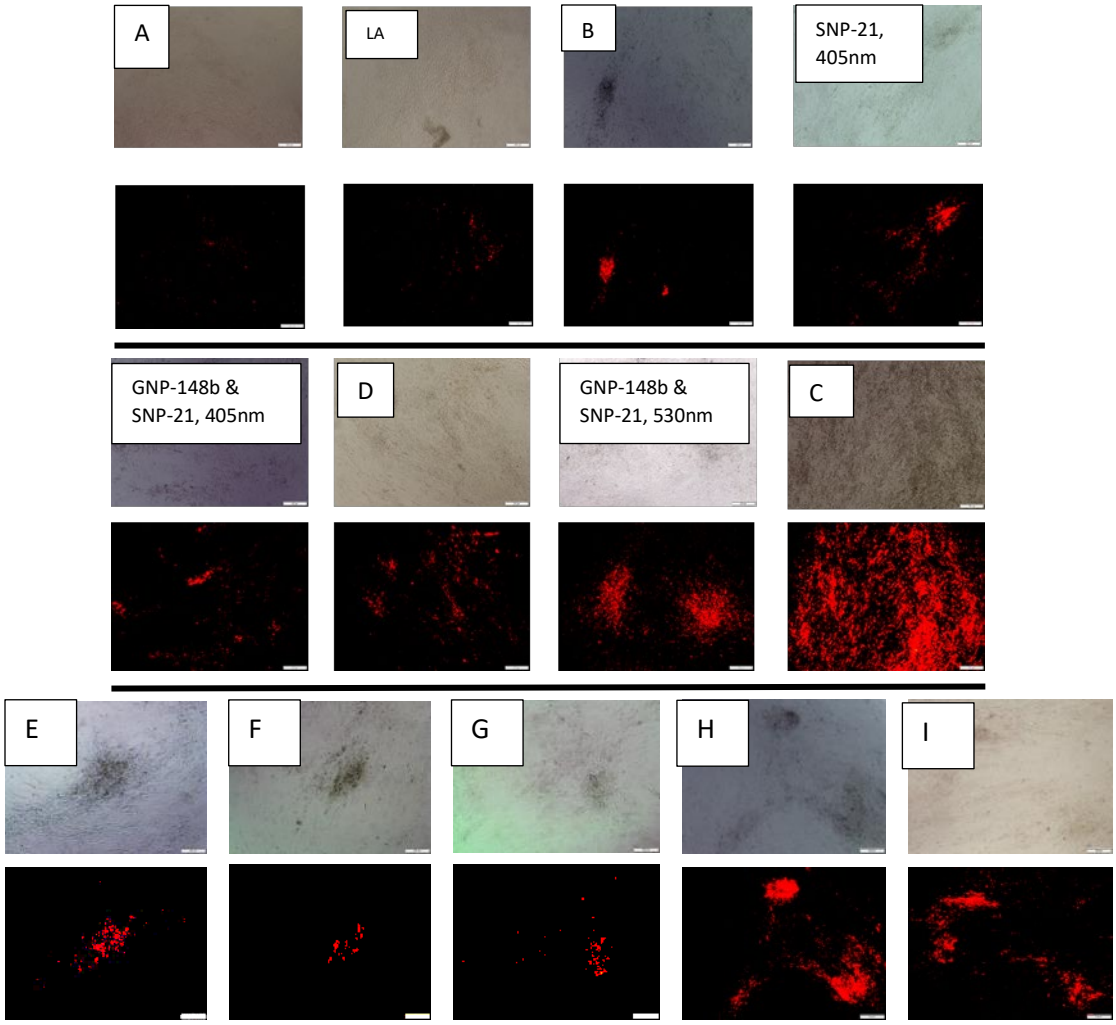

Figure S6. Xylene Orange images for all NP groups tested

Table S3. ARS images for all NP groups tested

Stromal Medium (A)		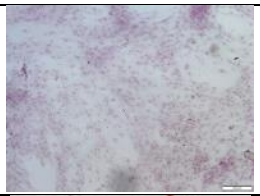	
Osteogenic Medium (C)	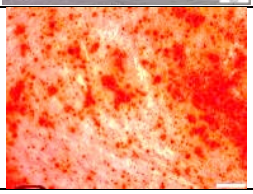	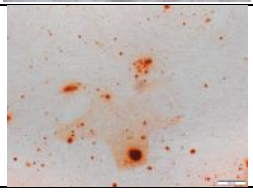	

GNPs & SNPs non-modified, irradiated at 405 nm & 530 nm (LA)	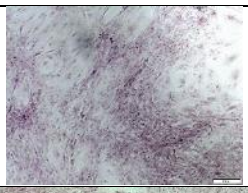		
GNP-miR-148b & SNP-miR-21, non-irradiated (B)	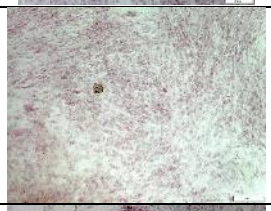		
SNP-miR-21, 405 nm			
GNP-miR-148b, 530 nm (D)	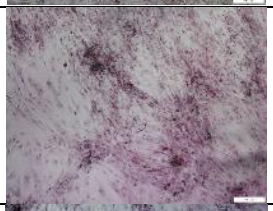		
SNP-miR-21 GNP-miR-148b, 405 nm	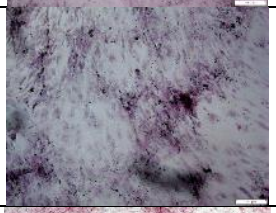	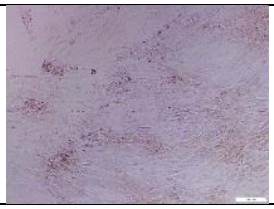	
SNP-miR-21 GNP-miR-148b, 530 nm	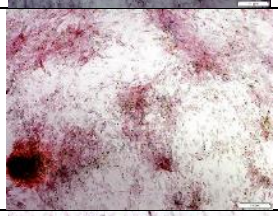		
SNP-miR-21 GNP-miR-148b, 405 nm & 530 nm 0 h (E)	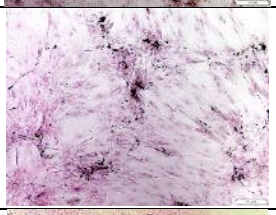	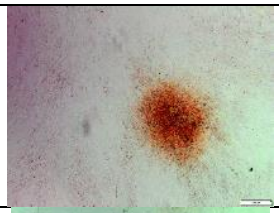	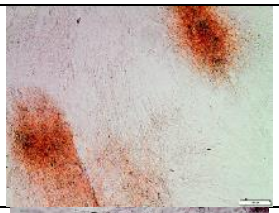
SNP-miR-21 GNP-miR-148b, 405 nm at 0 h & 530 nm at 24 h (F)	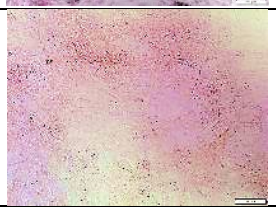	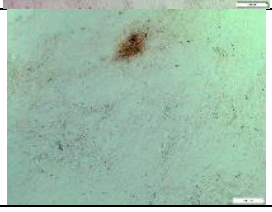	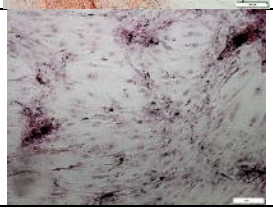

SNP-miR-21 GNP-miR-148b, 405 nm at 0 h & 530 nm at 48 h (G)	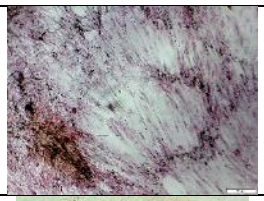		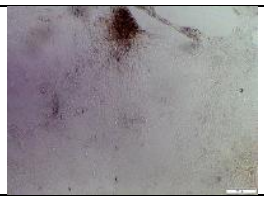
SNP-miR-21 GNP-miR-148b, 530 nm at 0 h & 405 nm at 24 h (H)		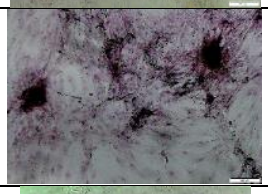	
SNP-miR-21 GNP-miR-148b, 530 nm at 0 h & 405 nm at 24 h (I)	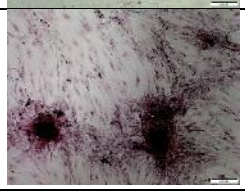		

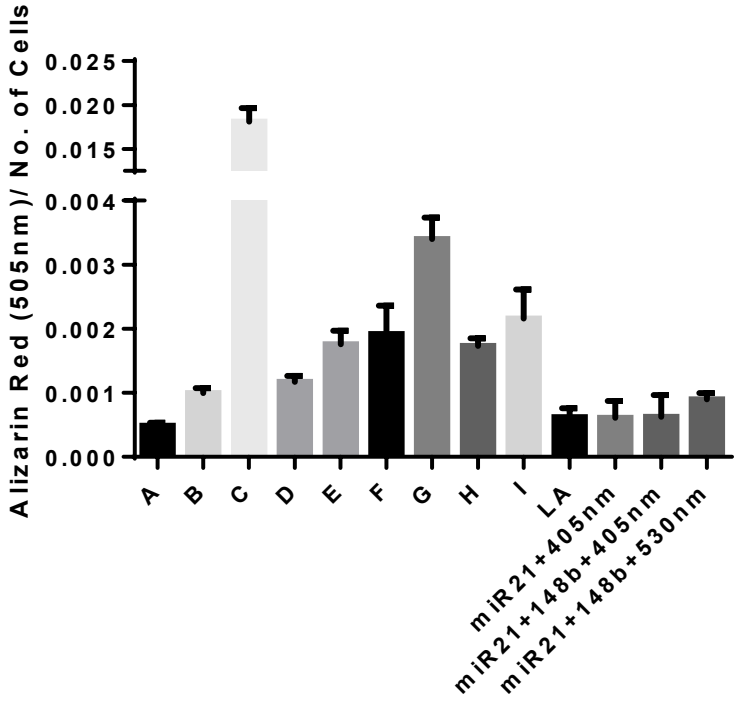

Figure S7. ARS quantification for all NP groups normalized to cell count

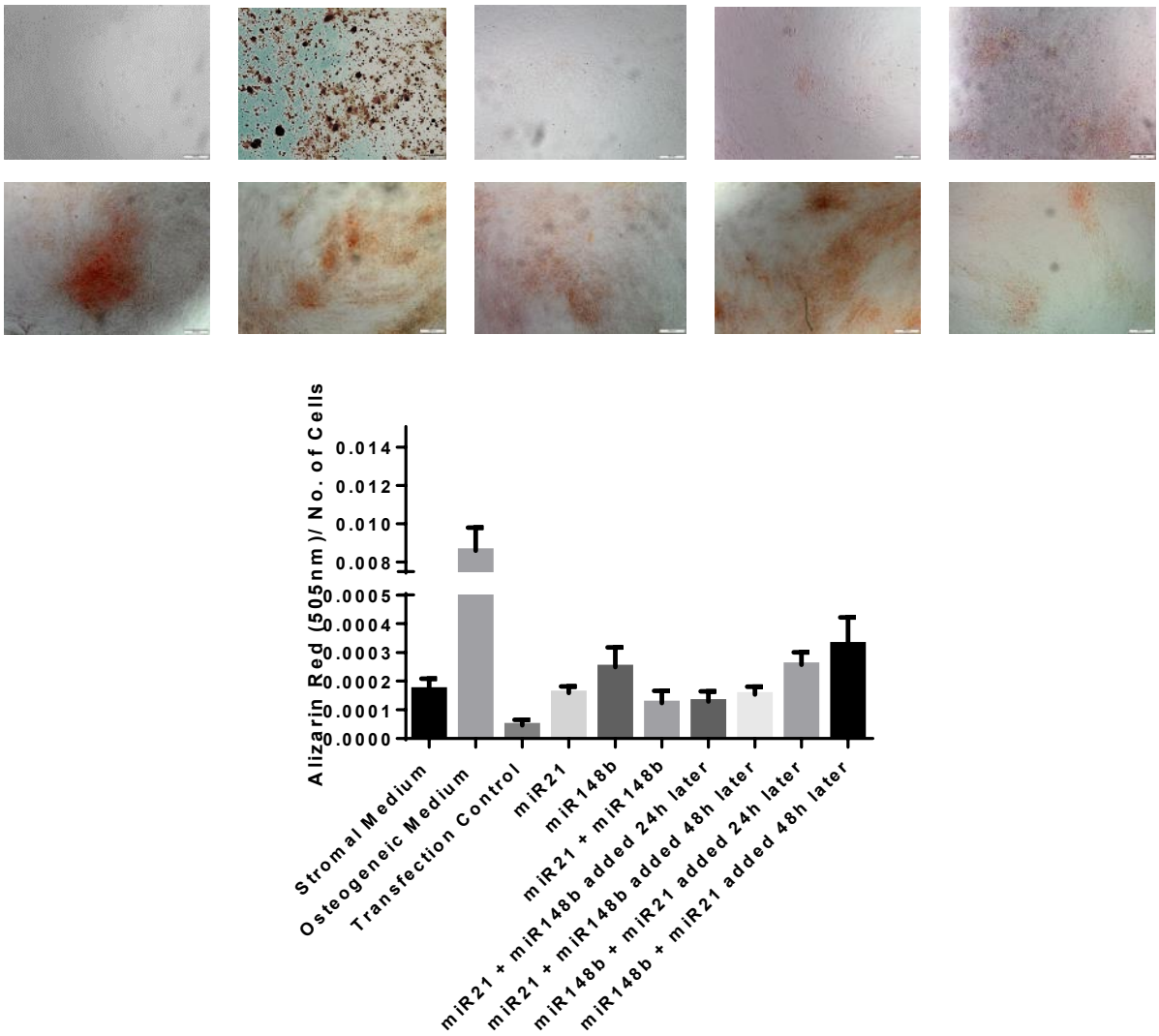

Figure S8. Chemical transfection groups ARS (images presented in same order, left to right, as listed on x-axis of graph)

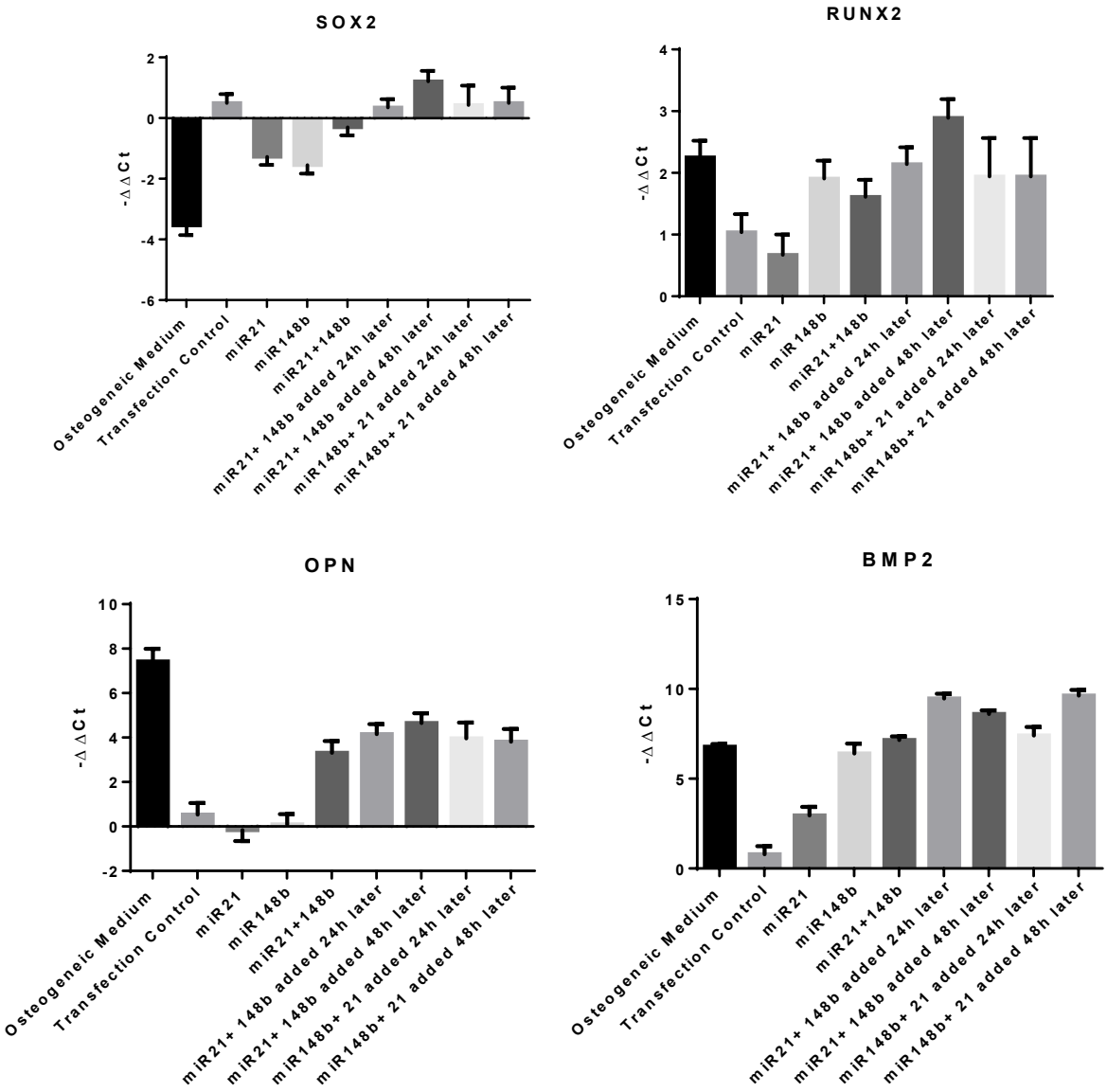

Figure S9. Chemical transfection groups PCR day 21

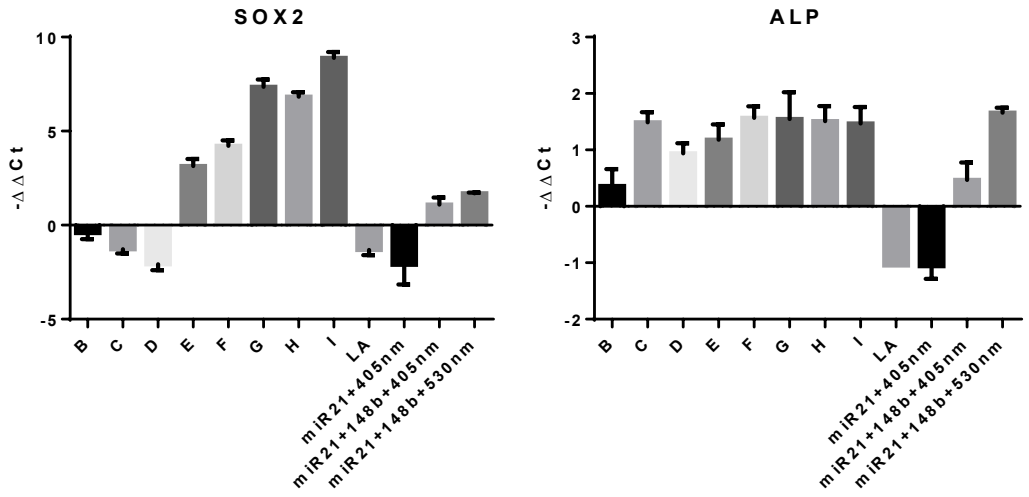

Figure S10. All NP groups PCR day 7

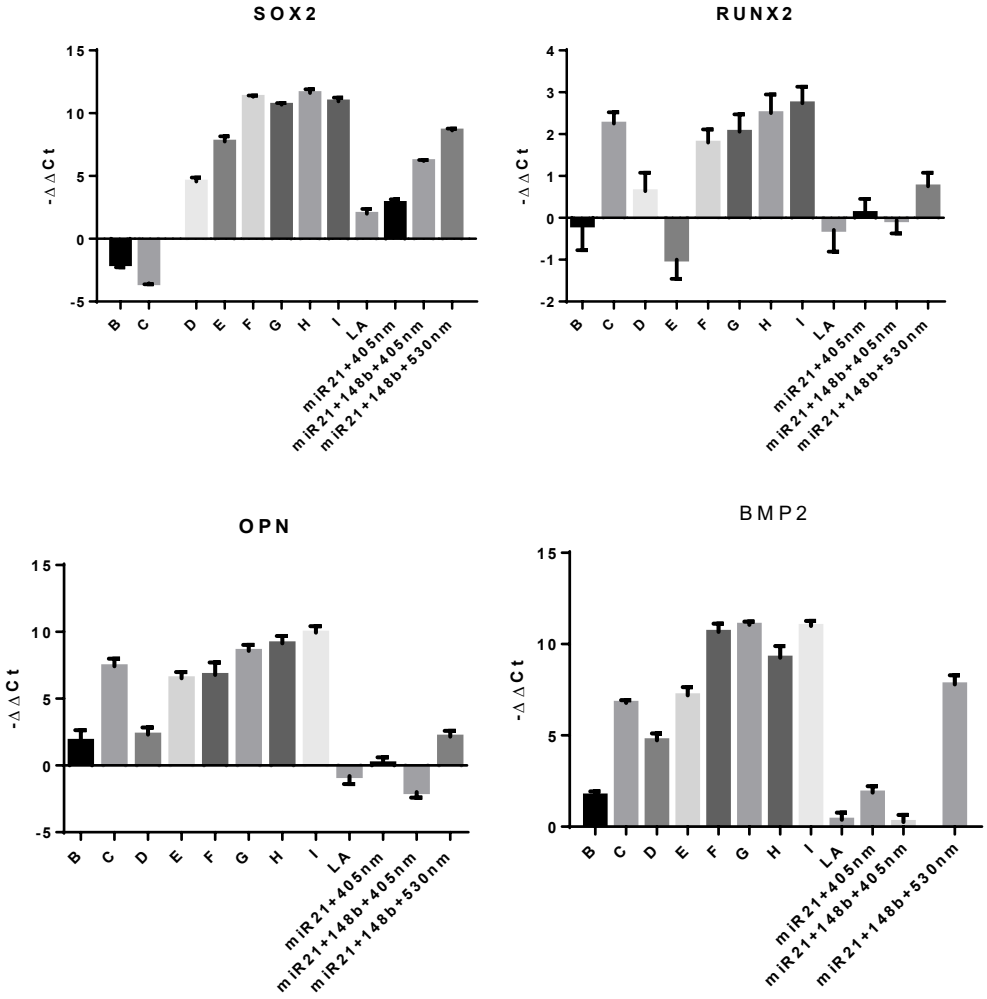

Figure S11. All NP groups PCR day 21

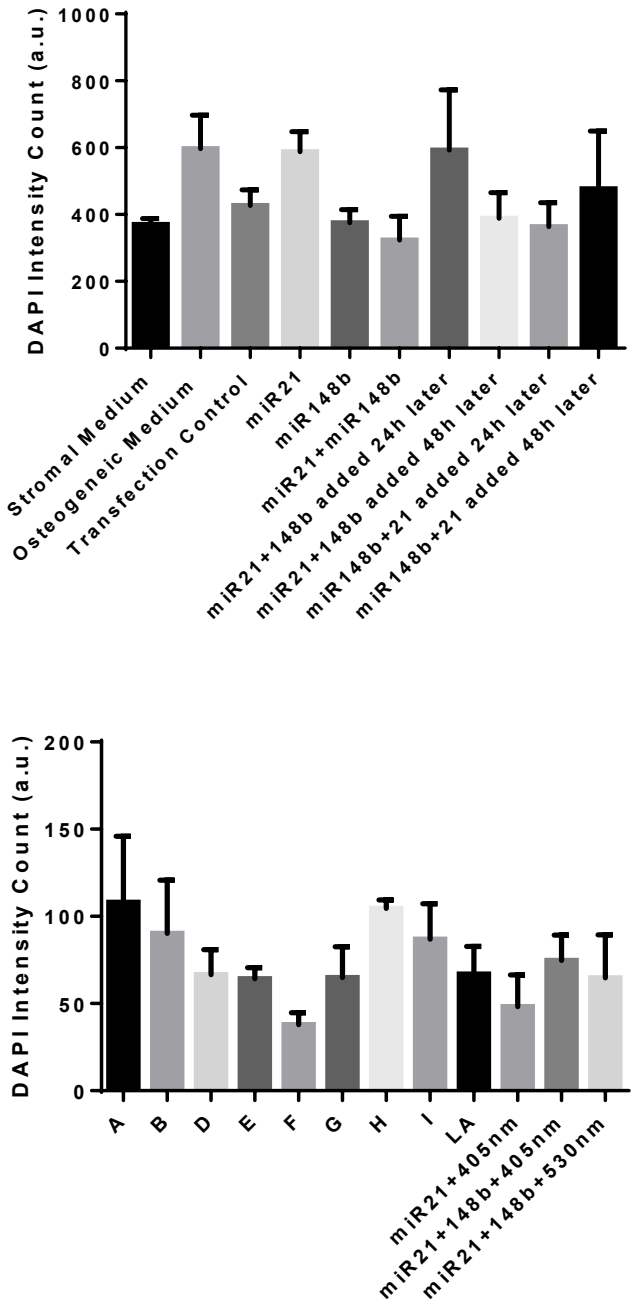

Figure S12. DAPI/Cell count at Day 21 for chemical transfection (top) and NP groups (bottom)

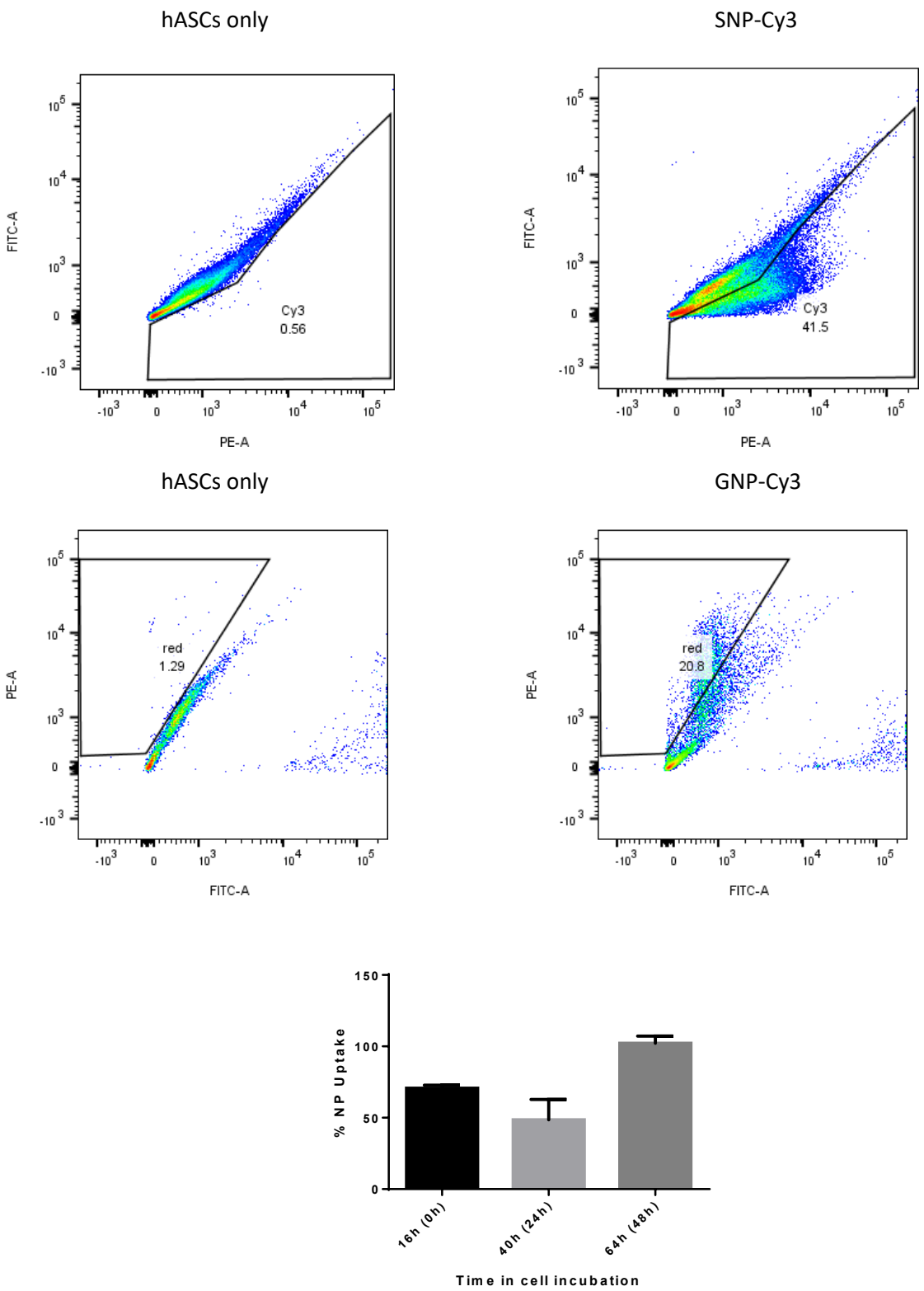

Figure S13. Transfection efficiencies of SNPs and GNPs in hASCs, measured using Flow Cytometry of Cy3 conjugated miRNA mimics, and uptake efficiency of SNPs using ICP-AES.

VITA

Mohammad Abu-Laban is a native of Amman, Jordan and was born in Abu Dhabi, UAE in October 1990. After earning his International Baccalaureate Diploma at the Modern Montessori School, Amman Jordan, he traveled to the US where he received his Bachelors of Science degree in Chemical Engineering at Louisiana State University (LSU), Baton Rouge, Louisiana. He then received his Masters of Science in Biological & Agricultural Engineering at LSU in May 2016 before moving to the Pennsylvania State University, University Park, to pursue his doctorate in Bioengineering, expected to be completed in the Summer of 2019.